

# Interstellar detection and chemical modeling of *iso*-propanol and its *normal* isomer

A. Belloche<sup>1</sup>, R. T. Garrod<sup>2</sup>, O. Zingsheim<sup>3</sup>, H. S. P. Müller<sup>3</sup>, and K. M. Menten<sup>1</sup>

<sup>1</sup> Max-Planck-Institut für Radioastronomie, Auf dem Hügel 69, 53121 Bonn, Germany  
 e-mail: belloche@mpi-fr-bonn.mpg.de

<sup>2</sup> Departments of Chemistry and Astronomy, University of Virginia, Charlottesville, VA 22904, USA

<sup>3</sup> I. Physikalisches Institut, Universität zu Köln, Zùlpicher Str. 77, 50937 Köln, Germany

Received March 17, 2022; accepted April 20, 2022

## ABSTRACT

**Context.** The detection of a branched alkyl molecule in the high-mass star forming protocluster Sgr B2(N) permitted by the advent of the Atacama Large Millimeter/submillimeter Array (ALMA) revealed a new dimension of interstellar chemistry. Astrochemical simulations subsequently predicted that beyond a certain degree of molecular complexity, branched molecules could even dominate over their straight-chain isomers.

**Aims.** More generally, we aim at probing further the presence in the interstellar medium of complex organic molecules with the capacity to exhibit both a *normal* and *iso* form, via the attachment of a functional group to either a primary or secondary carbon atom.

**Methods.** We used the imaging spectral line survey ReMoCA performed with ALMA at high angular resolution and the results of a recent spectroscopic study of propanol to search for the *iso* and *normal* isomers of this molecule in the hot molecular core Sgr B2(N2). We analyzed the interferometric spectra under the assumption of local thermodynamical equilibrium. We expanded the network of the astrochemical model MAGICKAL to explore the formation routes of propanol and put the observational results in a broader astrochemical context.

**Results.** We report the first interstellar detection of *iso*-propanol, *i*-C<sub>3</sub>H<sub>7</sub>OH, toward a position of Sgr B2(N2) that shows narrow linewidths. We also report the first secure detection of the *normal* isomer of propanol, *n*-C<sub>3</sub>H<sub>7</sub>OH, in a hot core. *iso*-Propanol is found to be nearly as abundant as *normal*-propanol, with an abundance ratio of 0.6 similar to the ratio of 0.4 that we obtained previously for *iso*- and *normal*-propyl cyanide in Sgr B2(N2) at lower angular resolution with our previous ALMA survey, EMOCA. The observational results are in good agreement with the outcomes of our astrochemical models, which indicate that OH-radical addition to propylene in dust-grain ice mantles, driven by water photodissociation, can produce appropriate quantities of *normal*- and *iso*-propanol. The *normal*-to-*iso* ratio in Sgr B2(N2) may be a direct inheritance of the branching ratio of this reaction process.

**Conclusions.** The detection of *normal*- and *iso*-propanol and their ratio indicate that the modest preference toward the *normal* form of propyl cyanide determined previously may be a more general feature among similarly sized interstellar molecules. Detecting other pairs of interstellar organic molecules with a functional group attached either to a primary or secondary carbon may help in pinning down the processes that dominate in setting their *normal*-to-*iso* ratios. Butanol and its isomers would be the next obvious candidates in the alcohol family, but their detection in hot cores will be challenging.

**Key words.** astrochemistry – line: identification – radio lines: ISM – ISM: molecules – ISM: individual objects: Sagittarius B2(N)

## 1. Introduction

The detection of a branched alkyl molecule, *iso*-propyl cyanide (*i*-C<sub>3</sub>H<sub>7</sub>CN), in the interstellar medium with the Atacama Large Millimeter/submillimeter Array (ALMA) opened a new window into the chemistry that takes place in star forming regions (Belloche et al. 2014). The production of such a branched molecule appears to require the addition of a functional group to a nonterminal carbon in the chain forming its backbone. This detection was made in the frame of our earlier imaging spectral line survey called Exploring Molecular Complexity with ALMA (EMOCA) that targeted the high-mass star forming protocluster Sagittarius (Sgr) B2(N) (Belloche et al. 2016). The analysis of the data surprisingly revealed that *iso*-propyl cyanide is nearly as abundant as its straight-chain isomer, *normal*-propyl cyanide (*n*-C<sub>3</sub>H<sub>7</sub>CN), which was detected earlier with the IRAM 30 m telescope (Belloche et al. 2009), with an abundance ratio between the two isomers of 0.4, determined based on our EMOCA data (Belloche et al. 2014). These findings suggested that branched

carbon-chain molecules may be generally abundant in the interstellar medium.

Since the discovery of *iso*-propyl cyanide, many new complex organic molecules (COMs), which are carbon-bearing molecules containing at least six atoms per definition (Herbst & van Dishoeck 2009), have been reported in the interstellar medium, including two polycyclic aromatic hydrocarbons (McGuire et al. 2021), but no other branched molecule has been identified. The astrochemical model MAGICKAL that we employed to interpret the observational results obtained for propyl cyanide suggested that for the next, more complex member of the alkyl cyanide family, butyl cyanide (C<sub>4</sub>H<sub>9</sub>CN), the branched isomers should even dominate over the straight chain form (Garrod et al. 2017). This was one of motivations for us to perform a new imaging spectral line survey of Sgr B2(N) with ALMA at higher angular resolution and with a higher sensitivity compared to EMOCA. One of the first results of this new survey, called Re-exploring Molecular Complexity with ALMA (ReMoCA), was the first interstel-

lar detection of urea,  $\text{NH}_2\text{C(O)NH}_2$ , and the confirmation of the interstellar detection of N-methylformamide,  $\text{CH}_3\text{NHCHO}$  (Belloche et al. 2019), which had initially been tentatively detected with EMOCA (Belloche et al. 2017).

While we have not been able to identify the isomers of butyl cyanide in the ReMoCA survey so far, we have systematically searched for all COMs that have been spectroscopically characterized in the laboratory and for which we had access to spectroscopic predictions in electronic format, in particular through spectroscopic databases such as the Cologne Database for Molecular Spectroscopy<sup>1</sup> (CDMS, Müller et al. 2005). Among these COMs, the alkanol family is of particular interest. Methanol,  $\text{CH}_3\text{OH}$ , and ethanol,  $\text{C}_2\text{H}_5\text{OH}$ , have long been known to exist in the interstellar medium. Both were first detected toward Sgr B2 at low angular resolution (Ball et al. 1970; Zuckerman et al. 1975). Our detailed study of alkanols with the EMOCA survey at  $1.6''$  resolution revealed that ethanol is 20 times less abundant than methanol in the secondary hot molecular core of Sgr B2(N), called Sgr B2(N2) (Müller et al. 2016). However, the EMOCA survey did not allow us to detect the next, more complex member of the alkanol family, propanol ( $\text{C}_3\text{H}_7\text{OH}$ ), neither in its *normal* form, nor in its *iso* form. We found that *normal*-propanol (*n*- $\text{C}_3\text{H}_7\text{OH}$ ), also called propan-1-ol, and *iso*-propanol (*i*- $\text{C}_3\text{H}_7\text{OH}$ ), also called propan-2-ol, are at least 8 and 22 times less abundant than ethanol in Sgr B2(N2) at the scale traced with EMOCA.

Here we present the search for both *normal*- and *iso*-propanol toward Sgr B2(N2) in the ReMoCA survey. *iso*-Propanol is not a branched alkyl molecule (it contains only three carbon atoms, which can only form a straight chain), but there are similarities between propanol and propyl cyanide in the sense that both molecules have a functional group (-OH or -CN) that can be attached to a terminal or middle atom of the carbon backbone. This motivates a comparison of these two families of COMs. The article is structured in the following way. Section 2 describes the observational setup, the method used to analyze the interferometric spectra, and the origin of the spectroscopic predictions employed to identify the detected lines and perform the radiative transfer calculations. Section 3 explains how we selected the position of the emission in the interferometric map for which the spectra were extracted and reports the detection of both *iso*- and *normal*-propanol, along with the results we obtained for methanol and ethanol. Section 4 presents the results of our astrochemical model with an expanded network that includes propanol. We discuss the results in Sect. 5 and lay out our conclusions in Sect. 6.

## 2. Observations and radiative transfer modeling

### 2.1. ALMA observations

The ReMoCA survey was performed toward Sgr B2(N) with ALMA in its cycle 4. Details about the observations and data reduction were published in Belloche et al. (2019). We summarize here only the main characteristics of the survey. The phase center was set at the equatorial position  $(\alpha, \delta)_{\text{J2000}} = (17^{\text{h}}47^{\text{m}}19^{\text{s}}.87, -28^{\circ}22'16''.0)$ . This position is located halfway between the two hot molecular cores Sgr B2(N1) and Sgr B2(N2). The frequency range from 84.1 GHz to 114.4 GHz was fully covered at a spectral resolution of 488 kHz ( $1.7$  to  $1.3 \text{ km s}^{-1}$ ) with five frequency tunings labeled S1–S5 in increasing frequency order. Each spectral setup consisted of four

spectral windows labeled W0–W3, with W0–W1 covering the lower sideband and W2–W3 covering the upper sideband. The angular resolution ranges from  $\sim 0.3''$  to  $\sim 0.8''$  (half-power beam width of synthesized beam, HPBW) with a median value of  $0.6''$  that corresponds to  $\sim 4900 \text{ au}$  at the distance of Sgr B2 (8.2 kpc, Reid et al. 2019). The survey achieved a sensitivity per spectral channel between  $0.35 \text{ mJy beam}^{-1}$  and  $1.1 \text{ mJy beam}^{-1}$  (rms) depending on the setup, with a median value of  $0.8 \text{ mJy beam}^{-1}$ . This corresponds to an rms brightness temperature noise level of  $0.27 \text{ K}$  for a  $0.6''$  HPBW at a frequency of  $100 \text{ GHz}$ . These sensitivities were measured with the program *go noise*, which is part of the GREG software in the GILDAS package<sup>2</sup> and fits the distribution of pixel intensities in each channel map. In this work, we used an improved version of the splitting of the line and continuum emission as we described in Melosso et al. (2020).

### 2.2. Radiative transfer modeling

The observed spectra were modeled assuming local thermodynamic equilibrium (LTE) with the astronomical software Weeds (Maret et al. 2011) which is part of the GILDAS package. The LTE assumption is justified by the high densities of the regions where hot-core emission is detected in Sgr B2(N) ( $> 1 \times 10^7 \text{ cm}^{-3}$ , see Bonfand et al. 2019). Weeds computes the radiative transfer by accounting for the line optical depth and the finite angular resolution of the observations. We derived a best-fit synthetic spectrum for each molecule separately, and then added the contributions of all identified molecules together. We used a set of five parameters to model the contribution of each species: size of the emitting region ( $\theta_s$ ), column density ( $N$ ), temperature ( $T_{\text{rot}}$ ), linewidth ( $\Delta V$ ), and velocity offset ( $V_{\text{off}}$ ) with respect to the assumed systemic velocity of the source.

### 2.3. Spectroscopy

For the radiative transfer calculations of the molecules analyzed in Sect. 3, we used spectroscopic predictions that we retrieved from the CDMS or that some of us produced in a companion article (Zingsheim et al. 2022). We used version 3 of the CDMS entry 32504 of methanol which is largely based on the study of Xu et al. (2008). Additional data of methanol in the range of our survey were taken from Lees & Baker (1968), Pickett et al. (1981), Sastry et al. (1984), Herbst et al. (1984), Anderson et al. (1990), and Müller et al. (2004). The partition function includes energies up to  $v_t = 3$ , which should be appropriate up to  $\sim 200 \text{ K}$  and still quite good at  $300 \text{ K}$ .

For ethanol, we used version 1 of the CDMS entry 46524 that is mainly based on Pearson et al. (2008), with modifications provided by Müller et al. (2016). These modifications were motivated by the EMOCA survey and resolve severe intensity issues. Additional laboratory data to Pearson et al. (2008) were contributed by Pearson et al. (1995, 1996, 1997). Contributions from ethanol in excited vibrational states were evaluated from the fundamental vibrations in Durig et al. (2011) employing the harmonic oscillator approximation. This approximation is usually the best in the absence of detailed information on the energies of overtone and combination states.

We used the CDMS entries 60518 and 60519 (both version 1) for the *gauche* and *anti* conformers of *iso*-propanol, respectively. Both of them are largely based on Maeda et al. (2006b). Contributions of excited vibrational states are based on Dobrowolski et al. (2008).

<sup>1</sup> <https://cdms.astro.uni-koeln.de/>

<sup>2</sup> See <http://www.iram.fr/IRAMFR/GILDAS>.

Calculations of the rotational spectra of the five conformers *Gauche-anti* (*Ga*), *Gauche-gauche* (*Gg*), *Gauche-gauche'* (*Gg'*), *Anti-anti* (*Aa*), and *Anti-gauche* (*Ag*) of *normal*-propanol were carried out in the context of our companion spectroscopic study (Zingsheim et al. 2022), which describes the *Aa* and *Ag* conformers. The spectroscopic predictions of *Ga*, *Gg*, and *Gg'* are based on Kisiel et al. (2010) with a large fraction of the *Ga* data from Maeda et al. (2006a). The partition function of *normal*-propanol was evaluated as described by Zingsheim et al. (2022). Briefly, the partition function was summed up over the *Ga*, *Gg*, and *Gg'* conformers, whose energies are accurately known (Kisiel et al. 2010). Conformational contributions of *Aa* and *Ag* were evaluated using their calculated energies (Kisiel et al. 2010). Contributions from excited vibrational states were estimated from the fundamental vibrations in Fukushima & Zwolinski (1968) employing the harmonic oscillator approximation as before.

### 3. Results

#### 3.1. Source selection

We used several prominent and uncontaminated lines of various COMs to explore the velocity structure of Sgr B2(N2), which is resolved with the ReMoCA observations. A detailed account of this investigation will be reported elsewhere (Belloche et al. in prep.). An outcome of this exploration is that the emission from the south-western part of Sgr B2(N2) is characterized by narrow lines, with a full width at half maximum (FWHM) as narrow as  $\sim 2$  km s<sup>-1</sup>. The narrowest lines are seen at the border of the molecular emission detected with ALMA and are thus weak. While narrow linewidths are key to reduce the spectral confusion that affects the spectra of Sgr B2(N) even in the 3 mm wavelength range, we also need positions with sufficiently strong emission in order to search for faint signals of low-abundance COMs. As a compromise, we selected the position indicated with a red cross in Fig. 1, which shows integrated intensity maps of selected transitions of ethanol that are not contaminated by other species and were observed with the highest angular resolution in the ReMoCA survey (setup S5). This position has equatorial offsets of  $(-0.48'', +2.40'')$  with respect to the phase center, i.e. an equatorial position  $(\alpha, \delta)_{J2000} = (17^{\text{h}}47^{\text{m}}19^{\text{s}}.83, -28^{\circ}22'13''.6)$ . We call this position Sgr B2(N2b). The COM lines detected toward Sgr B2(N2b) have a FWHM of 3.5 km s<sup>-1</sup>. The systemic velocity toward Sgr B2(N2b) is  $V_{\text{lsr}} = 74.2$  km s<sup>-1</sup>. The green crosses displayed in Fig. 1 mark the peak positions of the continuum sources identified by Sánchez-Monge et al. (2017) at 1.2 mm with ALMA.

#### 3.2. Column densities of methanol and ethanol

Methanol and ethanol are both clearly detected in their vibrational ground state toward Sgr B2(N2b), and lines from the former are also detected in its first two torsionally excited states (see Figs. A.1–A.5). Rotational lines from within the third torsionally excited state of methanol contribute to the observed spectrum but none is sufficiently free of contamination from other species to secure the identification of this state. We selected the transitions that have optical depths lower than 2 and are not too contaminated by emission from other species to build population diagrams for both molecules (see Figs. B.1 and B.2). In both diagrams the data indicate a single temperature component. Linear fits to these diagrams yield rotational temperatures of  $138.4 \pm 1.7$  K and  $133.9 \pm 1.2$  K for methanol and ethanol,

**Table 1.** Rotational temperature of methanol, ethanol, *g-i*-propanol, *a-i*-propanol, *Gg'-n*-propanol, and *Ag-n*-propanol derived from their population diagrams toward Sgr B2(N2b).

Molecule	States <sup>(a)</sup>	$T_{\text{fit}}^{(b)}$ (K)
CH <sub>3</sub> OH	$v = 0, v_t = 1, v_t = 2, v_t = 3$	138.4 (1.7)
C <sub>2</sub> H <sub>5</sub> OH	$v = 0$	133.9 (1.2)
<i>g-i</i> -C <sub>3</sub> H <sub>7</sub> OH	$v = 0$	80 (220)
<i>a-i</i> -C <sub>3</sub> H <sub>7</sub> OH	$v = 0$	110 (220)
<i>Gg'-n</i> -C <sub>3</sub> H <sub>7</sub> OH	$v = 0$	69 (62)
<i>Ag-n</i> -C <sub>3</sub> H <sub>7</sub> OH	$v = 0$	70 (34)

**Notes.** <sup>(a)</sup> Vibrational states that were taken into account to fit the population diagram. <sup>(b)</sup> The standard deviation of the fit is given in parentheses. As explained in Sect. 3 of Belloche et al. (2016) and in Sect. 4.4 of Belloche et al. (2019), this uncertainty is purely statistical and should be viewed with caution. It may be underestimated.

respectively, as reported in Table 1. We computed LTE synthetic spectra of methanol and ethanol assuming temperatures of 140 K and 135 K, respectively. Given the relatively compact morphology of the ethanol emission shown in Fig. 1, we assumed a size of the emitting region toward Sgr B2(N2b) of 0.5'' and then adjusted the column density until a good match between data and model was achieved for the lines that are not too optically thick. Very optically thick lines cannot be properly modeled with our simple approach that does not account for the structure of the emission along the line of sight. Besides, a few lines of methanol are masers (such as the  $5_{-1} - 4_0$  *E* line at 84521 MHz, see, e.g., Müller et al. 2004) or show a combination of absorption and emission and cannot be modeled adequately under the LTE approximation.

The results of our LTE modeling are reported in Table 2. We find an abundance ratio of methanol to ethanol of 19 toward Sgr B2(N2b), in very good agreement with the ratio of 20 obtained at lower angular resolution ( $\sim 1.6''$ ) with the EMOCA survey toward Sgr B2(N2) (Müller et al. 2016).

The CDMS spectroscopic entry of ethanol (and its associated partition function) contains rotational transitions from its two conformers, *anti* and *gauche*. It accounts for their conformational energy difference ( $\Delta E/k = 58$  K), the *gauche* conformer being higher in energy than the *anti* conformer. This means that our synthetic spectrum of ethanol assumes the relative populations of its conformers to be in thermodynamic equilibrium. The population diagram shown in Fig. B.2 displays the two conformers in different colors (black for *anti* and blue for *gauche*). The fact that the black and blue data points in this figure are well fitted with a single straight line clearly demonstrates that the assumption of thermodynamic equilibrium between conformers is valid for the high-density conditions of Sgr B2(N2b). Therefore, a single set of LTE parameters is sufficient to describe the level populations of ethanol in all its conformational states and it is adequate to fit its complete spectrum with this single set of parameters.

#### 3.3. Detection of *iso*-propanol

In order to search for both the *gauche* and *anti* conformers of *iso*-propanol, we assumed the same size of the emitting region, rotational temperature, linewidth, and velocity offset as for ethanol. The only parameter that was variable was the total column density of the molecule. Given that the spectroscopic predictions of *g-i*-C<sub>3</sub>H<sub>7</sub>OH and *a-i*-C<sub>3</sub>H<sub>7</sub>OH account for their relative en-

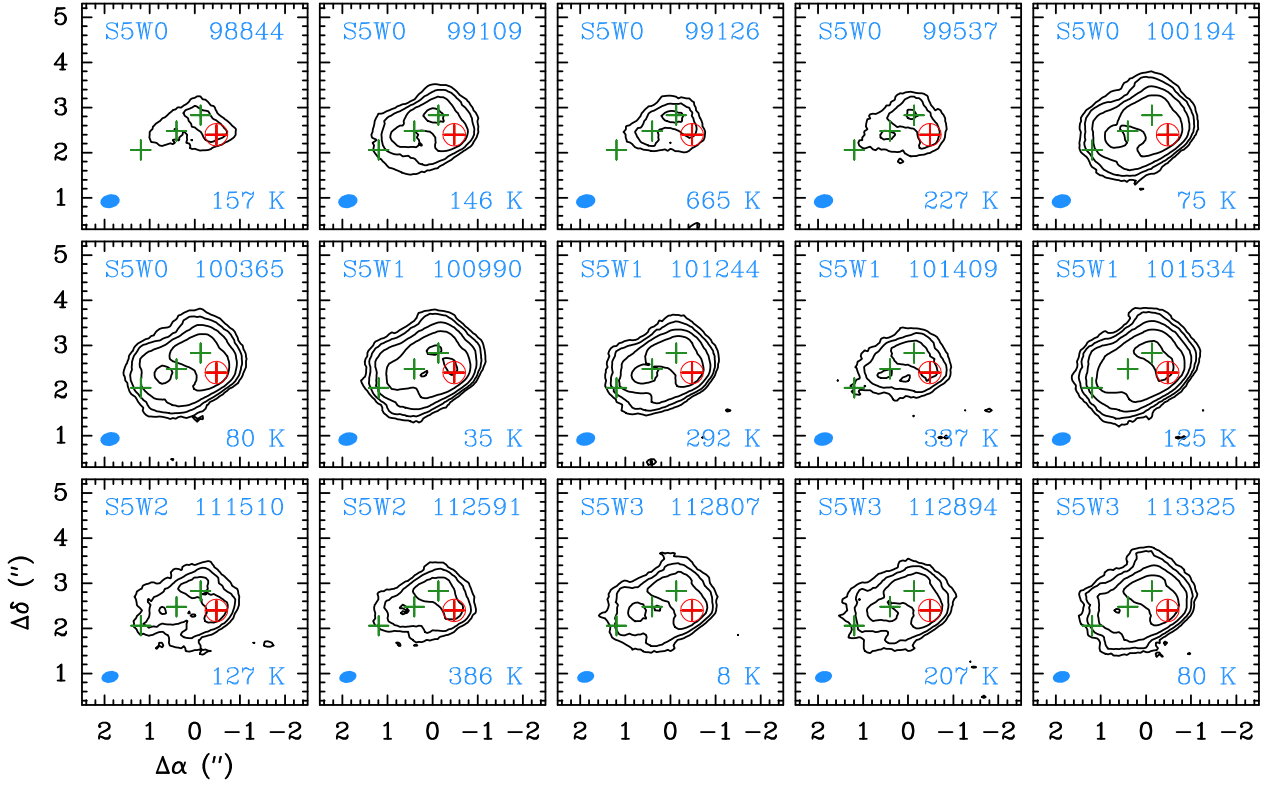


**Fig. 1.** Integrated intensity maps of selected transitions of ethanol detected toward Sgr B2(N2) in the ReMoCA survey. The equatorial offsets are defined with respect to the phase center of the survey (see its coordinates in Sect. 2.1). In each panel, the contours start at  $6\sigma$  with  $\sigma$  the noise level of the integrated intensity map, and they increase by a factor of two at each step. The red cross indicates the position of Sgr B2(N2b) and the red circle shows the intrinsic full-width at half maximum assumed to model the emission of Sgr B2(N2b). The green crosses from right to left mark the positions of the dust continuum sources AN02, AN03, and AN06 obtained with ALMA by Sánchez-Monge et al. (2017). The blue ellipse shows the half-power beam width of the ReMoCA survey. The setup (S) and its spectral window (W) are given in the top left corner of each panel with the same numbering as in Table 2 of Belloche et al. (2019). The frequency (in MHz) and upper-level energy (in temperature unit) of the ethanol line are indicated in the top right and bottom right corners, respectively. The integration ranges were optimized for Sgr B2(N2b) and do not necessarily include all the ethanol emission toward the other positions.

ergy, the two conformers can be modeled separately using the same column density parameter. It corresponds to the total column density of the molecule after accounting for the vibrational correction to the partition function that is purely rotational in the CDMS entries of these species. As was shown in Sect. 3.2 for ethanol, assuming that the conformers of a given molecule have relative populations consistent with thermodynamic equilibrium is valid for Sgr B2(N2b). Therefore, it is natural to expect the emission of both conformers of *iso*-propanol to be described with a single set of LTE parameters applied to the molecule as a whole. As a result, we did not fit the two conformers independently of each other but rather produced consistent synthetic spectra using a single set of LTE parameters.

The transitions of the *gauche* and *anti* conformers that are covered by the ReMoCA survey and are expected to contribute significantly to the spectrum of Sgr B2(N2b) on the basis of our LTE model are displayed in Figs. A.6 and A.7, respectively. Transitions that are too heavily blended with much stronger emission from other molecules and therefore cannot contribute to the identification of *iso*-propanol are not shown in these figures. A close inspection of these figures reveals a handful of lines that appear to be detected for each conformer. They are marked with green stars in these figures, and are shown specifically in Figs. 2 and 3 for the *gauche* and *anti* conformers, respectively.

Four spectral lines of *g-i*-C<sub>3</sub>H<sub>7</sub>OH and three spectral lines of *a-i*-C<sub>3</sub>H<sub>7</sub>OH are sufficiently strong and sufficiently free of contamination from other species to be considered as detected. Their

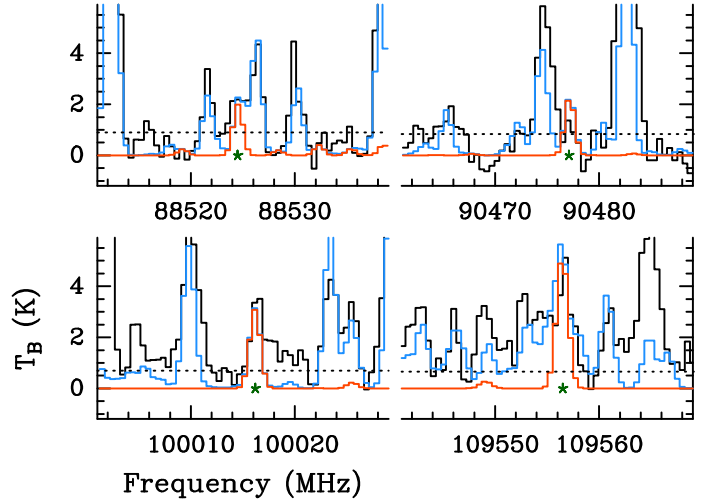


**Fig. 2.** Spectral lines of *gauche* *iso*-propanol detected in the ReMoCA survey toward Sgr B2(N2b). The best-fit LTE synthetic spectrum of *g-i*-C<sub>3</sub>H<sub>7</sub>OH is displayed in red and overlaid on the observed spectrum of Sgr B2(N2b) shown in black. The blue synthetic spectrum contains the contributions of all molecules identified in our survey so far, including propanol. The dotted line indicates the  $3\sigma$  noise level. The green stars mark the lines listed as detected in Table 3.

spectroscopic parameters are listed in Table 3, along with their

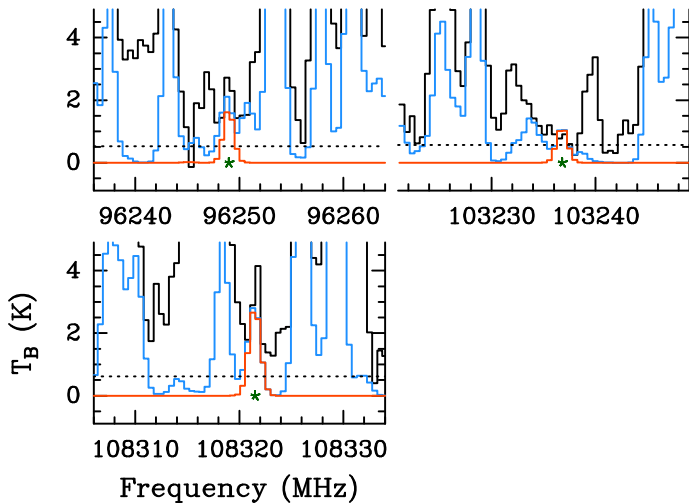


**Fig. 3.** Spectral lines of *anti iso*-propanol detected in the ReMoCA survey toward Sgr B2(N2b). The best-fit LTE synthetic spectrum of *a-i*-C<sub>3</sub>H<sub>7</sub>OH is displayed in red and overlaid on the observed spectrum of Sgr B2(N2b) shown in black. The blue synthetic spectrum contains the contributions of all molecules identified in our survey so far, including propanol. The dotted line indicates the  $3\sigma$  noise level. The green stars mark the lines listed as detected in Table 3.

integrated intensities and signal-to-noise ratios. This gives a total number of detected lines of seven for *iso-propanol*. Given that our analysis carefully accounts for the contamination from all other species identified so far toward Sgr B2(N2b) (the blue spectra shown in all figures), we consider that the detection of these seven spectral lines, whose relative intensities can be reproduced with a single combination of column density and rotational temperature, is sufficient to claim a secure detection of *iso-propanol* in Sgr B2(N2b). This is to our knowledge the first interstellar detection of this molecule.

We built population diagrams for both conformers, using the detected transitions as well as a few other transitions that are a bit more contaminated by the emission of other species that can be removed on the basis of our full LTE model of Sgr B2(N2b). These diagrams are shown in Figs. B.3 and B.4. In both cases, the covered range of upper-level energy is unfortunately too narrow to set meaningful constraints on the rotational temperature. The formal results of the fits to these diagrams are reported in Table 1 but the uncertainties are much too high to provide any robust insight into the rotational temperature of *iso-propanol*. This justifies our choice to fix the rotational temperature to the value derived for ethanol in order to model the emission of *iso-propanol*.

We obtained a total column density of  $1.3 \times 10^{17} \text{ cm}^{-2}$  for *iso-propanol*, which indicates that *iso-propanol* is  $\sim 600$  and  $\sim 30$  times less abundant than methanol and ethanol toward Sgr B2(N2b), respectively (Table 2). Our earlier detailed study of alkanols in Sgr B2(N2) at lower angular resolution with EMoCA resulted in a nondetection of *iso-propanol*, with an upper limit indicating that *iso-propanol* was at least  $\sim 20$  times less abundant than ethanol (Müller et al. 2016). This earlier nondetection is fully consistent with the ratio that we now obtain with ReMoCA. This shows that the high sensitivity and angular resolution of the ReMoCA survey was essential in revealing the presence of *iso-propanol* in the interstellar medium.

A small discrepancy affects the spectral line displayed in the top right panel of Fig. 2. In addition to the fact that this discrepancy is at the  $2\sigma$  level only, it seems that the level of the base-

line may have been slightly overestimated because a number of channels in the displayed frequency range have negative intensities that do not look random. Therefore, we consider that this discrepancy is insignificant and does not affect our identification of the *gauche* conformer of *iso-propanol*.

### 3.4. Detection of normal-propanol

We proceeded in the same way as for *iso-propanol* in order to search for the five conformers of *normal-propanol*. In particular, like for ethanol (Sect. 3.2) and *iso-propanol* (Sect. 3.3), we assumed that the relative populations of these five conformers are in thermodynamic equilibrium and that the emission of the molecule can be described with a single set of LTE parameters. Figures A.8–A.12 show the transitions of the *Gauche-anti*, *Gauche-gauche*, *Gauche-gauche'*, *Anti-anti*, and *Anti-gauche* conformers of *normal-propanol* that are covered by the ReMoCA survey and are expected to contribute significantly to the spectrum of Sgr B2(N2b) on the basis of our LTE model. Here again, transitions that are too heavily blended with much stronger emission from other molecules and therefore cannot contribute to the identification of *iso-propanol* are not shown in these figures. A close inspection of these figures reveals that a handful of spectral lines of the *Gauche-gauche'* and *Anti-gauche* conformers are detected toward Sgr B2(N2b). They are marked with green stars in these figures and displayed separately in Figs. 4 and 5, respectively. All the transitions of the other conformers are either too weak or too much contaminated by the emission of other species to be clearly identified.

Eight spectral lines of *Gg'-n*-C<sub>3</sub>H<sub>7</sub>OH and five spectral lines of *Ag-n*-C<sub>3</sub>H<sub>7</sub>OH are sufficiently strong and sufficiently free of contamination from other species to be considered as detected. Their spectroscopic parameters are listed in Table 3, along with their integrated intensities and signal-to-noise ratios. This gives a total number of detected lines of 13 for *normal-propanol*. As for *iso-propanol*, we consider this number of detected lines as sufficient to claim a robust detection of *normal-propanol* toward Sgr B2(N2b). This is to our knowledge the first secure detection of *normal-propanol* toward a hot core<sup>3</sup>.

As for *iso-propanol*, the population diagrams built for *normal-propanol* are too scarce to provide any meaningful constraints on the rotational temperature of its emission (see Figs. B.5–B.6 and Table 1). This again justifies our choice to use the same temperature as derived for ethanol in order to model the emission of *normal-propanol*.

We obtained a total column density of  $2.8 \times 10^{17} \text{ cm}^{-2}$  for *normal-propanol*, which indicates that *normal-propanol* is  $\sim 350$  and  $\sim 20$  times less abundant than methanol and ethanol toward Sgr B2(N2b), respectively (Table 2). Our earlier detailed study of alkanols at lower angular resolution with EMoCA resulted in a nondetection of *normal-propanol* in Sgr B2(N2), with an upper limit indicating that *normal-propanol* was at least  $\sim 8$  times less abundant than ethanol (Müller et al. 2016). Like in the case of *iso-propanol*, this earlier nondetection is fully consistent with the ratio that we now obtain with ReMoCA.

The synthetic spectra computed for the other three conformers of *normal-propanol* with the column density derived above are, under the assumption of thermodynamic equilibrium, fully consistent with the ReMoCA spectrum (see Figs. A.8, A.9, and

<sup>3</sup> The first interstellar detection of *normal-propanol* was reported by Jimenez-Serra et al. (2022) toward the molecular cloud G+0.693–0.027 during the refereeing process of this article. This source is thought to be a region dominated by shocks and is not a hot core.

**Table 2.** Parameters of our best-fit LTE model of methanol, ethanol, *normal*-propanol, and *iso*-propanol toward Sgr B2(N2b).

Molecule	Status <sup>(a)</sup>	$N_{\text{det}}$ <sup>(b)</sup>	Size <sup>(c)</sup> ( $''$ )	$T_{\text{rot}}$ <sup>(d)</sup> (K)	$N$ <sup>(e)</sup> ( $\text{cm}^{-2}$ )	$F_{\text{vib}}$ <sup>(f)</sup>	$F_{\text{conf}}$ <sup>(g)</sup>	$\Delta V$ <sup>(h)</sup> ( $\text{km s}^{-1}$ )	$V_{\text{off}}$ <sup>(i)</sup> ( $\text{km s}^{-1}$ )	$\frac{N_{\text{ref}}}{N}$ <sup>(j)</sup>
$\text{CH}_3\text{OH}, v = 0^*$	d	48	0.5	140	8.0 (19)	1.00	–	3.5	0.0	1
$v_t = 1$	d	15	0.5	140	8.0 (19)	1.00	–	3.5	0.0	1
$v_t = 2$	d	6	0.5	140	8.0 (19)	1.00	–	3.5	0.0	1
$v_t = 3$	t	0	0.5	140	8.0 (19)	1.00	–	3.5	0.0	1
$\text{C}_2\text{H}_5\text{OH}, v = 0$	d	271	0.5	135	4.2 (18)	1.24	–	3.5	0.0	19
<i>Ga-n</i> - $\text{C}_3\text{H}_7\text{OH}, v = 0$	n	0	0.5	135	2.3 (17)	1.57	1.44	3.5	0.0	350
<i>Gg-n</i> - $\text{C}_3\text{H}_7\text{OH}, v = 0$	n	0	0.5	135	2.3 (17)	1.57	1.44	3.5	0.0	350
<i>Gg'-n</i> - $\text{C}_3\text{H}_7\text{OH}, v = 0$	d	8	0.5	135	2.3 (17)	1.57	1.44	3.5	0.0	350
<i>Aa-n</i> - $\text{C}_3\text{H}_7\text{OH}, v = 0$	n	0	0.5	135	2.3 (17)	1.57	1.44	3.5	0.0	350
<i>Ag-n</i> - $\text{C}_3\text{H}_7\text{OH}, v = 0$	d	5	0.5	135	2.3 (17)	1.57	1.44	3.5	0.0	350
<i>g-i</i> - $\text{C}_3\text{H}_7\text{OH}, v = 0$	d	4	0.5	135	1.3 (17)	1.42	–	3.5	0.0	630
<i>a-i</i> - $\text{C}_3\text{H}_7\text{OH}, v = 0$	d	3	0.5	135	1.3 (17)	1.42	–	3.5	0.0	630

**Notes.** <sup>(a)</sup> d: detection, t: tentative detection, n: nondetection. <sup>(b)</sup> Number of detected lines (conservative estimate, see Sect. 3 of Belloche et al. 2016). One line of a given species may mean a group of transitions of that species that are blended together. <sup>(c)</sup> Source diameter (*FWHM*). <sup>(d)</sup> Rotational temperature. <sup>(e)</sup> Total column density of the molecule.  $x$  ( $y$ ) means  $x \times 10^y$ . An identical value for all listed vibrational/torsional states of a molecule means that LTE is an adequate description of the vibrational/torsional excitation. <sup>(f)</sup> Correction factor that was applied to the column density to account for the contribution of vibrationally excited states, in the cases where this contribution was not included in the partition function of the spectroscopic predictions. <sup>(g)</sup> Correction factor that was applied to the column density to account for the contribution of other conformers in the cases where this contribution could be estimated but was not included in the partition function of the spectroscopic predictions. <sup>(h)</sup> Linewidth (*FWHM*). <sup>(i)</sup> Velocity offset with respect to the assumed systemic velocity of Sgr B2(N2b),  $V_{\text{sys}} = 74.2 \text{ km s}^{-1}$ . <sup>(j)</sup> Column density ratio, with  $N_{\text{ref}}$  the column density of the previous reference species marked with a  $\star$ .

A.11). All transitions of these conformers that are not too weak unfortunately fall at frequencies where other molecules emit more strongly, which prevents the identification of these conformers in the spectrum toward Sgr B2(N2b). The synthetic spectrum of *normal*-propanol at the frequencies of several transitions of the *Gauche-anti* conformer shown in Fig. A.8 is close to the signal detected at these frequencies. A column density of *normal*-propanol twice as high as the value determined above would not be consistent anymore (see, e.g., the transitions at 94747, 99937, 102182, or 106120 MHz). Similarly, a column density of *normal*-propanol twice as high as the value determined above would, for some transitions of the *Gauche-gauche* conformer shown in Fig. A.9, not be consistent with the observed spectrum anymore (transitions at, e.g., 100696 MHz and 106248 MHz). The case of the *Anti-anti* conformer is less constraining, with an upper limit set by the transition at 95506 MHz in Fig. A.11 about three times as high as the value derived above.

### 3.5. Abundance ratio of *iso*-propanol and *normal*-propanol

The column densities reported in Table 2 imply that *iso*-propanol is twice less abundant than *normal*-propanol toward Sgr B2(N2b) ( $[\text{iso}]/[\text{normal}] = 0.6$ ). This is close to the isomeric ratio  $[\text{iso}]/[\text{normal}] = 0.4$  that we obtained for propyl cyanide,  $\text{C}_3\text{H}_7\text{CN}$ , at lower angular resolution toward Sgr B2(N2) with the EMOCA survey (Belloche et al. 2014).

## 4. Astrochemical modeling

In order to understand the relative ratios of the *iso* and *normal* forms of propanol detected in our survey, we have run astrochemical models simulating the chemistry occurring during the cold collapse of the core and the subsequent warm-up to typical hot-core temperatures. These simulations use the three-phase, gas-grain astrochemical kinetics code MAGICKAL (Garrod 2013). The models presented here build upon the hot-core models of Garrod et al. (2022), using those authors' *final*

model setup. Along with more typical gas-phase processes, the code employs the most up-to-date treatment of grain-surface and bulk-ice chemistry. This includes not only diffusive surface reaction processes, but – crucially – a range of non-diffusive reaction mechanisms that can occur both on the grain/ice surfaces and within the bulk ice mantles (Jin & Garrod 2020).

Diffusive reactions occur when one or other reactant is able to diffuse thermally on the grain/ice surface, allowing them to meet and react. In the non-diffusive case, some other process brings the reactants together to allow the same reaction to occur. Thus, in general, it is only the mechanism by which a meeting occurs that differentiates diffusive from non-diffusive reactions, rather than the underlying reaction network (with the limited exception of the so-called three-body excited formation mechanism, 3-BEF, see Jin & Garrod 2020). However, the reaction rates of non-diffusive reactions take on an entirely different form from their diffusive counterparts, and can allow reactions between species of low thermal mobility to occur even at very low temperatures.

Two main non-diffusive mechanisms considered in the model are: (i) photodissociation-induced (PDI) reactions, in which the photodissociation of a grain-surface/ice molecule in the presence of some other chemical species results in the latter being able to react with one of the photo-products; and (ii) three-body (3-B) reactions, in which a preceding two-body reaction on the grain occurs in the presence of some other chemical species with which the reaction product may itself react. In the latter case, the preceding reaction could itself be diffusive or non-diffusive. The PDI and 3-B processes may take place both on the grain/ice surfaces and within the bulk ice mantle. The Eley-Rideal process is also included in the model, whereby an atom or molecule adsorbing onto the grain surface from the gas phase immediately meets its reaction partner upon adsorption; however, this mechanism is generally of small significance.

Whether occurring as diffusive or non-diffusive processes, reactions with activation energy barriers may experience low efficiency if the reactants are able to diffuse away from each other



**Table 3.** Spectroscopic parameters and integrated intensities of transitions of *iso*-propanol and *normal*-propanol detected toward Sgr B2(N2b) in the ReMoCA survey.

Transition $J_{K_a,K_c}$	Frequency (MHz)	$\Delta f^{(a)}$ (kHz)	$A_{ul}^{(b)}$ ( $10^{-5} \text{ s}^{-1}$ )	$E_u^{(c)}$ (K)	$g_u^{(d)}$	$I_{\text{obs}}^{(e)}$ (K km s $^{-1}$ )	$I_{\text{mod}}^{(f)}$ (K km s $^{-1}$ )	$I_{\text{all}}^{(g)}$	$\frac{S_{\text{obs}}^{(h)}}{N}$	$\frac{S_{\text{dec}}^{(i)}}{N}$	$\frac{S_{\text{mod}}^{(j)}}{N}$
<i>g-i</i> -C <sub>3</sub> H <sub>7</sub> OH, $v = 0$											
13 <sub>1,12,0</sub> – 12 <sub>1,11,1</sub>	88524.536	6	0.43	48.2	27	10.6(9)	7.1	9.1	12	10	8.3
13 <sub>2,12,0</sub> – 12 <sub>2,11,1</sub>	88524.536	6	0.43	48.2	27	–	–	–	–	–	–
14 <sub>0,14,0</sub> – 13 <sub>0,13,1</sub>	90477.172	7	0.51	50.4	29	5.3(9)	8.6	9.1	5.9	5.4	9.5
14 <sub>1,14,0</sub> – 13 <sub>1,13,1</sub>	90477.172	7	0.51	50.4	29	–	–	–	–	–	–
15 <sub>0,15,0</sub> – 14 <sub>0,14,1</sub>	100016.165	7	0.68	57.5	31	13.8(7)	11.0	11.4	21	20	16
15 <sub>1,15,0</sub> – 14 <sub>1,14,1</sub>	100016.165	7	0.68	57.5	31	–	–	–	–	–	–
16 <sub>0,16,0</sub> – 15 <sub>0,15,1</sub>	109556.465	7	0.91	65.0	33	18.8(6)	18.5	23.3	32	24	32
16 <sub>1,16,0</sub> – 15 <sub>1,15,1</sub>	109556.465	7	0.91	65.0	33	–	–	–	–	–	–
<i>a-i</i> -C <sub>3</sub> H <sub>7</sub> OH, $v = 0$											
9 <sub>1,8</sub> – 8 <sub>2,7</sub>	96248.969	4	0.80	144.9	19	12.1(5)	6.3	9.5	22	17	12
9 <sub>2,8</sub> – 8 <sub>1,7</sub>	96248.969	4	0.80	144.9	19	–	–	–	–	–	–
9 <sub>2,7</sub> – 8 <sub>3,6</sub>	103236.772	3	0.86	147.4	19	4.6(5)	4.2	4.4	8.5	8.1	7.8
9 <sub>3,7</sub> – 8 <sub>2,6</sub>	103236.795	3	0.86	147.4	19	–	–	–	–	–	–
11 <sub>0,11</sub> – 10 <sub>1,10</sub>	108321.482	4	1.32	152.0	23	14.3(6)	10.2	10.9	26	24	18
11 <sub>1,11</sub> – 10 <sub>0,10</sub>	108321.482	4	1.32	152.0	23	–	–	–	–	–	–
<i>Gg'-n</i> -C <sub>3</sub> H <sub>7</sub> OH, $v = 0$											
9 <sub>1,8,2</sub> – 8 <sub>1,7,2</sub>	85495.771	2	0.65	94.4	76	4.1(8)	3.3	3.3	5.0	4.9	3.9
10 <sub>0,10,2</sub> – 9 <sub>0,9,2</sub>	88171.422	3	0.72	96.9	84	5.6(9)	3.8	4.4	6.5	5.9	4.5
10 <sub>2,9,2</sub> – 9 <sub>2,8,2</sub>	91872.157	2	0.78	99.4	84	7.4(9)	4.6	5.9	8.5	6.9	5.2
10 <sub>6,5,2</sub> – 9 <sub>6,4,2</sub>	93322.983	2	0.55	114.4	84	6.4(9)	5.8	6.4	7.5	6.8	6.8
10 <sub>6,4,2</sub> – 9 <sub>6,3,2</sub>	93323.050	2	0.55	114.4	84	–	–	–	–	–	–
11 <sub>2,10,2</sub> – 10 <sub>2,9,2</sub>	100777.598	2	1.04	104.3	92	5.7(7)	5.6	5.7	7.6	7.6	7.6
11 <sub>5,7,2</sub> – 10 <sub>5,6,2</sub>	102774.297	2	0.88	114.2	92	5.4(5)	4.0	5.4	10	7.4	7.3
11 <sub>1,10,2</sub> – 10 <sub>1,9,2</sub>	103092.965	2	1.14	103.9	92	8.0(5)	4.9	4.9	17	17	11
12 <sub>4,9,2</sub> – 11 <sub>4,8,2</sub>	112758.561	2	1.12	115.6	100	14.3(26)	8.7	12.0	5.6	4.3	3.4
<i>Ag-n</i> -C <sub>3</sub> H <sub>7</sub> OH, $v = 0$											
13 <sub>0,13,3</sub> – 12 <sub>0,12,3</sub>	94296.615	40	0.61	97.0	54	5.0(8)	4.4	4.6	5.9	5.6	5.2
13 <sub>0,13,2</sub> – 12 <sub>0,12,2</sub>	94297.251	40	0.61	97.0	54	–	–	–	–	–	–
13 <sub>6,7,0</sub> – 12 <sub>6,6,0</sub>	94959.841	40	0.49	136.0	54	3.5(7)	2.5	2.6	4.9	4.8	3.5
13 <sub>6,8,0</sub> – 12 <sub>6,7,0</sub>	94959.841	40	0.49	136.0	54	–	–	–	–	–	–
14 <sub>5,9,0</sub> – 13 <sub>5,8,0</sub>	102271.836	40	0.68	129.0	58	6.4(5)	3.4	5.4	12	8.0	6.3
14 <sub>5,10,0</sub> – 13 <sub>5,9,0</sub>	102271.836	40	0.68	129.0	58	–	–	–	–	–	–
14 <sub>2,12,3</sub> – 13 <sub>2,11,3</sub>	102855.519	40	0.78	106.4	58	3.4(5)	2.1	2.3	7.2	6.9	4.5
15 <sub>5,10,1</sub> – 14 <sub>5,9,1</sub>	109618.830	40	0.86	134.3	62	8.0(7)	6.3	9.2	12	7.8	9.6
15 <sub>5,11,1</sub> – 14 <sub>5,10,1</sub>	109618.830	40	0.86	134.3	62	–	–	–	–	–	–

**Notes.** <sup>(a)</sup> Frequency uncertainty. <sup>(b)</sup> Einstein coefficient for spontaneous emission. <sup>(c)</sup> Upper-level energy. <sup>(d)</sup> Upper-level degeneracy. <sup>(e)</sup> Integrated intensity of the observed spectrum in brightness temperature scale. The statistical standard deviation is given in parentheses in unit of the last digit. <sup>(f)</sup> Integrated intensity of the synthetic spectrum of propanol. <sup>(g)</sup> Integrated intensity of the model that contains the contribution of all identified molecules, including propanol. <sup>(h)</sup> Signal-to-noise ratio of  $I_{\text{obs}}$ . <sup>(i)</sup> Signal-to-noise ratio of the integrated intensity,  $I_{\text{dec}}$ , decontaminated from the contribution of molecules other than propanol, i.e.  $I_{\text{dec}} = I_{\text{obs}} - (I_{\text{all}} - I_{\text{mod}})$ , computed with the uncertainty of  $I_{\text{obs}}$ . <sup>(j)</sup> Signal-to-noise ratio of  $I_{\text{mod}}$  computed with the uncertainty of  $I_{\text{obs}}$ . In the last six columns, a value followed by a dash in the next row represents the value obtained for a group of transitions that are not resolved in the astronomical spectrum.

before reaction occurs. However, in cases where the reactants are completely immobile, a slow, barrier-mediated reaction may occur with high efficiency – for example, when bulk-ice photodissociation leads to a photo-product radical being trapped in the ice next to a stable molecule, with which it may react after overcoming an activation energy barrier.

One further noteworthy adjustment made in the Garrod et al. (2022) model is the removal of the bulk-diffusion process for species other than H and H<sub>2</sub>; aside from these two, bulk species are deemed to be too bulky to diffuse via interstitial hopping within the ice structure. Consequently, atomic H and H<sub>2</sub> are the

only species whose diffusion may lead to reactions in the bulk. Non-diffusive mechanisms nevertheless allow reactions in the bulk ice to proceed.

The model of Garrod et al. (2022) included an expanded reaction network, which we further extend to include propanol. We also update several of the reactions relating to the chemistry of *normal*- and *iso*-propyl cyanide (Garrod et al. 2017). The new network is described in more detail in Sect. 4.1.

The physical conditions used in the models follow past simulations, beginning with a cold collapse stage in which the gas density,  $n_{\text{H}}$ , increases from  $3 \times 10^3$  to  $2 \times 10^8 \text{ cm}^{-3}$  over a pe-

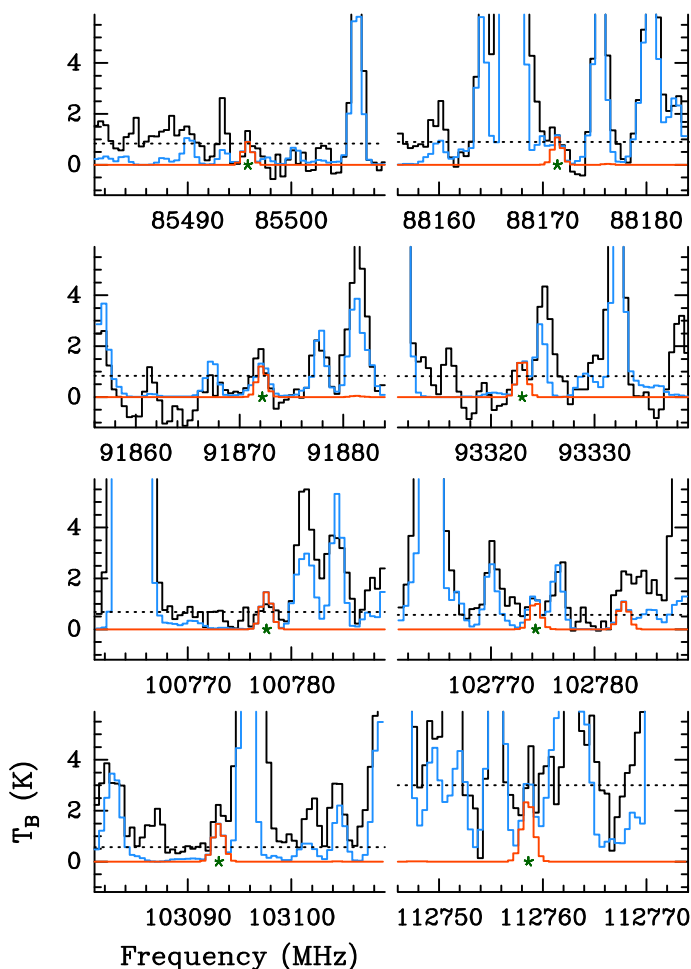


**Fig. 4.** Spectral lines of *Gauche-gauche'* normal-propanol detected in the ReMoCA survey toward Sgr B2(N2b). The best-fit LTE synthetic spectrum of *Gg'-n-C*<sub>3</sub>H<sub>7</sub>OH is displayed in red and overlaid on the observed spectrum of Sgr B2(N2b) shown in black. The blue synthetic spectrum contains the contributions of all molecules identified in our survey so far, including propanol. The dotted line indicates the  $3\sigma$  noise level. The green stars mark the lines listed as detected in Table 3.

riod of approximately 1 Myr, under free-fall collapse. Due to the gradual increase in visual extinction (3 to 500 magnitudes), the dust temperature falls from  $\sim 14.7$  K to a fixed lower limit of 8 K, following the relationship of Garrod & Pauly (2011). The collapse is halted when the desired density is reached; a warm-up stage then ensues at fixed gas density, in which the coupled gas and dust temperatures gradually rise to a final value of 400 K, at which point the model ends. We use the same three warm-up timescales as in past models: *fast*, *medium*, and *slow*, corresponding to characteristic timescales of  $5 \times 10^4$ ,  $2 \times 10^5$ , and  $1 \times 10^6$  yr taken to reach a representative hot-core temperature of 200 K (more detail is provided by Garrod & Herbst 2006; Garrod 2013). We assume here that the *slow* model is most relevant to Sgr B2(N), based on its better match to observational data in past comparisons.

#### 4.1. Reaction network

We constructed a new sub-network of chemical reactions for propanol that was added to our existing chemical network derived from Garrod et al. (2022). This new network is not the first to consider propanol in the ISM; Charnley et al. (1995) pre-

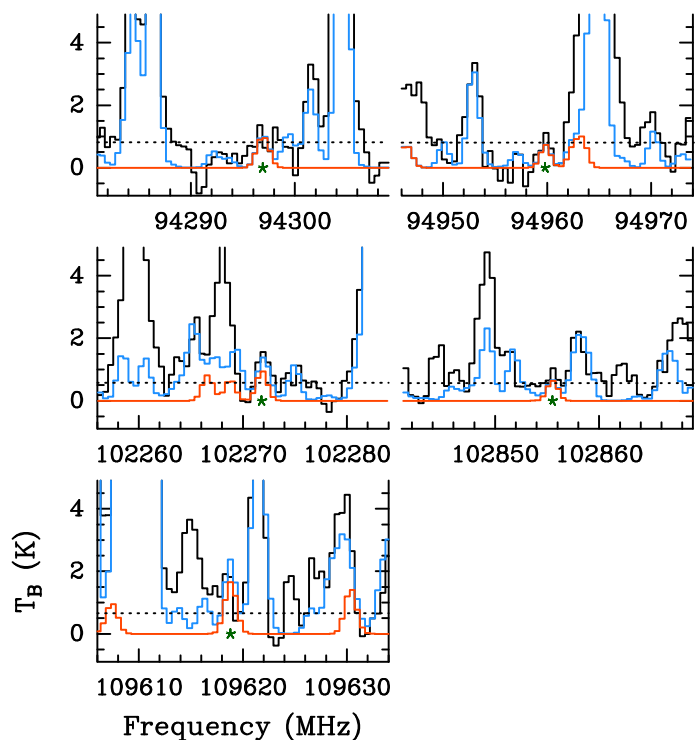


**Fig. 5.** Spectral lines of *Anti-gauche* normal-propanol detected in the ReMoCA survey toward Sgr B2(N2b). The best-fit LTE synthetic spectrum of *Ag-n-C*<sub>3</sub>H<sub>7</sub>OH is displayed in red and overlaid on the observed spectrum of Sgr B2(N2b) shown in black. The blue synthetic spectrum contains the contributions of all molecules identified in our survey so far, including propanol. The dotted line indicates the  $3\sigma$  noise level. The green stars mark the lines listed as detected in Table 3.

sented a gas-phase chemical model of hot cores in which both *n-C*<sub>3</sub>H<sub>7</sub>OH and *i-C*<sub>3</sub>H<sub>7</sub>OH were presumed to form on dust grains, before being thermally released into the gas phase where they were destroyed. Those authors' network thus seems to have included only gas-phase, destructive mechanisms for propanol. More recently, Manigand et al. (2021) included a generic form of propanol in their gas-grain network that did not differentiate between the *normal* and *iso* forms. Here we present the first model to incorporate a full gas-phase and dust-grain chemistry with active formation and destruction routes for both forms of propanol.

The new network is informed by that constructed for *normal*- and *iso*-propyl cyanide by Belloche et al. (2014) and refined and extended by Garrod et al. (2017) to include the butyl cyanides and the pentanes. The new network also incorporates several new ethanol-related reactions introduced into the network by Jin et al. (in prep.), which mainly concern the hydrogenation state of the C-C-O molecular backbone on grain surfaces.

Construction of the network follows the general approach laid out by Garrod et al. (2008) and followed in later publications; *normal*- and *iso*-propanol are assumed to form on dust grains, primarily through the barrierless addition of radicals on the grain/ice surfaces or within the bulk ice. The chemistry of most of the relevant radicals was already present in earlier networks, but several additional radicals have been included along with the two forms of propanol, and these also have a full complement of their own gas-phase and dust-grain chemical processes. The network differentiates between structurally isomeric radicals, in which the radical site may be present on different atoms, e.g., the primary radical  $\dot{\text{C}}\text{H}_2\text{CH}_2\text{OH}$ , versus the sec-



ondary radical  $\dot{\text{C}}\text{H}_3\dot{\text{C}}\text{HOH}$ ; the addition of a methyl ( $\text{CH}_3$ ) radical to each of these would lead to  $n\text{-C}_3\text{H}_7\text{OH}$  and  $i\text{-C}_3\text{H}_7\text{OH}$ , respectively. The addition of OH to the isomeric radicals of formula  $\text{C}_3\text{H}_7$  may similarly produce one or other of the propanol structures. A unique mechanism for  $n$ -propanol is also provided by the addition of the radicals  $\text{C}_2\text{H}_5$  and  $\text{CH}_2\text{OH}$ .

The radicals involved in this chemistry may be produced by atomic addition to smaller molecules, such as by the hydrogenation of vinyl alcohol,  $\text{C}_2\text{H}_3\text{OH}$ , by atomic H on grain surfaces, leading to  $\dot{\text{C}}\text{H}_2\text{CH}_2\text{OH}$  and  $\text{CH}_3\dot{\text{C}}\text{HOH}$ . Stable molecules may also be photodissociated by external UV photons or by the cosmic ray-induced UV field to produce these and other radicals. All the new chemical species are provided photodissociation mechanisms from both UV sources, with the products assumed to be radical-radical or radical-atom pairs.

Abstraction of a hydrogen atom from a stable molecule by a reactive radical (producing another radical) is also possible, although these reactions typically have activation energy barriers. As a result, the most effective examples are those in which the barriers are low (e.g., involving attack by the OH radical or an H atom). Due to the low temperatures involved for much of the grain-surface and ice chemistry, H-abstraction reactions are assumed typically to be driven by the quantum tunneling of the abstracted H atom. A rectangular barrier treatment is adopted in such cases, as per past models. Based on the substantial differences in activation energy barrier measured or calculated for these processes, the secondary radicals tend to be favored over primary radicals, due to the lower energies of their structures.

Several other reactions are included that involve the addition of an OH radical to a hydrocarbon. Of particular relevance to propanol formation is the reaction between OH and propylene,  $\text{C}_3\text{H}_6$ . Evidence from the literature indicates that these reactions are essentially barrierless in the gas phase (Atkinson et al. 1997; Thomsen & Jorgensen 2009), while both experimental and theoretical analyses indicate that the addition of OH to the terminal carbon occurs at a slightly higher rate than to the central carbon atom (Izsak et al. 2009; Daranlot et al. 2010; Loison et al. 2010), in ratios ranging from 58:42 to 72:28. In our network, we assume a ratio 3:2 (see Sec. 4.2) in the production of  $\text{CH}_3\dot{\text{C}}\text{HCH}_2\text{OH}$  versus  $\dot{\text{C}}\text{H}_2\text{CH}(\text{OH})\text{CH}_3$ , which are the precursor radicals of *normal* and *iso*-propanol, respectively.

Similar mechanisms were studied by Gannon et al. (2007) for the gas-phase addition of the CN radical to propylene, who found them to have null or minimal activation energy barriers. These latter were included by Garrod et al. (2017) as grain-surface processes. In that network we assumed that the product of the grain-surface reaction would be the lowest-energy radical (rather than two products, as would be expected in the gas-phase low-density limit). Here we assume the same product ratios as with the equivalent OH reaction above. In both the CN and OH reactions, routes for the abstraction of H, to produce HCN or  $\text{H}_2\text{O}$  and the  $\text{C}_3\text{H}_5$  radical, are also included.

Finally, following the approach of Garrod et al. (2022), we include surface and bulk-ice reactions between the ground-state diradical  $\text{CH}_2$  (methylene) and the stable molecules  $\text{C}_2\text{H}_5\text{OH}$  and  $\text{C}_2\text{H}_5\text{CN}$ . Although these reactions are assumed to have activation energy barriers, they will result in two radical products which are assumed to recombine to produce a larger molecule with 50% efficiency. In this way, the  $\text{CH}_2$  radical may insert itself in a two-step process (H-abstraction followed by  $\text{CH}_3$  radical addition) into ethanol or ethyl cyanide to produce either the *normal* or *iso* form of propanol or propyl cyanide. There are no measured data apparent in the literature for these particular reactions,

although gas-phase data exist for the analogous  $\text{CH}_2 + \text{C}_3\text{H}_8$  reactions (leading to radicals). The gas-phase activation energy barriers are not very well defined for these reactions either, but they seem to indicate that production of the primary  $\text{C}_3\text{H}_7$  radical would be favored (Tsang 1988), which for the ethanol-related reactions would lead to the preferential production of *n*-propanol.

Tables C.1 and C.2 provide details of most of the new, existing, or updated grain-surface/bulk-ice reactions in the network related to propanol and (in a few cases) to propyl cyanide. Table C.1 contains mostly radical-radical or atom-radical addition reactions. Table C.2 shows H-abstraction reactions related to H and OH attack; similar abstraction reactions were also included in the network for radicals such as  $\text{NH}_2$ , in keeping with the construction of past networks, but they have a relatively small effect on the results in the present case. All grain-surface and bulk-ice reactions in the network are equally available for all diffusive and non-diffusive reaction mechanisms.

Binding energies and enthalpies of formation used in the model for several existing or new chemical species are shown in Table C.3. Binding energies, where not directly measured, are interpolated from known values, following past publications. The assumed binding energy of water (on amorphous water ice) is the value adopted by Jin et al. (in prep.), which is lower than the one employed by Garrod et al. (2022). Binding energies are used to define the thermal and non-thermal desorption rates of these molecules from the grains. For chemical desorption, whose rate calculations require the enthalpies of formation, an efficiency factor (Garrod et al. 2007) of  $a = 0.001$  is assumed, to ensure that methanol is not overproduced in the gas phase at low temperatures.

Finally, a selection of (primarily) destruction reactions were included for all new species, encompassing photodissociation via external and CR-induced UV radiation, and ion-molecule reactions with  $\text{C}^+$ ,  $\text{H}^+$ ,  $\text{He}^+$ ,  $\text{H}_3^+$ ,  $\text{H}_3\text{O}^+$ , and  $\text{HCO}^+$  ions. For reactions with  $\text{C}^+$ ,  $\text{H}^+$ , or  $\text{He}^+$ , immediate fragmentation of the neutral molecule ensues. For  $\text{H}_3^+$ ,  $\text{H}_3\text{O}^+$ , and  $\text{HCO}^+$ , reaction leads to proton transfer, producing protonated forms of the neutrals involved. Electronic recombination reactions for these ions were also included, with a default fraction of 5% of these leading back to the original neutral, while the other branches involve the breakdown of the molecule's heavy-atom backbone. Following Taquet et al. (2016), and as also implemented by Garrod et al. (2022), we include proton transfer reactions between the protonated molecules and ammonia ( $\text{NH}_3$ ) assuming 100% efficiency, for molecules whose proton affinity is less than that of ammonia. This tends to enhance the ability of the neutrals to survive in the gas phase. Further details of the construction process for the gas-phase network are provided by Garrod et al. (2008), Garrod (2013), and others.

#### 4.2. Treatment of orientation-specific reactions on dust grains

Most of the new barrier-mediated reactions occurring on the grains, as well as some barrierless reactions, make use of the new  $F_{\text{dir}}$  and  $F_{\text{comp}}$  parameters introduced by Garrod et al. (2022), as these reactions are important in differentiating the two forms of propanol and of propyl cyanide produced in the models. The cyanide-related reactions that were already present in the network have been updated to include this parameterization in a consistent way. Only a selection of new reactions (i.e. those most relevant to propanol and propyl cyanide) have yet been set up to use this method, which will be developed comprehensively in future work.

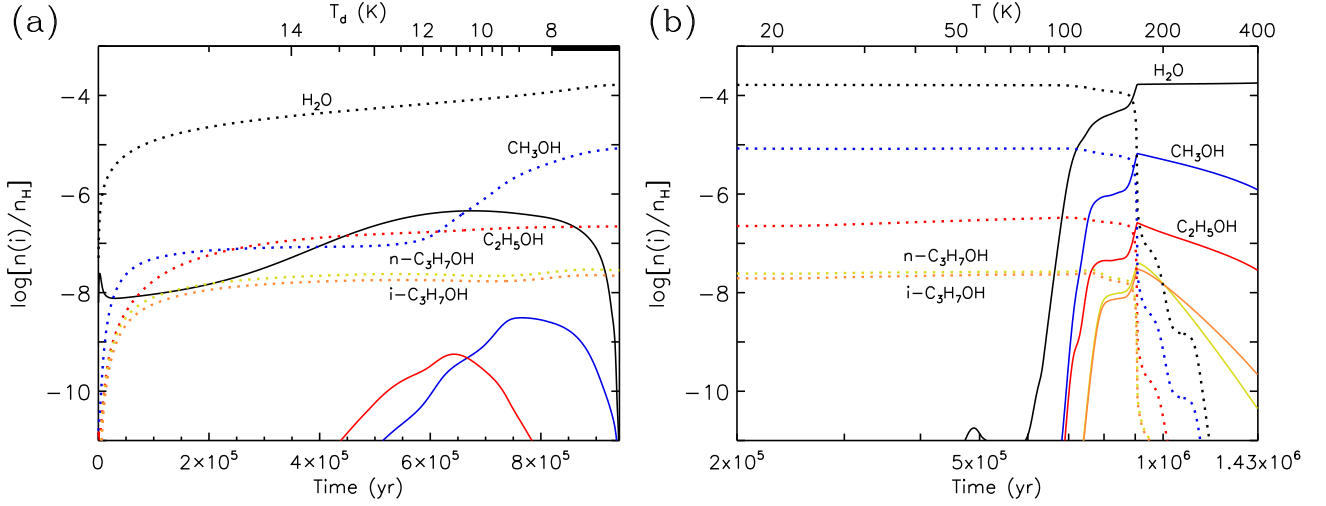


**Fig. 6.** Abundances with respect to total H for selected OH-group bearing molecules during the collapse stage and subsequent warm-up using the *slow* warm-up model. Solid lines indicate gas-phase species; dotted lines of the same colours indicate the same species on the dust grains. **Panel (a):** Stage 1 (collapse) model results, plotted linearly against time. The dust temperature is shown on the top axis, with an initial value of  $\sim 14.7$  K, which falls to a minimum of 8 K, while the gas temperature is held at 10 K throughout the collapse model. **Panel (b):** Stage 2 (warm up) model results, plotted logarithmically against time. Time values correspond to the time during the warm-up stage, which are plotted beginning  $2 \times 10^5$  yr into the warm up. The top axis shows the gas and dust temperatures, which are identical at this point in the model.

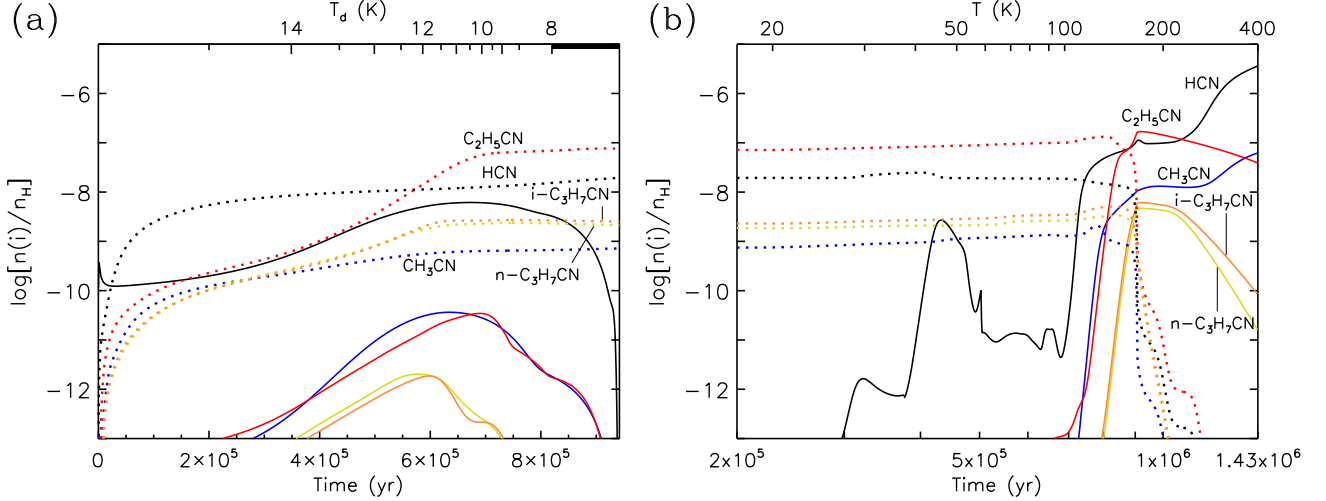


**Fig. 7.** Abundances with respect to total H for selected CN-group bearing molecules during the collapse stage and subsequent warm-up using the *slow* warm-up model. Other details as per Fig. 6.

The  $F_{\text{dir}}$  and  $F_{\text{comp}}$  parameters allow account to be taken of the directionality of surface and bulk-ice reactions, and of the competition between barrier-mediated reactions that involve different reactants.  $F_{\text{dir}}$  describes the fraction of orientation space of the two reactants from which a particular reaction is accessible. For example, a particular H atom in a large molecule may be susceptible to abstraction only with a particular orientation of the attacking radical with respect to the molecule. In this way, steric effects related to the specific structure of individual molecules may be considered.

All reaction types may in principle be assigned an  $F_{\text{dir}}$  value in the model, but the  $F_{\text{comp}}$  parameter is needed only for reactant-reactant pairings that have multiple barrier-mediated reactions available, for which the competition between these reactions must be controlled. For example, abstraction of different H atoms from the same molecule may be possible, depending on the orientation of the arriving radical with respect to the molecule (as defined by  $F_{\text{dir}}$ ), while each abstraction process

may have a different barrier. However, under certain orientations multiple abstraction processes may be accessible at once, and would therefore be competitive. A value of  $F_{\text{comp}} = 1$  for a particular abstraction reaction would indicate that for all  $F_{\text{dir}}$  values in which that reaction is accessible, it is competing with all other barrier-mediated processes according to their thermal or tunneling rates. A value of  $F_{\text{comp}} = 0$  would indicate that no other reaction outcomes are accessible at orientations accessible to the reaction of interest.

A more detailed description of the implementation of these parameters is provided by Garrod et al. (2022). Here, we have chosen a statistical distribution of reaction accessibility, in the absence of other information. That is, the three H atoms on the primary carbon of the ethanol molecule and the two H atoms on the secondary carbon of the same molecule are accessible for abstraction in a ratio of 3:2. For propane, which has six H atoms on the primary carbons, this ratio is 6:2; this is implemented in the model by adopting  $F_{\text{dir}}$  values of 0.75 and 0.25 for reactions

52/53 and 54/55. In the case of abstraction of secondary-carbon H atoms, as well as these reactions having lower accessibility ( $F_{\text{dir}}$ ) they are also much more likely to be in direct competition with abstraction from the primary carbon, due to crowding.  $F_{\text{comp}} = 1$  is therefore chosen for attack on the secondary-carbon H atoms, while  $F_{\text{comp}} = 0.25$  is chosen for the primary-carbon H atoms. In fact, due to the lower barriers to attack on the secondary-carbon H atoms, this route will nevertheless tend to win the competition in the fraction of cases ( $F_{\text{dir}}$ ) in which it is accessible.

As noted by Garrod et al. (2022), the  $F_{\text{dir}}$  values for any particular collection of reaction outcomes do not need to sum to unity, but we indeed choose this to be the case for the generic parameters that we apply to all relevant alcohol- or nitrile-related reactions in the new network. For molecules with three functional groups, such as  $\text{C}_2\text{H}_5\text{OH}$ ,  $\text{C}_2\text{H}_5\text{CN}$ , or  $\text{C}_3\text{H}_8$ , the central  $\text{CH}_2$  group is assumed to be accessible to attack in 25% of cases ( $F_{\text{dir}} = 0.25$ ), based on the statistical fraction of H atoms on the central carbon out of the total of 8 present in propane. Hydrogen atoms on a terminal carbon are assumed to be accessible in 37.5% of cases ( $F_{\text{dir}} = 0.375$ ). Then, regardless of the reaction or functional group, the other end of the molecule is also assumed to be accessible in 37.5% of cases. The latter includes the abstraction of H from the hydroxyl group in ethanol (reactions 58 and 61). Since H-abstraction cannot occur from the CN group in ethyl cyanide, in 37.5% of cases the meeting of H or OH with  $\text{C}_2\text{H}_5\text{CN}$  will lead to no reaction accessibility at all.

These same  $F_{\text{dir}}$  values are applied also to the addition reactions of OH and CN to propylene. As noted in Sect. 4.1, experimental and theoretical determinations of the ratios of radical production are available in the case of  $\text{OH} + \text{C}_3\text{H}_6$  (reactions 49 and 50). While the generic statistical values we adopt here for all similar reactions represent crude assumptions ( $F_{\text{dir}} = 0.375$  for radical addition to a terminal carbon and  $F_{\text{dir}} = 0.25$  to a central carbon), the resulting 3:2 ratio lies close to the experimental and theoretical values.

For molecules with four functional groups, such as *n*- $\text{C}_3\text{H}_7\text{OH}$  and *i*- $\text{C}_3\text{H}_7\text{OH}$ , a similar statistical treatment is applied, using  $\text{C}_4\text{H}_{10}$  as the model, i.e. attack on terminal functional groups has  $F_{\text{dir}} = 0.3$  (3/10), while the inner functional groups split the remainder. This means that the hydrogen atom on the central carbon in *i*- $\text{C}_3\text{H}_7\text{OH}$  has an accessibility of only 10%.

Separate from  $F_{\text{dir}}$  values, which determine the fraction of reactant meetings from which a particular reaction is accessible (constituting a pre-reaction efficiency factor applied to the meeting rate), branching ratios may be used to decide on the outcome of otherwise identical meeting and reaction conditions (i.e. post-reaction splitting of the reaction rate). Branching ratios always sum to unity. Here they are applied to several barrierless radical-radical reactions, in cases where H-atom transfer is in competition with addition. The two branches may be considered accessible from the same orientations.

#### 4.3. Chemical modelling results

Figure 6 shows the stage 1 (collapse) and stage 2 (warm up) chemical abundances of methanol, ethanol, *n*-propanol, *i*-propanol, and water, with respect to total hydrogen. Solid lines in each correspond to gas-phase molecules, with dotted lines of the same colours indicating the grain-surface forms of the same species. The stage 1 results (panel a) are plotted linearly with time. It can be seen that methanol production on grains begins early on in the model, but only reaches a value close to its peak

abundance in the ice much later on. Ethanol also begins to be formed quite early on, but quickly reaches a level close to its maximum on the grain surfaces. Similar behavior is seen for both forms of propanol, although there is a slight increase toward the end of stage 1.

Methanol is mainly produced by repetitive H-atom addition to CO on the grains, as per past models. Ethanol is initially produced mainly within the bulk ice mantle, through PDI reactions (i.e. non-diffusive reactions driven by photodissociation) between  $\text{C}_2\text{H}_5$  and OH (listed as reaction 5 in Table C.1). The photodissociation is the result of external UV radiation penetrating the initial 3 magnitudes of extinction. Similar reactions drive vinyl alcohol ( $\text{C}_2\text{H}_3\text{OH}$ ) production, and the hydrogenation of vinyl alcohol in the bulk ice by mobile H atoms soon takes over as the main ethanol formation mechanism (reactions 1, 2, 10, and 12). Once  $A_V$  exceeds around 5 mag, the external UV field only has weak effect, and the production of solid-phase ethanol is dominated by surface reactions such as methylene addition to methanol (reaction 4) and hydrogenation of ketene ( $\text{CH}_2\text{CO}$ ) and acetaldehyde ( $\text{CH}_3\text{CHO}$ ). Once formed on the grain/ice surface, that ethanol is incorporated into the bulk ice as the mantle grows.

Production of *normal*- and *iso*-propanol begins within the bulk ice similarly to ethanol, driven by the PDI reaction of OH with propylene ( $\text{C}_3\text{H}_6$ ) (reactions 49 and 50), followed by hydrogenation of the resultant radical by mobile H (reactions 24 and 33). Being barrierless, these OH reactions lead to a preference (3:2) for *n*- $\text{C}_3\text{H}_7\text{OH}$  production, based on their  $F_{\text{dir}}$  values. However, a modest amount of propanol is also formed by PDI reactions of OH with either the primary or secondary radical forms of  $\text{C}_3\text{H}_7$  (reactions 20 and 29), which are themselves formed by diffusive reactions of atomic H with propylene. These reactions (46 and 47) have activation energy barriers that strongly favor the secondary radical; combined with the  $F_{\text{dir}}$  values that favor the primary radical, this leads to approximately equal production of the two. As a result, at these early times, propanol formation only slightly favors the *normal* form, in a ratio somewhat less than 3:2.

The later rise in solid-phase propanol abundances during stage 1 occurs when the gas density becomes high and dust temperatures fall; production on the surface of the ice takes over (followed by incorporation into the mantle). Again, OH reactions with propylene dominate.

During stage 2 (panel b – *slow* model results are shown), the abundances of *n*- and *i*-propanol are mostly flat until a temperature of around 100 K is reached; OH reactions with propylene and OH addition to  $\text{C}_3\text{H}_7$  radicals driven by photodissociation (PDI) enhance propanol abundances a little during this period.

As water ice begins to leave the grains via thermal desorption, unreacted propanol-precursor radicals (i.e. various structures of formula  $\text{C}_3\text{H}_7\text{O}$ ) trapped in the ice are released onto the grain surface, where they may be more easily hydrogenated, boosting the production of both *n*- $\text{C}_3\text{H}_7\text{OH}$  and *i*- $\text{C}_3\text{H}_7\text{OH}$ . The reaction of OH with propylene, driven mainly by the PDI mechanism, also continues to produce such radicals in the ice right up until the complete loss of the ice mantles.

Propanol molecules reach their peak abundances in the gas phase immediately following their complete release from the grains. *n*- $\text{C}_3\text{H}_7\text{OH}$  initially dominates over *i*- $\text{C}_3\text{H}_7\text{OH}$ , in the ratio preserved from the solid phase:  $\sim 1.6$ . Table 4 shows the peak abundances achieved in each of the stage 2 warm-up models, along with the corresponding model temperatures at which each peak value occurs. Following their abundance peaks, the *n*:*i* propanol ratio falls rapidly; however, this is caused by the slightly greater total CR-induced UV destruction rates for the

**Table 4.** Peak gas-phase abundances of selected molecules obtained with the three warm-up timescale models. Abundances are shown as a fraction with respect to  $H_2$  at the moment when the molecule reaches its own peak abundance. The temperature of the dust and gas corresponding to the peak abundance value is also shown.

Molecule	Fast		Medium		Slow	
	$n[i]/n[H_2]$	$T$ (K)	$n[i]/n[H_2]$	$T$ (K)	$n[i]/n[H_2]$	$T$ (K)
$CH_3OH$	1.88(-5)	168	1.73(-5)	167	1.33(-5)	166
$C_2H_5OH$	5.33(-7)	241	4.89(-7)	167	5.12(-7)	166
$n-C_3H_7OH$	7.12(-8)	212	7.29(-8)	168	7.90(-8)	167
$i-C_3H_7OH$	5.78(-8)	219	6.03(-8)	169	5.92(-8)	167
$CH_3CN$	3.42(-9)	400	1.27(-8)	398	1.23(-7)	400
$C_2H_5CN$	1.96(-7)	170	2.33(-7)	167	3.38(-7)	171
$n-C_3H_7CN$	9.25(-9)	180	9.25(-9)	184	9.35(-9)	171
$i-C_3H_7CN$	1.10(-8)	180	1.18(-8)	181	1.23(-8)	171

**Notes.**  $x(y)$  means  $x \times 10^y$ .

**Table 5.** Ratios of branched-chain molecules with their straight-chain forms, for each model, as well as ratios between larger and smaller homologues; data correspond to the ratios of the peak values given in Table 4. Observed ratios are also shown.

Molecular ratio	[Fast]	[Medium]	Slow	Observations
$CH_3OH / C_2H_5OH$	35.3	35.4	25.4	19
$CH_3OH / n-C_3H_7OH$	264	237	168	350
$CH_3OH / i-C_3H_7OH$	325	287	224	630
$C_2H_5OH / n-C_3H_7OH$	7.48	6.71	6.60	18
$C_2H_5OH / i-C_3H_7OH$	9.22	8.11	8.80	33
$n-C_3H_7OH / i-C_3H_7OH$	1.23	1.21	1.33	1.8
$C_2H_5CN / CH_3CN$	57.3	18.3	2.74	2.8 <sup>a</sup>
$C_2H_5CN / n-C_3H_7CN$	21.2	25.2	36.1	34 <sup>a,b</sup>
$n-C_3H_7CN / i-C_3H_7CN$	0.842	0.785	0.762	2.5 <sup>b</sup>

**Notes.** Observational values are those presented in this work, with the exception of <sup>a</sup> Belloche et al. (2016), <sup>b</sup> Belloche et al. (2014).

*normal* form. Since all of these rates are simply estimates, the post-peak drop in  $n:i$  is not a reliable feature of the models.

Figure 7 shows the behavior of chemical abundances of various nitriles, including *normal*- and *iso*-propyl cyanide. Like propanol, the propyl cyanides also form on the grains at early times; however, in this case, the production is driven initially by surface reactions. H-abstraction from surface  $C_2H_5CN$  preferentially produces the secondary radical (reaction 63), due to the lower activation energy barrier of this reaction, in spite of its smaller  $F_{dir}$  value. Production of *iso*-propyl cyanide is therefore marginally higher than that of the *normal* form.

In contrast to the results of Garrod et al. (2017), the reaction of CN with propylene is not an effective mechanism for propyl cyanide formation in the present models. The removal of bulk diffusion for heavy species (i.e. CN) means that this reaction does not occur rapidly within the ice, even at elevated temperatures, while on the ice surfaces the production rate of the CN radical is not great enough to make this pathway significant.

At times around  $5 \times 10^5$  yr into the collapse model, methylene ( $CH_2$ ) insertion into ethyl cyanide allows *n*- and *i*- $C_3H_7CN$  to grow, with the *normal* form becoming slightly dominant in its abundance. This behavior is then reversed toward the end of the stage 1 model, as H-abstraction from  $C_2H_5CN$ , followed by methyl-group addition, takes over as the main propyl cyanide-forming mechanism on the ice surfaces, which substantially favors the production of the  $CH_3\dot{C}HCN$  radical, thus bumping up

the *i*- $C_3H_7CN$  isomer sufficiently to become slightly more abundant than the *n* form in the ice mantles.

During the warm-up of the core (panel b), the  $n:i$  ratio of propyl cyanide formed earlier on is largely preserved, leading to a gas-phase ratio that is close to unity. Note that, in the present model, the gas-phase destruction of propyl cyanide is slower than in the Garrod et al. (2017) models, due to proton transfer of protonated propyl cyanide to ammonia, which slows the destructive effects of dissociative electronic recombination.

Table 5 shows the ratios of the various alcohols and nitriles obtained from the models and observations; for the nitriles, the observational values derive from Belloche et al. (2014) and Belloche et al. (2016). All of the model ratios correspond to the quotient of the peak values given in Table 4. Modeled ratios of methanol with the two forms of propanol are broadly in agreement with the observations, i.e. within a factor of around 2–3 in each case, when comparing the *slow* model results, which were generally found by Garrod et al. (2022) to provide the best match to Sgr B2(N) data. Ethanol itself is slightly underproduced with respect to methanol, by a factor  $\sim 1.3$ , which raises the disagreement in its ratios with *normal*- and *iso*-propanol to a factor of something closer to 3–4. The modeled  $n:i$  ratio for propanol is exceedingly close to the observed value. Although the models generally produce a very good match to the observational ratios of the nitriles, the  $n:i$  ratio for propyl cyanide is close to unity, rather than the observed value of 2.5. The results of the models are discussed further in Sect. 5.3.

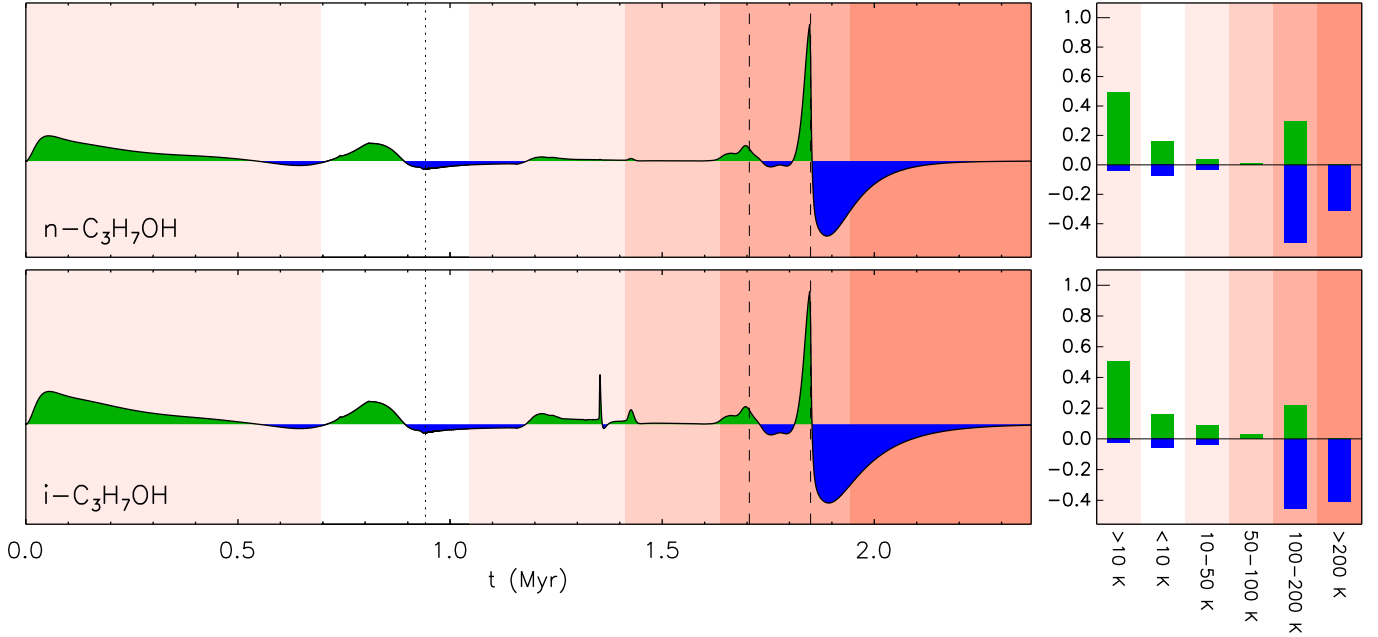


**Fig. 8.** *Left panels:* Net rate of change (arbitrary units) in the abundances of *normal*- and *iso*-propanol, summed over all chemical phases, during stages 1 and 2. Data correspond to the *slow* warm-up timescale in stage 2; the vertical dotted line indicates the start of the warm-up phase. Net gain is shown in green, net loss in blue. Vertical dashed lines indicate the onset and end-point of water desorption. Background colors indicate the dust temperature regime; from left to right these are:  $>10$  K,  $<10$  K,  $10\text{--}50$  K,  $50\text{--}100$  K,  $100\text{--}200$  K,  $200\text{--}400$  K. The initial dust temperature is  $\sim 14.7$  K. *Right panels:* Net rates of change integrated over each temperature range. Positive (formation) and negative (destruction) rates are integrated independently; both are normalized to the total integrated formation rate.

## 5. Discussion

### 5.1. Comparison of Sgr B2(N2) results to other sources

In their article on the detection of *trans* ethyl methyl ether ( $t\text{-C}_2\text{H}_5\text{OCH}_3$ ), which is an isomer of propanol, toward Orion KL with ALMA and the IRAM 30 m telescope, Tercero et al. (2015) also reported on a search for the *Gauche-anti* conformer of *normal*-propanol. They obtained a lower limit on the abundance ratio of the vibrational ground state of ethanol to the vibrational ground state of *Ga-n*- $\text{C}_3\text{H}_7\text{OH}$  of 60. Accounting for vibrational and conformational corrections to the partition function at the temperature that they determined for this source (100 K), this nondetection translates into a lower limit on the abundance ratio of ethanol to *normal*-propanol of 14 (see Müller et al. 2016). This indicates that, if present in Orion KL, *normal*-propanol is not more abundant than in Sgr B2(N2b) with respect to ethanol. However, given that ethanol is  $\sim 30$  times less abundant than methanol in Orion KL (Kolesníková et al. 2014) while their ratio is only a factor 19 in Sgr B2(N2b) (Table 2), we can conclude that *normal*-propanol is, relative to methanol, more abundant in Sgr B2(N2b) than in Orion KL.

Nondetections of both *normal*- and *iso*-propanol were also reported toward the Class 0 protostar IRAS 16293-2422B on the basis of the Protostellar Interferometric Line Survey (PILS) performed with ALMA (Manigand et al. 2021). A similar column density upper limit was obtained for both isomers ( $3 \times 10^{15} \text{ cm}^{-2}$ ). Considering the column densities of methanol and ethanol derived with the PILS survey toward the same source by Jørgensen et al. (2018) ( $1 \times 10^{19}$  and  $2.3 \times 10^{17} \text{ cm}^{-2}$ , respectively), the upper limits obtained by Manigand et al. (2021) imply that both isomers of propanol are at least 3300 and 80 times less abundant than methanol and ethanol in this source, respectively. This means that propanol is, relative to methanol, at least one order of magnitude less abundant in IRAS 16293-2422B

than in Sgr B2(N2b). Manigand et al. (2021) applied conformation corrections to the partition function in order to derive their column density upper limits, but they do not mention any vibrational correction. At the temperature they considered (100 K), this correction factor is smaller than 1.5 and would not significantly reduce the large difference between the two sources. This difference for propanol is surprising given the strong correlation that was noticed between the chemical composition of IRAS 16293-2422B and Sgr B2(N2) for oxygen-bearing species (Jørgensen et al. 2020). The correlation between the two sources may break down beyond a certain degree of chemical complexity.

### 5.2. Observed isomeric ratios of propanol and propyl cyanide

It is striking that the isomeric ratio  $[\textit{iso}]/[\textit{normal}]$  that we obtained in Sgr B2(N2) is similar for both propanol and propyl cyanide (0.6 versus 0.4). Besides, the abundance ratios of ethanol to *normal*-propanol and of ethyl cyanide to *normal*-propyl cyanide are similar within a factor of  $\sim 2$  (15 versus 34). This probably indicates similarities in the chemical processes that form these two families of molecules, as we discuss further in the next section.

### 5.3. Discussion of chemical model results

Although the introduction of non-diffusive grain-surface and bulk-ice reaction mechanisms into the model has changed some of the general behavior, the suggestion by Garrod et al. (2017) that OH addition to propylene would be an important mechanism for propanol production is borne out here – it appears to be dominant throughout the chemical evolution. Furthermore, their prediction that this mechanism would lead to an *i:n* ratio “around unity or a little less” also stands up well.

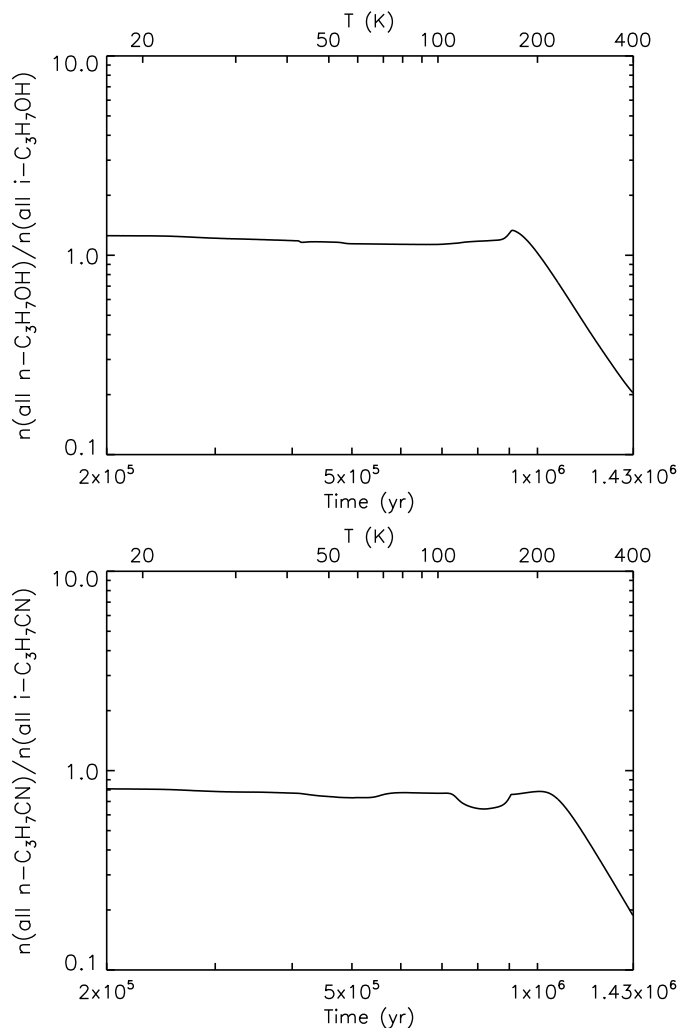


**Fig. 9.** Ratios of *normal*- to *iso*-propanol (upper panel) and *normal*- to *iso*-propyl cyanide (lower panel), summed over all phases, during the warm-up (stage 2) model.

In comparing the modeled abundance ratios with the observations, we note that our comparison between the peak abundances of different molecules, as shown in Table 5, introduces a degree of error related to the relative desorption temperatures of those species and their survival timescales in the gas phase; the observed column densities may reflect spatial variation that the present models are not equipped to reproduce. However, we would expect these considerations to be much less important when comparing the two forms of propanol, whose desorption properties should be much more similar than between the different homologs (e.g., methanol or ethanol). The behavior of the cyanides should be affected in a similar way. Thus, the *n:i* ratios for propanol and propyl cyanide might be considered the most robust aspect of the model results when comparing with observations.

In fact, the models come remarkably close to the observed abundance ratios of all the molecules considered, including the *n:i* ratios of both propanol and propyl cyanide. Furthermore, while the ratios between different molecules are somewhat variable for different model warm-up timescales, the *n:i* ratios are fairly stable, especially for propanol. Part of this stability may be due to the fact that, in general, the dominant production mechanisms for the *iso* or *normal* forms of either propanol or propyl cyanide tend to be the same throughout; the reaction of OH

with propylene is responsible for forming much of the *n*- and *i*-C<sub>3</sub>H<sub>7</sub>OH, while the abstraction of H from ethyl cyanide, followed by addition of methyl to the resulting radical is responsible for most *n*- and *i*-C<sub>3</sub>H<sub>7</sub>CN production.

Much of the formation of propanol and propyl cyanide occurs during the cold stages of the hot core evolution; Figure 8 shows the net rates of formation of *n*-C<sub>3</sub>H<sub>7</sub>OH and *i*-C<sub>3</sub>H<sub>7</sub>OH, summed over all phases (gas, surface, and bulk), from the start of the stage 1 model to the end of stage 2. In the right-hand panels are shown the totals of the net formation rates occurring during several different temperature regimes experienced by the hot core (the sum of net positive rates is shown in green, the sum of net negative rates is shown in blue – see Garrod et al. 2022, for further explanation of this style of plot). Nearly half of all propanol is formed while the visual extinction is quite low and the dust temperatures are still greater than 10 K, through photodissociation-induced reactions within the young ice mantles caused by the external UV field. As noted in Sect. 4.3, a modest contribution of reactions between OH and the two C<sub>3</sub>H<sub>7</sub> radicals in the bulk ice lessens the dominance of the *normal* form at this point in the models.

Later in the models, during the period in which the desorption of the ice mantles becomes significant (indicated in Fig. 8 by the two dashed vertical lines), the OH + C<sub>3</sub>H<sub>6</sub> reactions are more dominant. Also, at these higher temperatures, the barrier against the reaction of H with C<sub>3</sub>H<sub>6</sub> to produce the primary form of the C<sub>3</sub>H<sub>7</sub> radical is less important, so that even the OH + C<sub>3</sub>H<sub>7</sub> mechanism tends to favor production of *n*-propanol more strongly. Figure 9 indeed shows the *n:i* ratio during the stage 2 evolution, where it may be seen that the ratio reaches its peak at the moment of maximum desorption from the grains. It may be considered, then, that if, during the cold collapse stage, the core were to spend less time at low visual extinctions or began forming ice mantles at a somewhat higher extinction, then while the overall production of propanol would be less, its production would be dominated more by the high-temperature, late-stage mechanisms that favor a higher *n:i* ratio.

In the present models, the ultimate reason for the *n:i* ratio in propanol being a little greater than unity seems to originate in the choice of  $F_{\text{dir}}$  values for certain key reactions, in particular the reactions of OH with propylene. Here, production ratios of 3:2 are chosen for radicals related to the *n* and *i* forms of propanol, respectively, and this ratio is approximately preserved in propanol abundances throughout the model run. Theoretical modeling on the outcomes of these reactions in the gas phase (under the high-pressure limit, which is appropriate for the solid-phase conditions of interest here), based on transition state theory analysis, indeed indicate ratios similar to these: Daranlot et al. (2010) find 58:42, while Izsak et al. (2009) find that 65.8% leads to terminal carbon addition, i.e. close to 2:1. The experimental work of Loison et al. (2010) yields a ratio of 72:28. The 3:2 ratio used in our grain-chemistry network is therefore a little conservative, but still within the bounds provided by detailed studies of this system.

The slightly low *n:i* propanol ratio provided by our models, as compared with the observations, may therefore be explained as an underestimate of the chemical-reaction ratio applied in our network. It is interesting to consider that the observed *n:i* ratio of propanol may be a direct reflection of the underlying branching ratio of the OH + C<sub>3</sub>H<sub>6</sub> reaction.

Although the modelled abundances of propyl cyanide are close to the observed values, the deviation in the *n:i* ratio in this case appears a little more stark. The models do not allow for a substantial degree of production of propyl cyanide through



CN radical addition to propylene in the same way as propanol is formed. Although this mechanism is not hindered in any way, it relies on the photodissociation of HCN in the ice to produce CN, in the same way as the analogous propanol-forming reaction relies on the photodissociation of water. As may be seen from Figures 6 and 7, the solid-phase abundance of HCN is around four orders of magnitude lower than that of water. As a result, the reaction of CN with propylene is simply not rapid enough to contend with the competing mechanism relating to H-abstraction from ethyl cyanide on the surface of the ice. Unlike the OH and CN addition processes, this reaction does have barriers that are substantial enough to favor strongly the production of the secondary radical at early times, which leads to the formation of *i*-C<sub>3</sub>H<sub>7</sub>CN upon the addition of a methyl radical. However, the greater accessibility (i.e. greater  $F_{\text{dir}}$  value) of the process that leads to the primary radical tends to balance out the effects of its higher barrier, especially when the dust temperatures are close to their minimum, which reduces the possibility that the H atom attacking ethyl cyanide will diffuse away before the reaction can occur. This effect is more pronounced in the bulk ice, where atomic H has a higher barrier to diffusion than on the ice surface.

Ultimately, it is the steric effects involved in the attack of H on C<sub>2</sub>H<sub>5</sub>CN on the grains (reactions 62 and 63), which are reproduced by the adoption of the  $F_{\text{dir}}$  and  $F_{\text{comp}}$  parameters in the models, that determine the maximum allowed *n*:*i* ratio for propyl cyanide (here, 3:2). Under conditions where H atoms have low mobility, reaction will commonly occur in spite of the activation energy barriers, and thus  $F_{\text{dir}}$  will determine the ratio of primary to secondary radicals produced. However, the temperature threshold at which the barriers become unimportant will indeed be a function of those very activation energy values, and these are poorly constrained in the literature; our models use only estimates based on analogous (gas phase) reactions involving propane. If the activation energy for abstraction of H from the secondary carbon in propyl cyanide were nearer to the value for the attack on the primary carbon, then the *n*:*i* ratio produced by the models would be closer to our chosen statistical limit of 3:2, although this value itself is insufficient to reproduce the observed ratio. Assuming that no other chemical mechanism is strongly contributing to propyl cyanide production, then this could indicate that abstraction of H from the secondary carbon of C<sub>2</sub>H<sub>5</sub>CN may be more sterically hindered than we assume here. Such an effect might be more prevalent when manifested on an ice surface or within the ice mantle, wherein any sort of roaming effect for the attacking H atom could be very limited due to the surrounding ice structure.

As noted above, the *n*:*i* ratios for propanol and propyl cyanide that we observe toward Sgr B2(N) are similar enough that one might suspect similar underlying chemical processes to be forming them. However, unless the chemical models vastly under-produce HCN, and thus CN, in the ices, it seems unlikely that propanol and propyl cyanide share *exactly* analogous formation mechanisms. Nevertheless, similar steric effects may be controlling the reactivity of their precursors in similar ways and to similar degrees. This would be the case if activation energies played only a small role, with the physical accessibility of either the primary or secondary carbon functional group being the main determinant of the outcome of a particular reaction. Such an effect may be more prevalent within and upon low-temperature ices, in which surrounding water molecules may physically inhibit access to particular reaction channels, while the attacking atom or radical may also be trapped or sufficiently immobile such that a reaction would become inevitable, even if an acti-

vation energy barrier should be present. In that case, the ratio of the probabilities of attack on a terminal versus central functional group of some arbitrary molecule should assume a value that would somewhat favor reaction at the terminal methyl group (potentially by a factor of say 2), due to the terminal carbon holding a larger number of H atoms and having greater accessibility from different orientations.

It is possible, then, that the similar *n*:*i* ratios of propanol and propyl cyanide are due to the reactions that form them both lying in this steric limit of reaction accessibility, caused by the reactions occurring in/upon ices. To determine the veracity of this supposition will require detailed chemical calculations in which the relevant reactions are simulated on an ice surface or in the presence of a surrounding ice matrix. Results determined from gas-phase measurements or calculations may not be sufficient to approximate such a slim divergence between the *iso* and *normal* forms of the molecules studied here.

It is valuable to compare our models with other recent treatments of propanol chemistry. The astrochemical models presented by Manigand et al. (2021) considered a generic form of propanol, using a network that incorporated the scheme proposed by Qasim et al. (2019) for the hydrogenation of grain-surface propenal (C<sub>2</sub>H<sub>3</sub>CHO) to propanal (C<sub>2</sub>H<sub>5</sub>CHO), and further to *normal*-propanol. They also included a reaction between atomic O and propane (C<sub>3</sub>H<sub>8</sub>), producing the radicals OH and C<sub>3</sub>H<sub>7</sub>, which could further recombine to form propanol. The latter process in particular was highlighted by Manigand et al. as being a productive route to propanol in their models. The propenal/propanal routes are not included in our own network, as we do not have propenal in the model, and its full inclusion would require a far more extended network. Nor does our model include the apparently more important reaction of atomic oxygen with propane; however, the activation energy barriers for this process are not well defined in the literature (because the fits to experimental gas-phase rates, conducted at room temperature and above, have a strong temperature dependence in the collisional portion). Our own Evans-Polanyi calculations for the H-abstraction process (based on the data provided by Dean & Bozzelli 1999) to form each of the two C<sub>3</sub>H<sub>7</sub> isomers suggests barriers that are rather higher than those employed by Manigand et al. (i.e. 2100–2800 K, vs. 1000 K for each branch), with the secondary radical energetically preferred, as is typical. Thus, this process should be somewhat less efficient than the OH reaction with propylene, all else being equal. Furthermore, the production rate of O in the ice mantles, either by photodissociation of OH or CO<sub>2</sub> or through reactive mechanisms, is substantially slower than that of OH, which occurs primarily through photodissociation of water. In our model, it therefore seems unlikely that this process would make a major contribution to *normal*-propanol production. If the propenal/propanal mechanism that was also considered by Manigand et al. were to become an important contributor to *normal*-propanol production, it is unclear how stable the *n*:*i* ratio might be among different astrophysical sources.

Unfortunately, it is difficult to compare directly our chemical models with those of Manigand et al. (2021), as the latter use a purely diffusive grain-surface/mantle chemistry, meaning that the production of COMs is strongly dependent on radical mobilities, which may only become significant at elevated temperatures. Our own models rely on non-diffusive processes to form many complex organic molecules on the grains (Garrod et al. 2022), which can occur at very low temperatures and early times.

#### 5.4. The crucial role of high angular resolution

Compared to its predecessor EMOCA, the higher angular resolution of the ReMoCA survey turned out to be crucial in bringing down the degree of spectral confusion that limits our ability to identify low-abundance COMs in the emission spectra of hot cores. The smaller beam of ReMoCA allowed us to resolve the molecular emission of Sgr B2(N2), the secondary hot core of Sgr B2(N), and thereby reveal regions of smaller velocity dispersion. It is striking to realize that the continuous gain in our sustained efforts over the past 15 years to decipher the molecular content of Sgr B2(N) has greatly benefitted from a substantial increase in angular resolution that came along with a decrease of the spectral line widths of this star forming region by a factor of 5. Both are required to beat the inevitable crowding of emission from various species near the confusion limit. This long-term project started with an angular resolution of  $\sim 30''$  using the IRAM 30 m telescope that traced lines with a FWHM of  $17 \text{ km s}^{-1}$  (Belloche et al. 2013), continued with ALMA at an angular resolution of  $1.6''$  that unveiled lines with a FWHM of  $5 \text{ km s}^{-1}$  (Belloche et al. 2016), and now culminates in revealing line widths of  $3.5 \text{ km s}^{-1}$  thanks to the  $0.6''$  angular resolution achieved with the ReMoCA survey, and even  $2 \text{ km s}^{-1}$  at the edge of the molecular emission detected around Sgr B2(N2).

While the gain in angular resolution was key in reducing the spectral confusion in the Sgr B2(N) region, the gain in sensitivity allowed by the higher number of antennas in ALMA's cycle 4 and the longer integration time awarded to the ReMoCA survey also played a crucial role in the detection of both isomers of propanol. The abundance ratios derived for the latter with respect to ethanol with the ReMoCA survey indicate that the EMOCA survey was short of a detection of propanol by a factor of  $\sim 2$  in sensitivity.

All of the numerous new detections of COMs reported in 2021–2022 (see the "Molecules in Space" webpage of the CDMS<sup>4</sup>) were obtained with single-dish telescopes, thanks to three surveys that achieved high sensitivities through huge amounts of observing time and large instantaneous bandwidths: the QUIJOTE survey of the dark cloud core TMC1 with the Yebes 40 m telescope (e.g., Cernicharo et al. 2021), the GOTHAM survey of TMC1 with the Green Bank Telescope (e.g., McGuire et al. 2021), and the survey of the molecular cloud G+0.693–0.027 in the vicinity of Sgr B2(N) with the Yebes 40 m and IRAM 30 m telescopes (e.g., Rodríguez-Almeida et al. 2021). Despite the obvious strength of these single-dish surveys, which profit from the large angular sizes of the emission regions, our detection of *iso*-propanol and *normal*-propanol shows that ALMA still has a role to play in the discovery of COMs, especially in star forming regions at the scales where protostellar systems emerge. However, strategies must be found to beat the confusion limit that is easily achieved in these hot and dense regions. Resolving low-velocity-dispersion regions at high angular resolution is one way, which we have explored here; going to lower frequencies with, e.g., band 2 of ALMA in the near future may also be promising.

Interestingly, the conformers of *normal*-propanol that contributed to its detection toward Sgr B2(N2b), the *Gauche-gauche*' and *Anti-gauche* conformers, are two of its higher-energy conformers (though the energy of all conformers is within tens of wavenumbers). This illustrates that it is difficult to predict which conformer of a given molecule should be the most favorable one to achieve a detection in the line-crowded spectrum of a hot core, in particular when the energy difference

is small with respect to the excitation (rotation) temperature, and even more so, if the dipole moment or one of its components is more favorable. The key factor turns out to be the degree of contamination of the spectral lines of that molecule from emission of other molecules. This suggests that spectroscopists should also characterize higher-energy conformers of the COMs investigated in their laboratories and not only focus on the lowest-energy ones.

## 6. Conclusions

The high angular resolution and sensitivity achieved with ALMA in the frame of the ReMoCA survey has led to the first interstellar detection of *iso*-propanol, and the first robust detection of its isomer, *normal*-propanol, in a hot core. These detections were obtained toward Sgr B2(N2b), a new position revealed by the ReMoCA survey and characterized by narrow line widths of  $3.5 \text{ km s}^{-1}$  in the secondary hot core of Sgr B2(N). The main conclusions of this work are the following:

1. Both conformers of *iso*-propanol and two of the higher-energy conformers of *normal*-propanol have contributed to the detections of these isomers toward Sgr B2(N2b). The transitions of the other three conformers of *normal*-propanol fall at frequencies that are more affected by blending with emission of other species. Therefore, the zero-point energy of a conformer of a given molecule does not prefigure its detectability in the congested spectra of hot cores.
2. *iso*-Propanol and *normal*-propanol are 600 and 350 times less abundant than methanol in Sgr B2(N2b), respectively. They are 30 and 20 times less abundant than ethanol, respectively.
3. The abundance of *iso*-propanol relative to *normal*-propanol is 0.6 toward Sgr B2(N2b), which is strikingly similar to the isomeric ratio of 0.4 obtained earlier for propyl cyanide toward Sgr B2(N2). This probably indicates similarities in the chemical processes that form these two families of molecules.
4. The chemical models indicate that propanol is mainly produced within the dust-grain ice mantles, via photodissociation-induced reactions between OH and propylene ( $\text{C}_3\text{H}_6$ ), although other mechanisms also make modest contributions. The observed *normal*-to-*iso* ratio is consistent with a direct preservation of the ratio of OH addition to the terminal versus central carbon atom in propylene.

With the detection of *iso*- and *normal*-propanol, two pairs of organic molecules with a functional group attached either to a primary or secondary carbon atom have now been detected in the interstellar medium, the second pair being *iso*- and *normal*-propyl cyanide,  $\text{C}_3\text{H}_7\text{CN}$  (Belloche et al. 2009, 2014). In the latter case, the carbon in the CN group technically makes *iso*-propyl cyanide a branched carbon-chain molecule, while *iso*-propanol is not branched by this definition. Nevertheless, in the placement of the -OH or -CN functional group, both pairs of molecules are directly comparable.

The similarity of the propanol and propyl cyanide *normal*-to-*iso* ratios is not fully accounted for by the models presented here, although a perfect match could likely be achieved with a small degree of tuning in certain poorly-defined parameters (such as activation energies against the abstraction of different H atoms from ethyl cyanide). Finding other such pairs of molecules may help in pinning down the processes that dominate in setting

<sup>4</sup> <https://cdms.astro.uni-koeln.de/classic/molecules>

these ratios in each family of molecules. The search for *normal*-butanal ( $\text{C}_4\text{H}_7\text{CHO}$ ) and its branched isomer, *iso*-butanal, toward Sgr B2(N) and G+0.693–0.027 has unfortunately not been successful so far (Sanz-Novo et al. 2022). A nondetection of lactaldehyde (2-hydroxypropanal),  $\text{CH}_3\text{CH}(\text{OH})\text{CHO}$ , was also reported toward several star forming regions (Alonso et al. 2019), but no investigation of its isomer, 3-hydroxypropanal ( $\text{HOCH}_2\text{CH}_2\text{CHO}$ ), which might be more abundant, has been reported to date. As mentioned in Sect. 1, our search for the straight-chain and branched forms of butyl cyanide,  $\text{C}_4\text{H}_9\text{CN}$ , in the ReMoCA survey has not been successful so far. In the alcohol family, the next candidate would be butanol ( $\text{C}_4\text{H}_9\text{OH}$ ) and its isomers, surely a challenging search given the difficult detection of propanol itself.

**Acknowledgements.** This paper makes use of the following ALMA data: ADS/JAO.ALMA#2016.1.00074.S. ALMA is a partnership of ESO (representing its member states), NSF (USA), and NINS (Japan), together with NRC (Canada), NSC and ASIAA (Taiwan), and KASI (Republic of Korea), in co-operation with the Republic of Chile. The Joint ALMA Observatory is operated by ESO, AUI/NRAO, and NAOJ. The interferometric data are available in the ALMA archive at <https://almascience.eso.org/aq/>. Part of this work has been carried out within the Collaborative Research Centre 956, sub-project B3, funded by the Deutsche Forschungsgemeinschaft (DFG) – project ID 184018867. RTG acknowledges support from the Astronomy & Astrophysics program of the National Science Foundation (grant No. AST 19-06489).

## References

- Alonso, E. R., McGuire, B. A., Kolesnikov, L., et al. 2019, *ApJ*, 883, 18
- Anderson, T., De Lucia, F., & Herbst, E. 1990, *ApJS*, 72, 797
- Atkinson, R., Baulch, D., Cox, R., et al. 2001, IUPAC Subcommittee on Gas Kinetic Data Evaluation for Atmospheric Chemistry; <http://www.iupac-kinetic.ch.cam.ac.uk>
- Atkinson, R., Baulch, D., Cox, R., et al. 1997, *J. Phys. Chem. Ref. Data*, 26, 521
- Baldwin, R. & Walker, R. 1979, *J. Chem. Soc. Faraday Trans. 1*, 75
- Ball, J. A., Gottlieb, C. A., Lilley, A. E., & Radford, H. E. 1970, *ApJ*, 162, L203
- Baulch, D. L., Cobos, C. J., Cox, R. A., et al. 1992, *Journal of Physical and Chemical Reference Data*, 21, 411
- Belloche, A., Garrod, R. T., Müller, H. S. P., & Menten, K. M. 2014, *Science*, 345, 1584
- Belloche, A., Garrod, R. T., Müller, H. S. P., et al. 2009, *A&A*, 499, 215
- Belloche, A., Garrod, R. T., Müller, H. S. P., et al. 2019, *A&A*, 628, A10
- Belloche, A., Meshcheryakov, A. A., Garrod, R. T., et al. 2017, *A&A*, 601, A49
- Belloche, A., Müller, H. S. P., Garrod, R. T., & Menten, K. M. 2016, *A&A*, 587, A91
- Belloche, A., Müller, H. S. P., Menten, K. M., Schilke, P., & Comito, C. 2013, *A&A*, 559, A47
- Bertin, M., Doronin, M., Fillion, J. H., et al. 2017, *A&A*, 598, A18
- Bonfand, M., Belloche, A., Garrod, R. T., et al. 2019, *A&A*, 628, A27
- Cernicharo, J., Agúndez, M., Cabezas, C., et al. 2021, *A&A*, 649, L15
- Charnley, S. B., Kress, M. E., Tielens, A. G. G. M., & Millar, T. J. 1995, *ApJ*, 448, 232
- Curran, H. J. 2006, *Int. J. Chem. Kinet.*, 38, 250
- Daranlot, J., Bergeat, A., Caralp, F., et al. 2010, *Chem. Phys. Chem.*, 11, 4002
- Dean, A. M. & Bozzelli, J. W. 1999, in *Gas-phase Combustion Chemistry*, ed. J. B. S. ed. W. C. Gardiner, 138
- Dobrowolski, J. C., Ostrowski, S., Kołos, R., & Jamróz, M. H. 2008, *Vib. Spectrosc.*, 48, 82
- Durig, J. R., Deeb, H., Darkhalil, I. D., et al. 2011, *J. Mol. Struct.*, 985, 202
- Fukushima, K. & Zwolinski, B. J. 1968, *J. Mol. Spectrosc.*, 26, 368
- Gannon, K., Glowacki, D., Blitz, M., et al. 2007, *J. Phys. Chem. A*, 111, 6679
- Garrod, R. T. 2013, *ApJ*, 765, 60
- Garrod, R. T., Belloche, A., Müller, H. S. P., & Menten, K. M. 2017, *A&A*, 601, A48
- Garrod, R. T. & Herbst, E. 2006, *A&A*, 457, 927
- Garrod, R. T., Jin, M., Matis, K. A., et al. 2022, *ApJS*, 259, 1
- Garrod, R. T. & Pauly, T. 2011, *ApJ*, 735, 15
- Garrod, R. T., Wakelam, V., & Herbst, E. 2007, *A&A*, 467, 1103
- Garrod, R. T., Widicus Weaver, S. L., & Herbst, E. 2008, *ApJ*, 682, 283
- Herbst, E., Messer, J. K., De Lucia, F. C., & Helminger, P. 1984, *J. Mol. Spectrosc.*, 108, 42
- Herbst, E. & van Dishoeck, E. F. 2009, *ARA&A*, 47, 427
- Hu, W.-P., Rossi, I., Corchado, J., & Truhlar, D. 1997, *J. Phys. Chem. A*, 101, 6911
- Izsaak, R., Szori, M., Knowles, P., & Viskolcz, B. 2009, *J. Chem. Theory Comput.*, 5, 2313
- Jimenez-Serra, I., Rodriguez-Almeida, L. F., Martin-Pintado, J., et al. 2022, arXiv e-prints, arXiv:2204.08267
- Jin, M. & Garrod, R. T. 2020, *ApJS*, 249, 26
- Jørgensen, J. K., Belloche, A., & Garrod, R. T. 2020, *ARA&A*, 58, 727
- Jørgensen, J. K., Müller, H. S. P., Calcutt, H., et al. 2018, *A&A*, 620, A170
- Kisiel, Z., Dorosh, O., Maeda, A., et al. 2010, *Physical Chemistry Chemical Physics (Incorporating Faraday Transactions)*, 12, 8329
- Kolesnikov, L., Tercero, B., Cernicharo, J., et al. 2014, *ApJ*, 784, L7
- Lees, R. M. & Baker, J. G. 1968, *J. Chem. Phys.*, 48, 5299
- Loison, J., Daranlot, J., Bergeat, A., et al. 2010, *J. Phys. Chem. A*, 114, 13326
- Maeda, A., De Lucia, F. C., Herbst, E., et al. 2006a, *ApJS*, 162, 428
- Maeda, A., Medvedev, I. R., De Lucia, F. C., & Herbst, E. 2006b, *ApJS*, 166, 650
- Manigand, S., Coutens, A., Loison, J. C., et al. 2021, *A&A*, 645, A53
- Maret, S., Hily-Blant, P., Pety, J., Bardeau, S., & Reynier, E. 2011, *A&A*, 526, A47
- McGuire, B. A., Loomis, R. A., Burkhardt, A. M., et al. 2021, *Science*, 371, 1265
- Melosso, M., Belloche, A., Martin-Drumel, M. A., et al. 2020, *A&A*, 641, A160
- Müller, H. S. P., Belloche, A., Xu, L.-H., et al. 2016, *A&A*, 587, A92
- Müller, H. S. P., Menten, K. M., & Mäder, H. 2004, *A&A*, 428, 1019
- Müller, H. S. P., Schlöder, F., Stutzki, J., & Winnewisser, G. 2005, *Journal of Molecular Structure*, 742, 215
- Olm, C., Varga, T., Valko, E., et al. 2016, *Int. J. Chem. Kinet.*, 48, 423
- Pearson, J. C., Brauer, C. S., & Drouin, B. J. 2008, *Journal of Molecular Spectroscopy*, 251, 394
- Pearson, J. C., Sastry, K. V. L. N., Herbst, E., & De Lucia, F. C. 1996, *J. Mol. Spectrosc.*, 175, 246
- Pearson, J. C., Sastry, K. V. L. N., Herbst, E., & De Lucia, F. C. 1997, *ApJ*, 480, 420
- Pearson, J. C., Sastry, K. V. L. N., Winnewisser, M., Herbst, E., & De Lucia, F. C. 1995, *J. Phys. Chem. Ref. Data*, 24, 1
- Pickett, H. M., Cohen, E. A., Brinza, D. E., & Schaefer, M. M. 1981, *J. Mol. Spectrosc.*, 89, 542
- Qasim, D., Fedoseev, G., Chuang, K. J., et al. 2019, *A&A*, 627, A1
- Rao, H., Zeng, X., He, H., & Li, Z. 2011, *J. Phys. Chem. A*, 115, 1602
- Reid, M. J., Menten, K. M., Brunthaler, A., et al. 2019, *ApJ*, 885, 131
- Rodríguez-Almeida, L. F., Rivilla, V. M., Jiménez-Serra, I., et al. 2021, *A&A*, 654, L1
- Sánchez-Monge, Á., Schilke, P., Schmiedeke, A., et al. 2017, *A&A*, 604, A6
- Sanz-Novo, M., Belloche, A., Rivilla, V. M., et al. 2022, arXiv e-prints, arXiv:2203.07334
- Sastry, K. V. L. N., Lees, R. M., & De Lucia, F. C. 1984, *J. Mol. Spectrosc.*, 103, 486
- Sivaramakrishnan, R., Su, M., Michael, J., et al. 2010, *J. Phys. Chem. A*, 114, 9425
- Sun, J., Tang, Y., Sun, H., et al. 2008, *Chem. Phys. Lett.*, 463, 315
- Taquet, V., Wirstrom, E. S., & Charnley, S. B. 2016, *ApJ*, 821, 46
- Tercero, B., Cernicharo, J., López, A., et al. 2015, *A&A*, 582, L1
- Thomsen, D. & Jørgensen, S. 2009, *Chem. Phys. Lett.*, 481, 29
- Tsang, W. 1988, *J. Phys. Chem. Ref. Data*, 17, 887
- Tsang, W. 1991, *J. Phys. Chem. Ref. Data*, 20, 221
- Tsang, W. 1992, *Ind. Eng. Chem.*, 31, 3
- Xu, L.-H., Fisher, J., Lees, R. M., et al. 2008, *Journal of Molecular Spectroscopy*, 251, 305
- Zingsheim, O., Müller, H. S. P., & et al. 2022
- Zuckerman, B., Turner, B. E., Johnson, D. R., et al. 1975, *ApJ*, 196, L99

## Appendix A: Complementary figures: Spectra

Figures A.1–A.12 show the transitions of  $\text{CH}_3\text{OH } v = 0$ ,  $\text{CH}_3\text{OH } v_t = 1$ ,  $\text{CH}_3\text{OH } v_t = 2$ ,  $\text{CH}_3\text{OH } v_t = 3$ ,  $\text{C}_2\text{H}_5\text{OH}$ ,  $g\text{-}i\text{-C}_3\text{H}_7\text{OH}$ ,  $a\text{-}i\text{-C}_3\text{H}_7\text{OH}$ ,  $Ga\text{-}n\text{-C}_3\text{H}_7\text{OH}$ ,  $Gg\text{-}n\text{-C}_3\text{H}_7\text{OH}$ ,  $Gg'\text{-}n\text{-C}_3\text{H}_7\text{OH}$ ,  $Aa\text{-}n\text{-C}_3\text{H}_7\text{OH}$ , and  $Ag\text{-}n\text{-C}_3\text{H}_7\text{OH}$ , respectively, that are covered by the ReMoCA survey and contribute significantly to the signal detected toward Sgr B2(N2b). Transitions of a given molecule that are too heavily blended with much stronger emission from other molecules and therefore cannot contribute to the identification of this molecule are not shown in these figures.

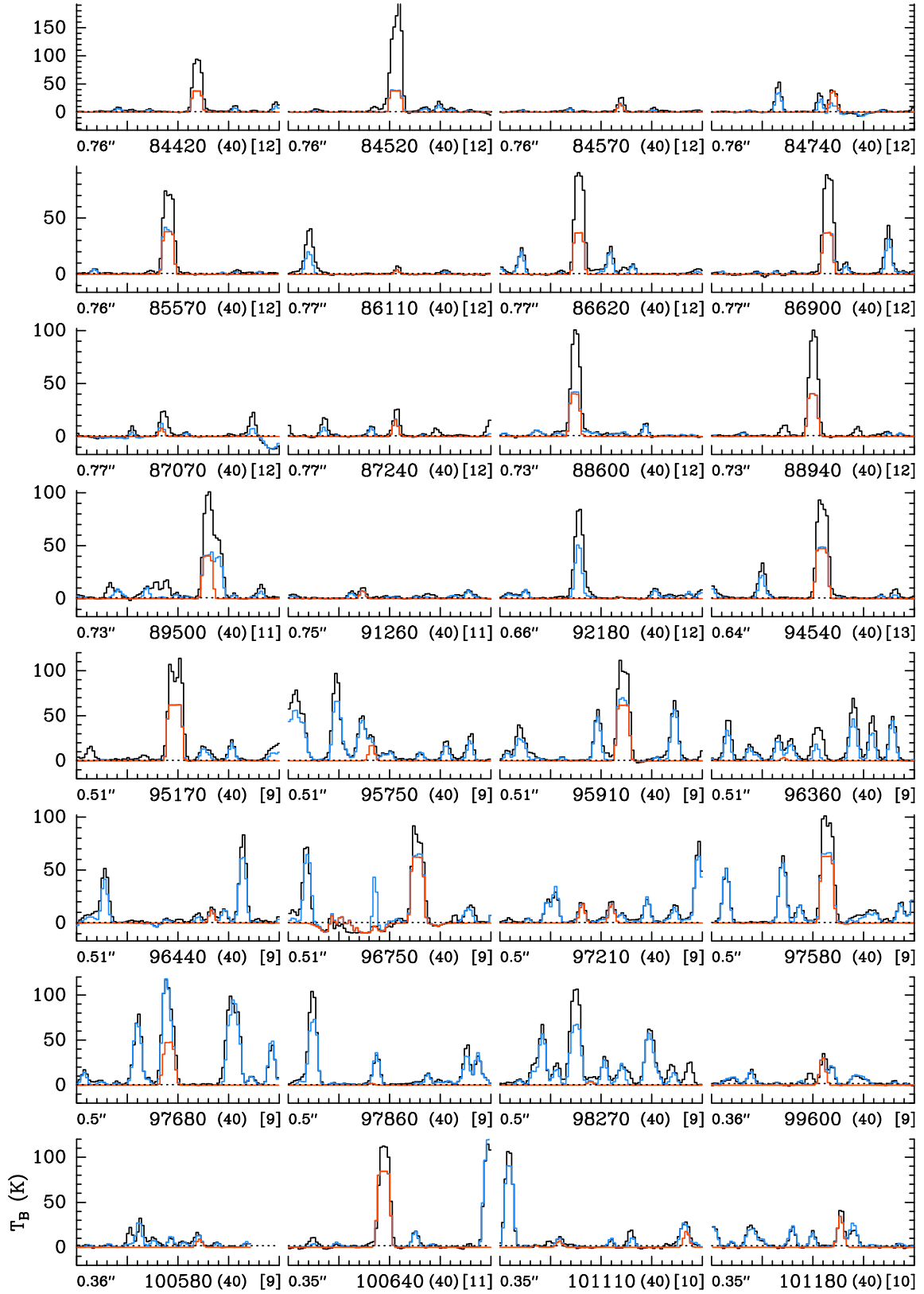


**Fig. A.1.** Transitions of  $\text{CH}_3\text{OH}$ ,  $v = 0$  covered by the ReMoCA survey with ALMA. The best-fit LTE synthetic spectrum of  $\text{CH}_3\text{OH}$ ,  $v = 0$  is displayed in red and overlaid on the observed spectrum of Sgr B2(N2b) shown in black. The blue synthetic spectrum contains the contributions of all molecules identified in our survey so far, including the species shown in red. The central frequency is indicated in MHz below each panel as well as the half-power beam width on the left, the width of each panel in MHz in parentheses, and the continuum level in K of the baseline-subtracted spectra in brackets. The y-axis is labeled in brightness temperature units (K). The dotted line indicates the  $3\sigma$  noise level.

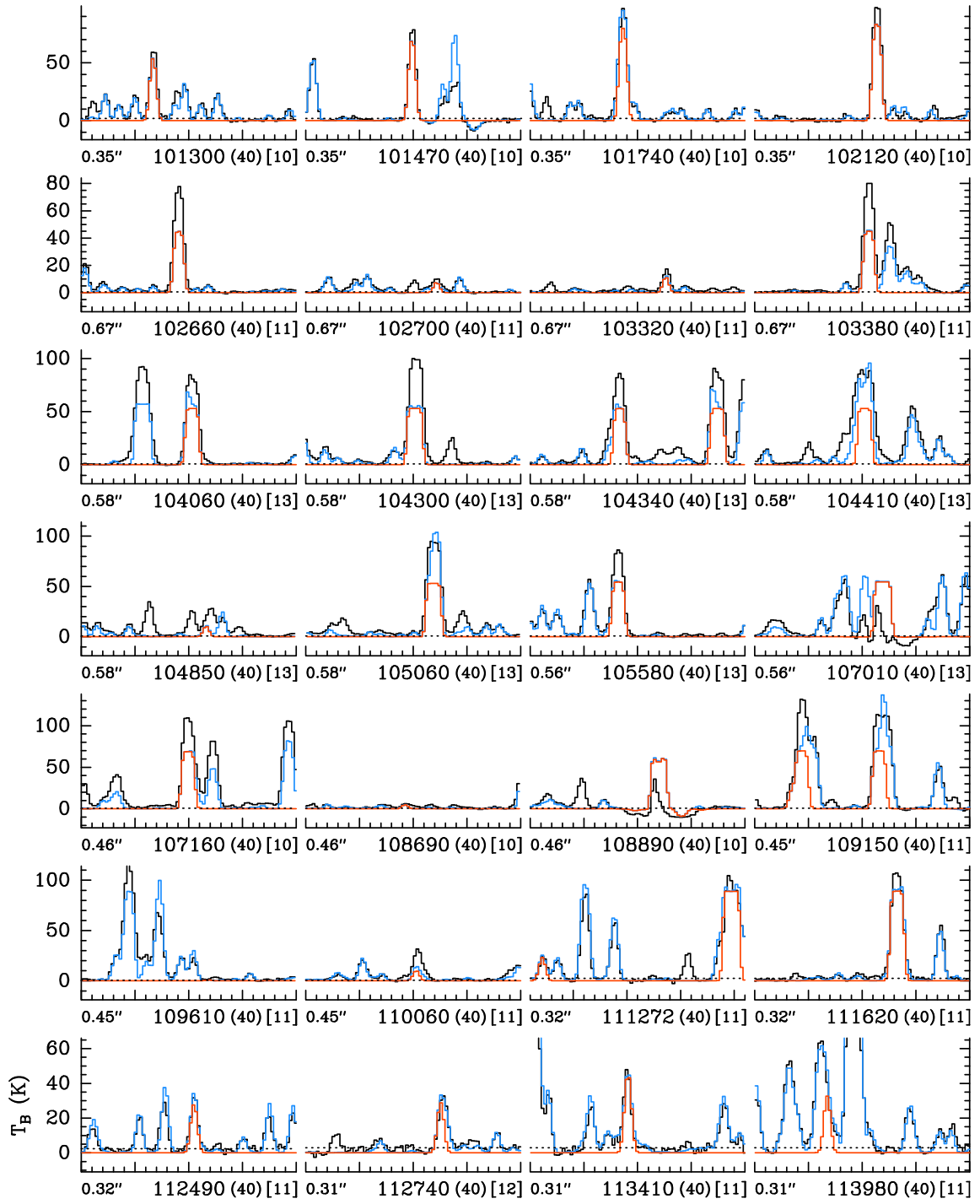
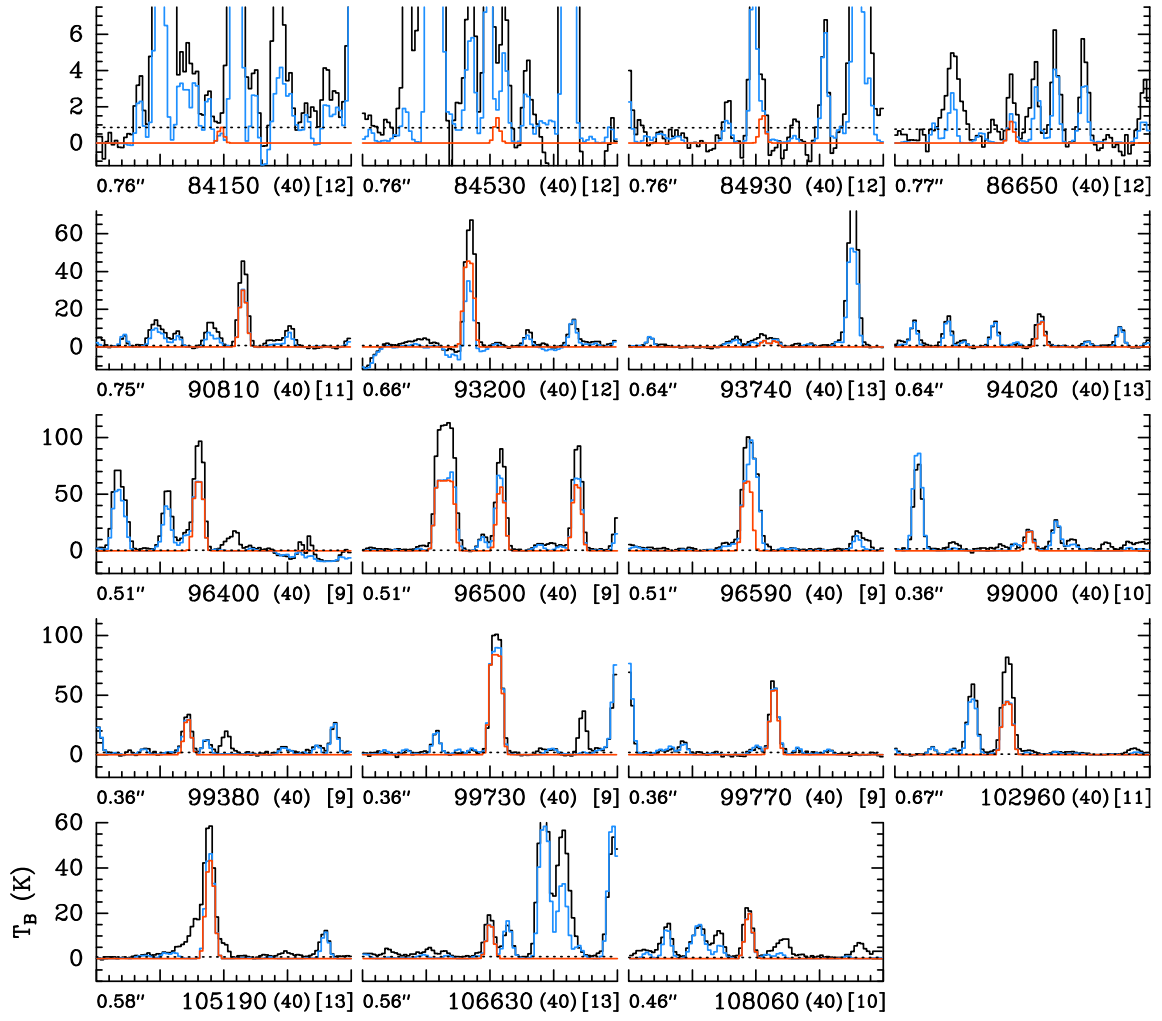
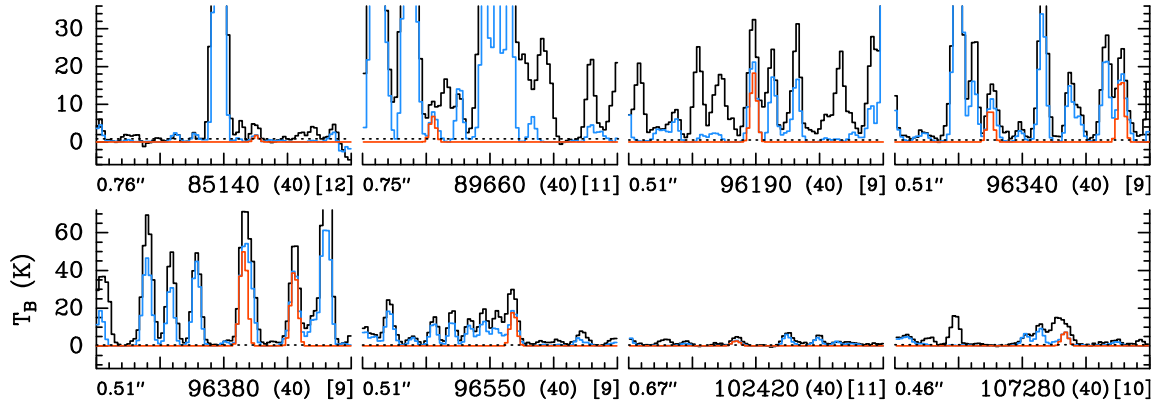


Fig. A.1. continued.





**Fig. A.2.** Same as Fig. A.1 but for  $\text{CH}_3\text{OH}$ ,  $v_t=1$ .



**Fig. A.3.** Same as Fig. A.1 but for  $\text{CH}_3\text{OH}$ ,  $v_t=2$ .

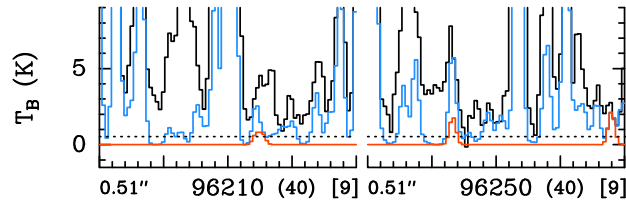


**Fig. A.4.** Same as Fig. A.1 but for  $\text{CH}_3\text{OH}$ ,  $v_t=3$ .

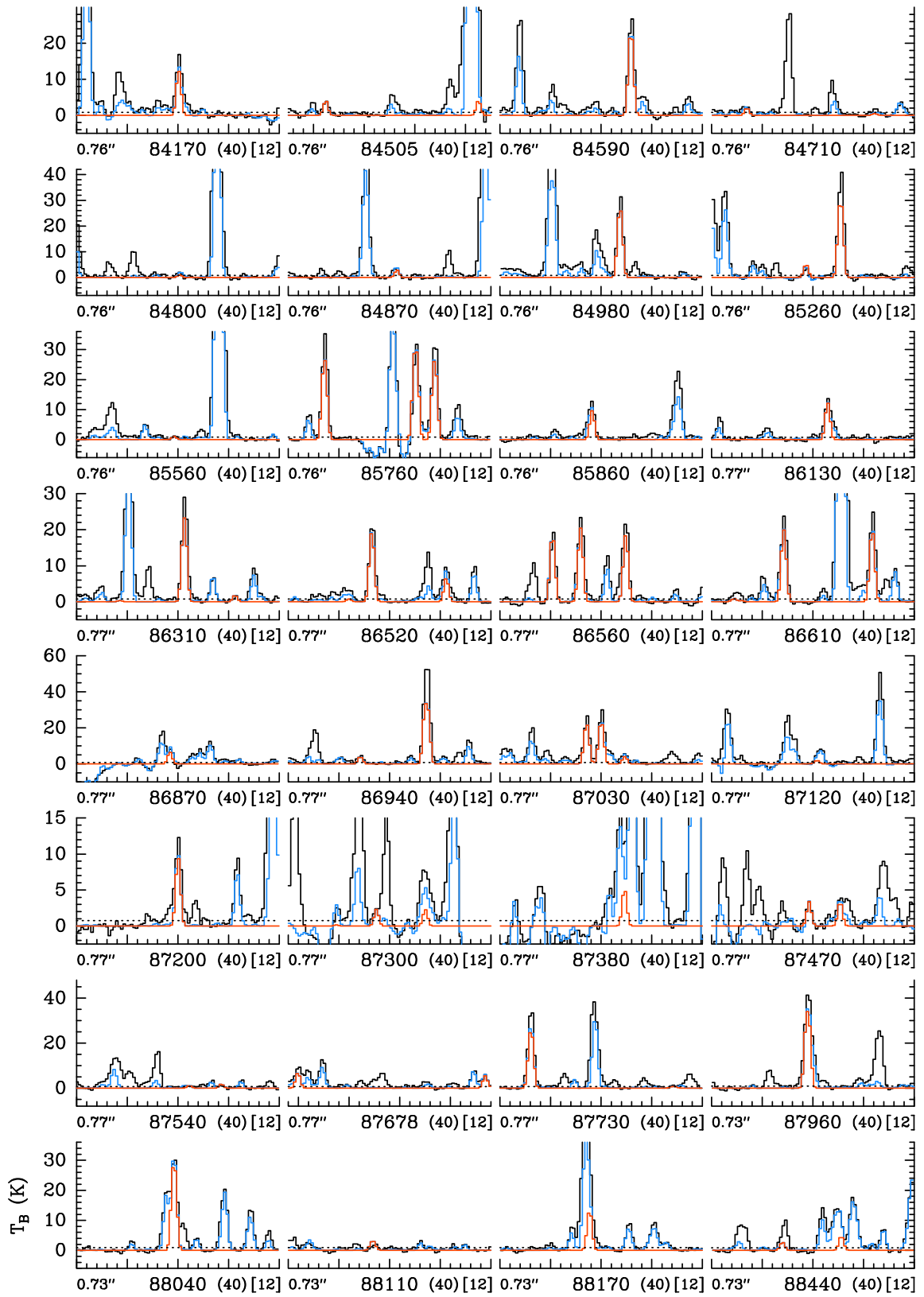


**Fig. A.5.** Same as Fig. A.1 but for  $C_2H_5OH$ ,  $v=0$ .

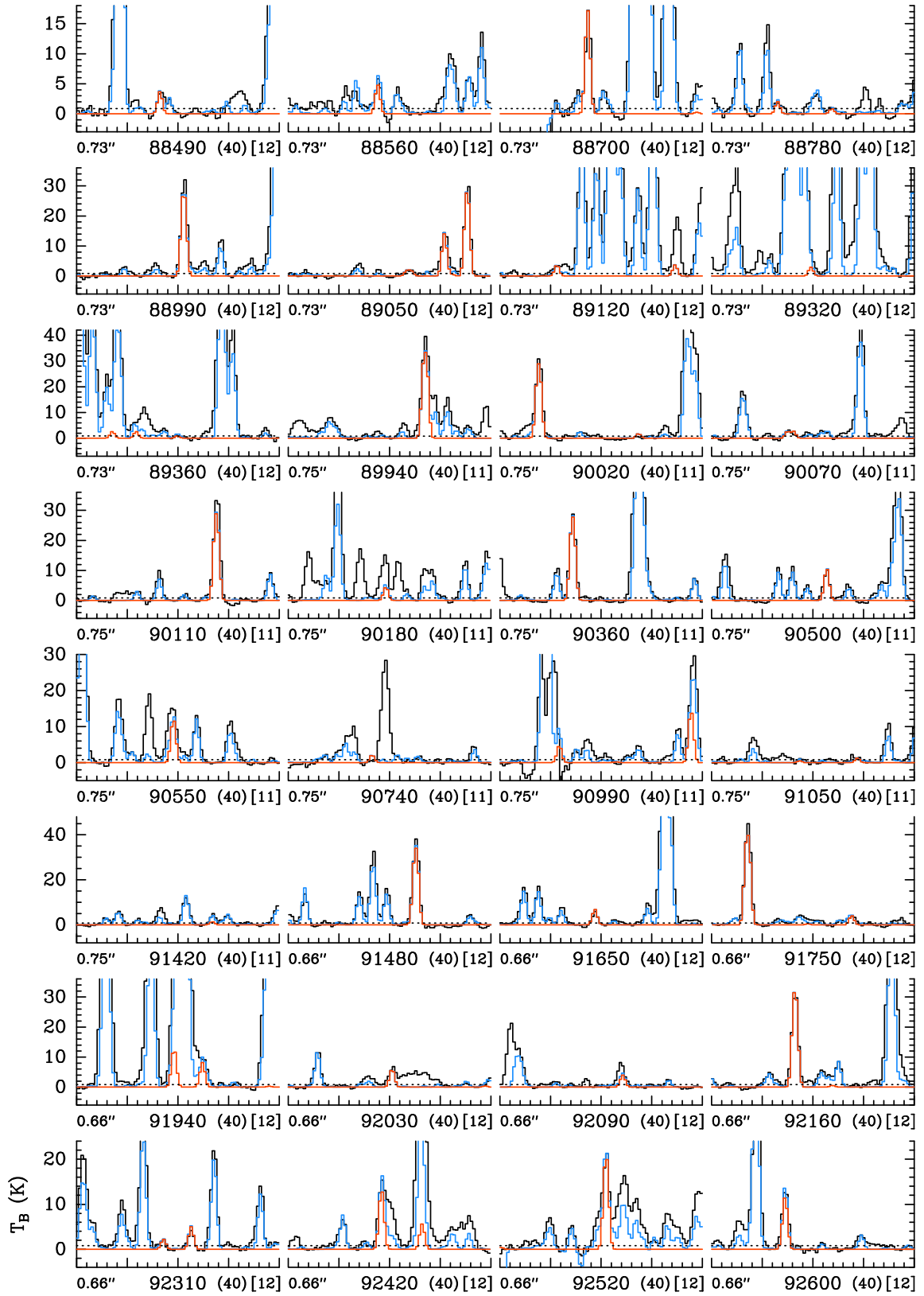


Fig. A.5. continued.

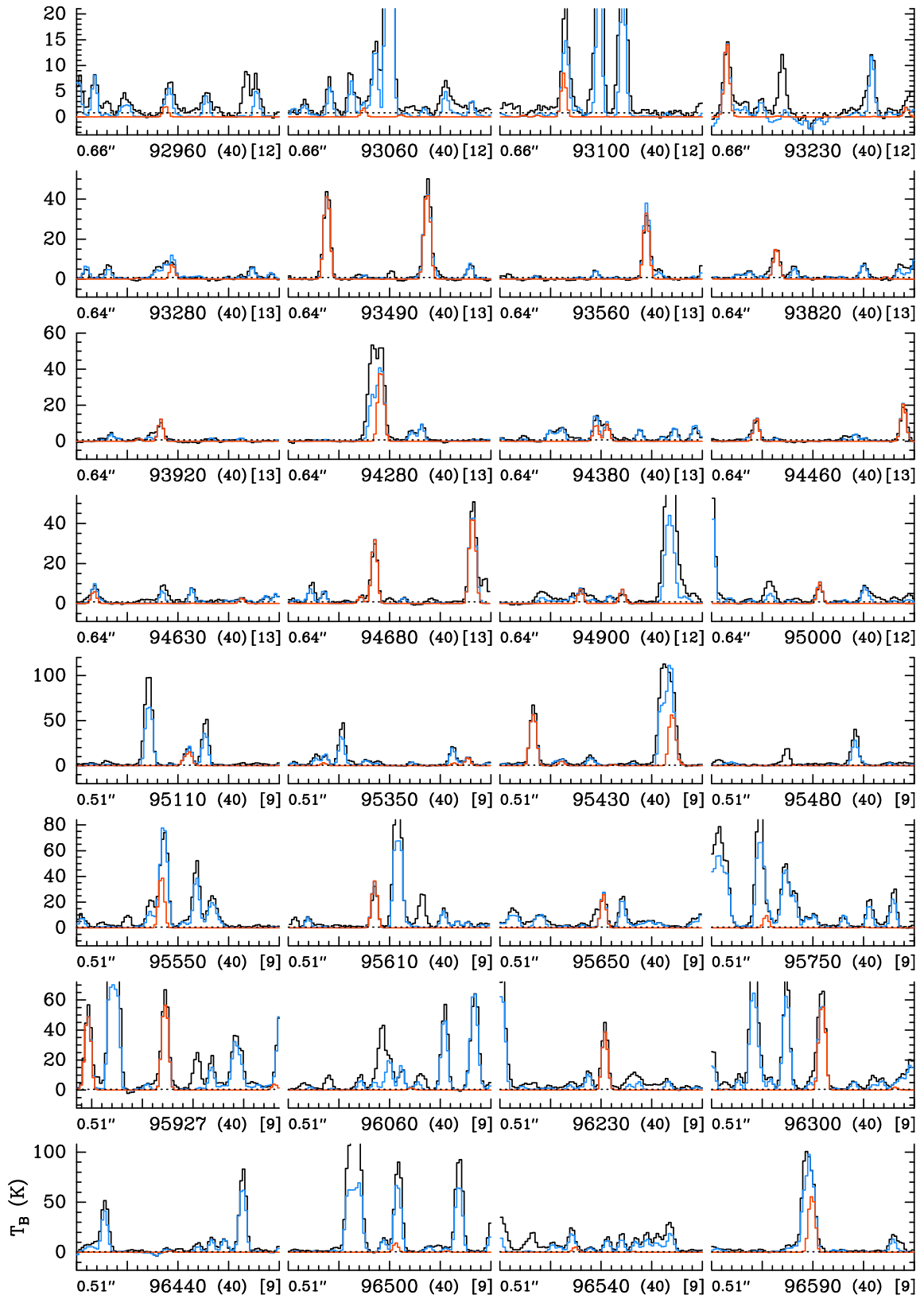


Fig. A.5. continued.

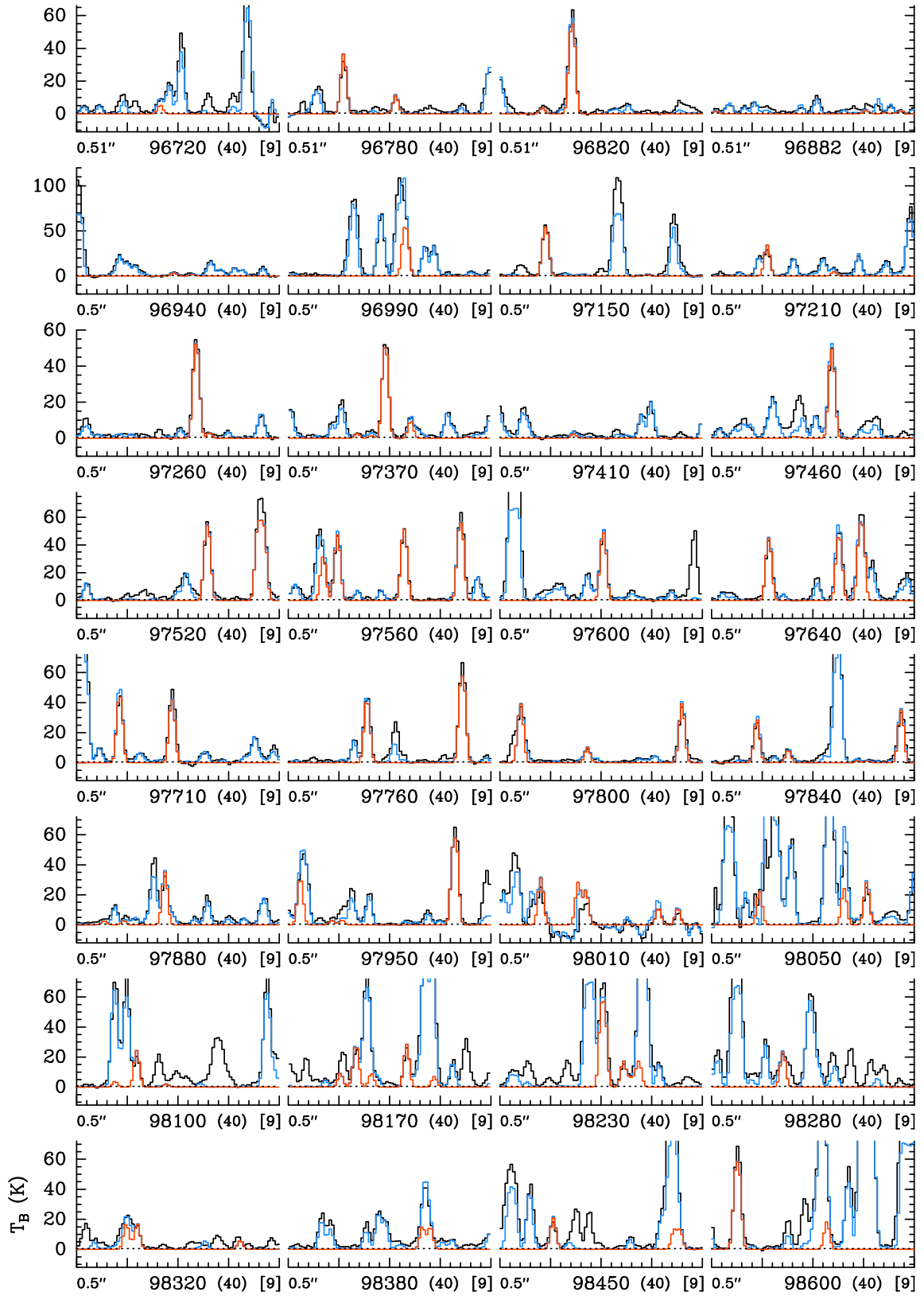


Fig. A.5. continued.

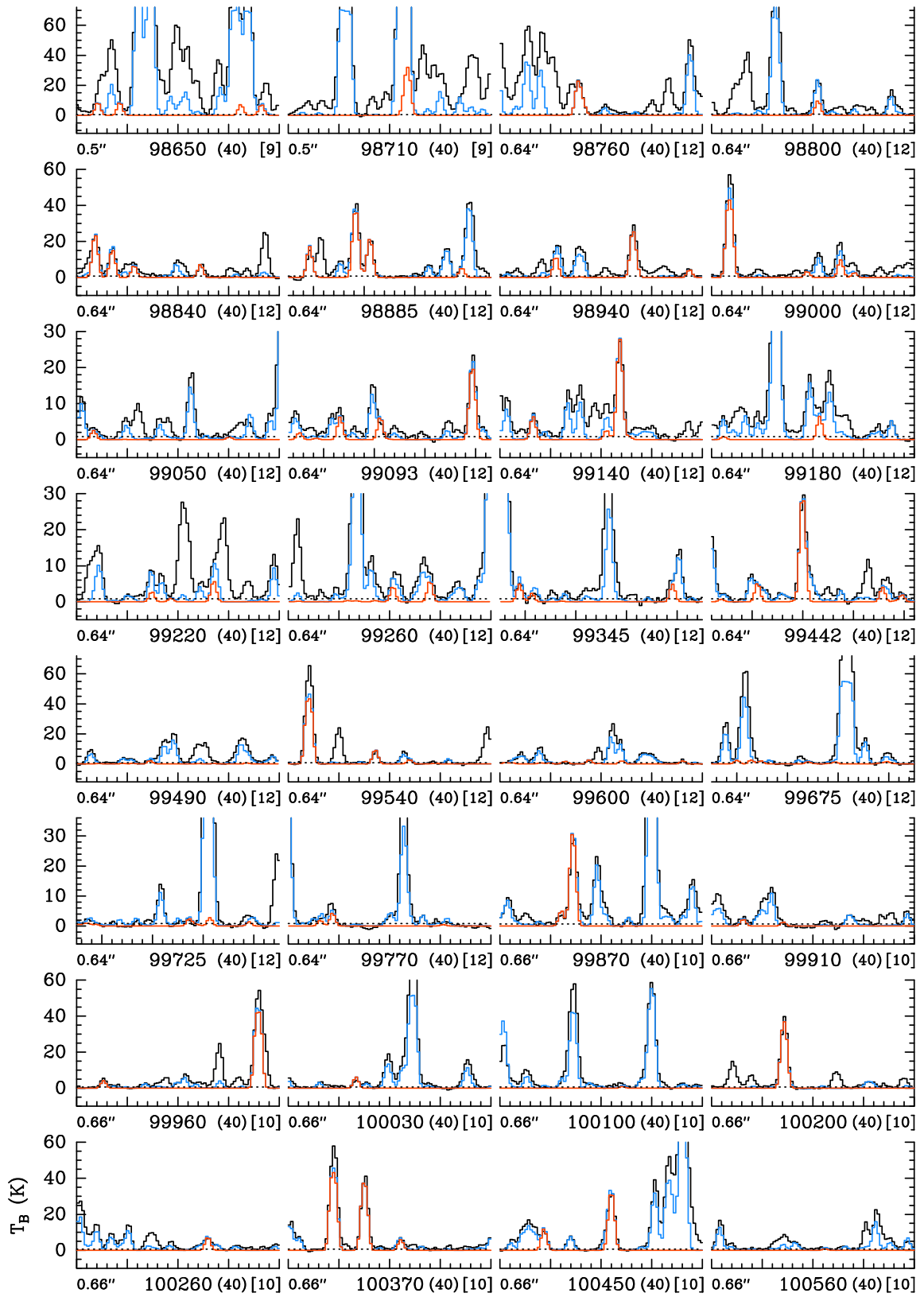


Fig. A.5. continued.



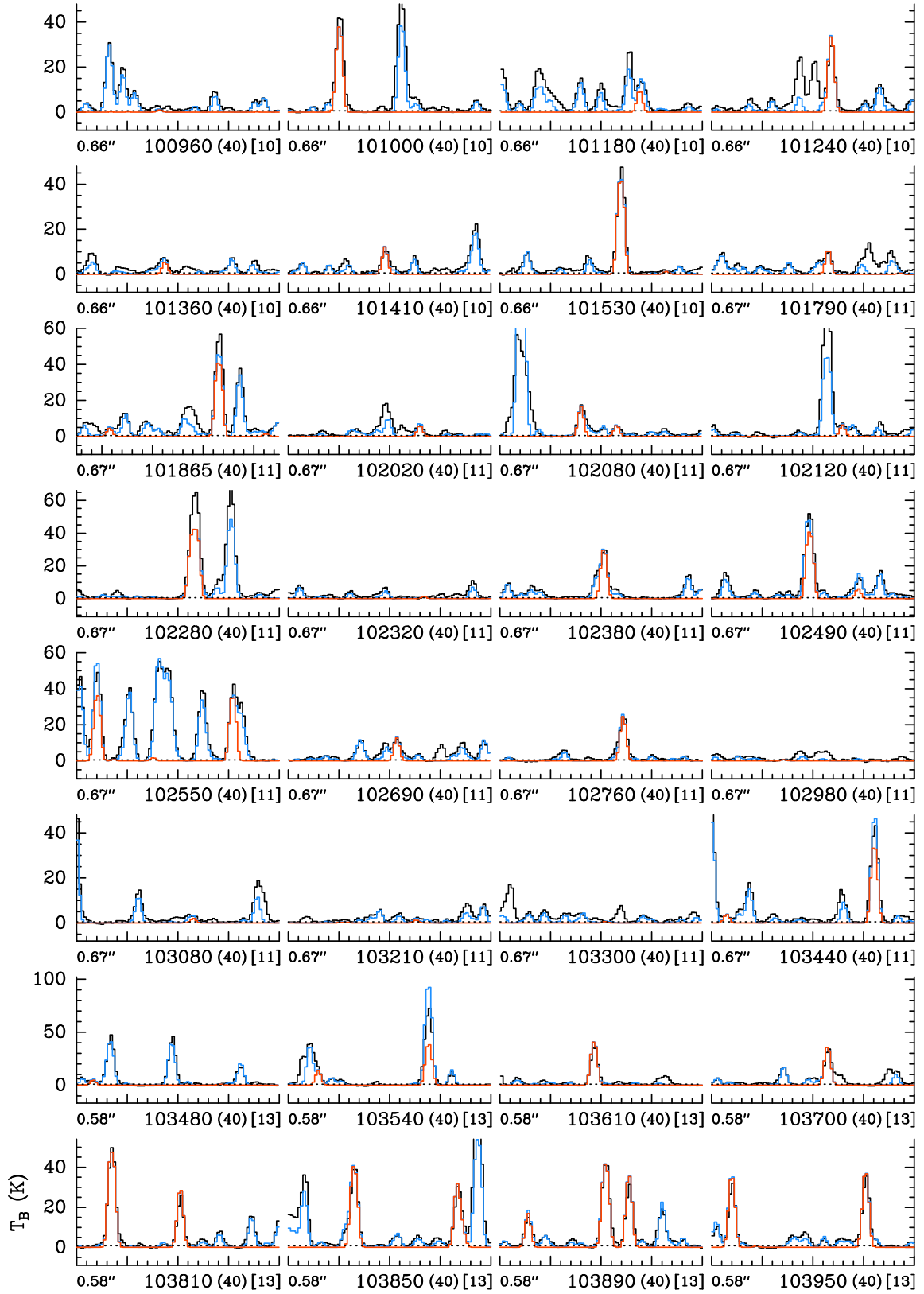


Fig. A.5. continued.

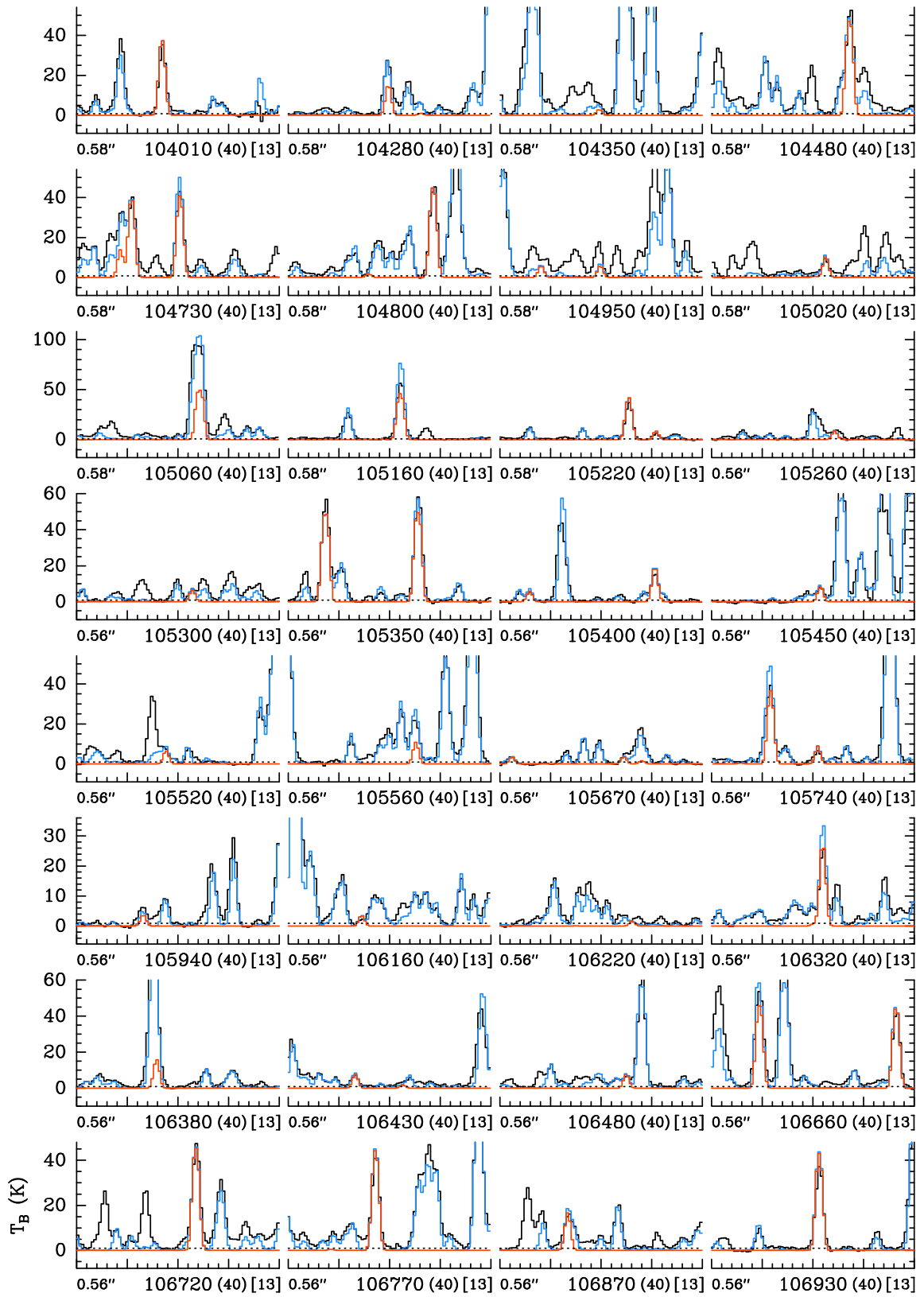


Fig. A.5. continued.

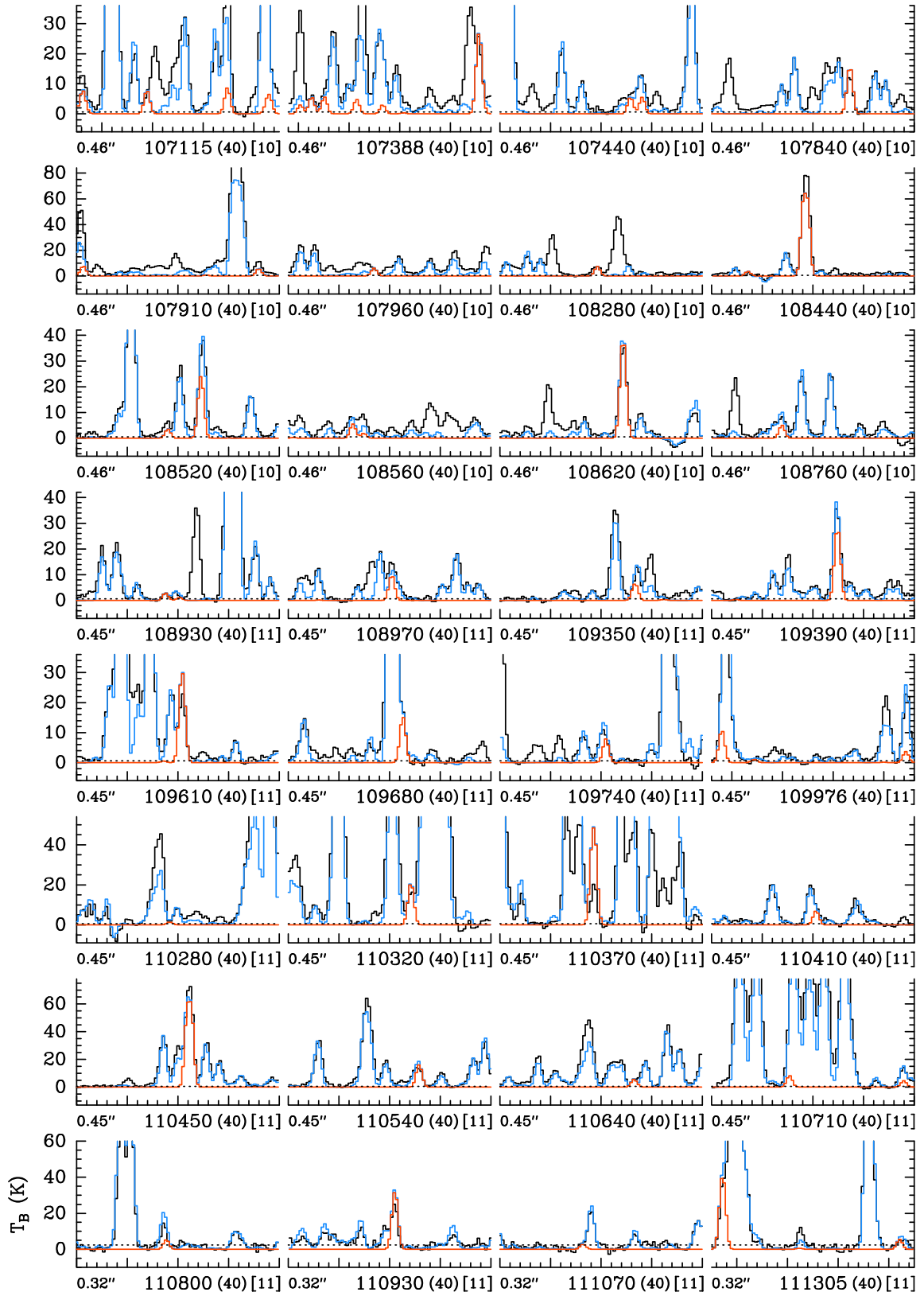


Fig. A.5. continued.

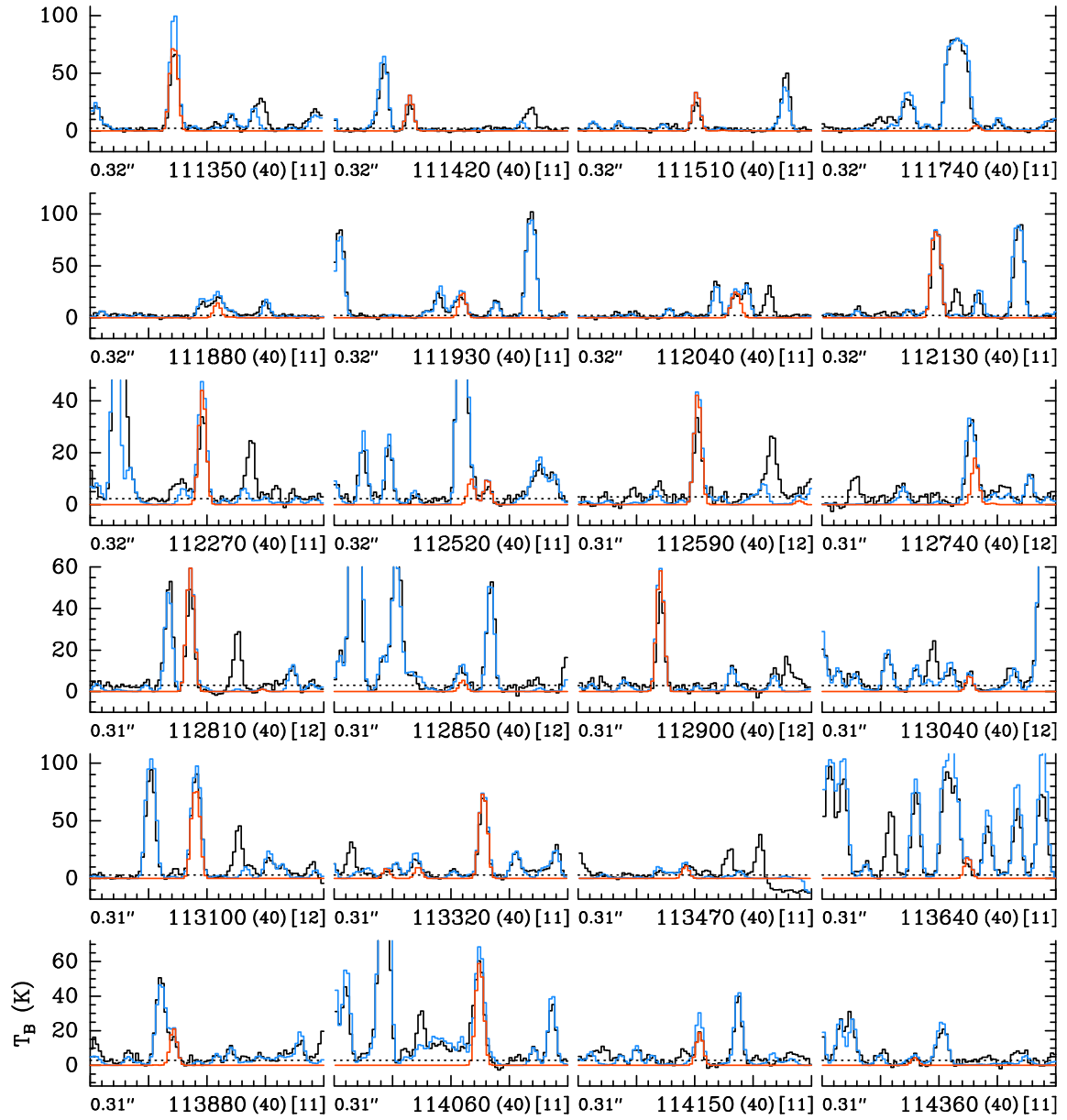
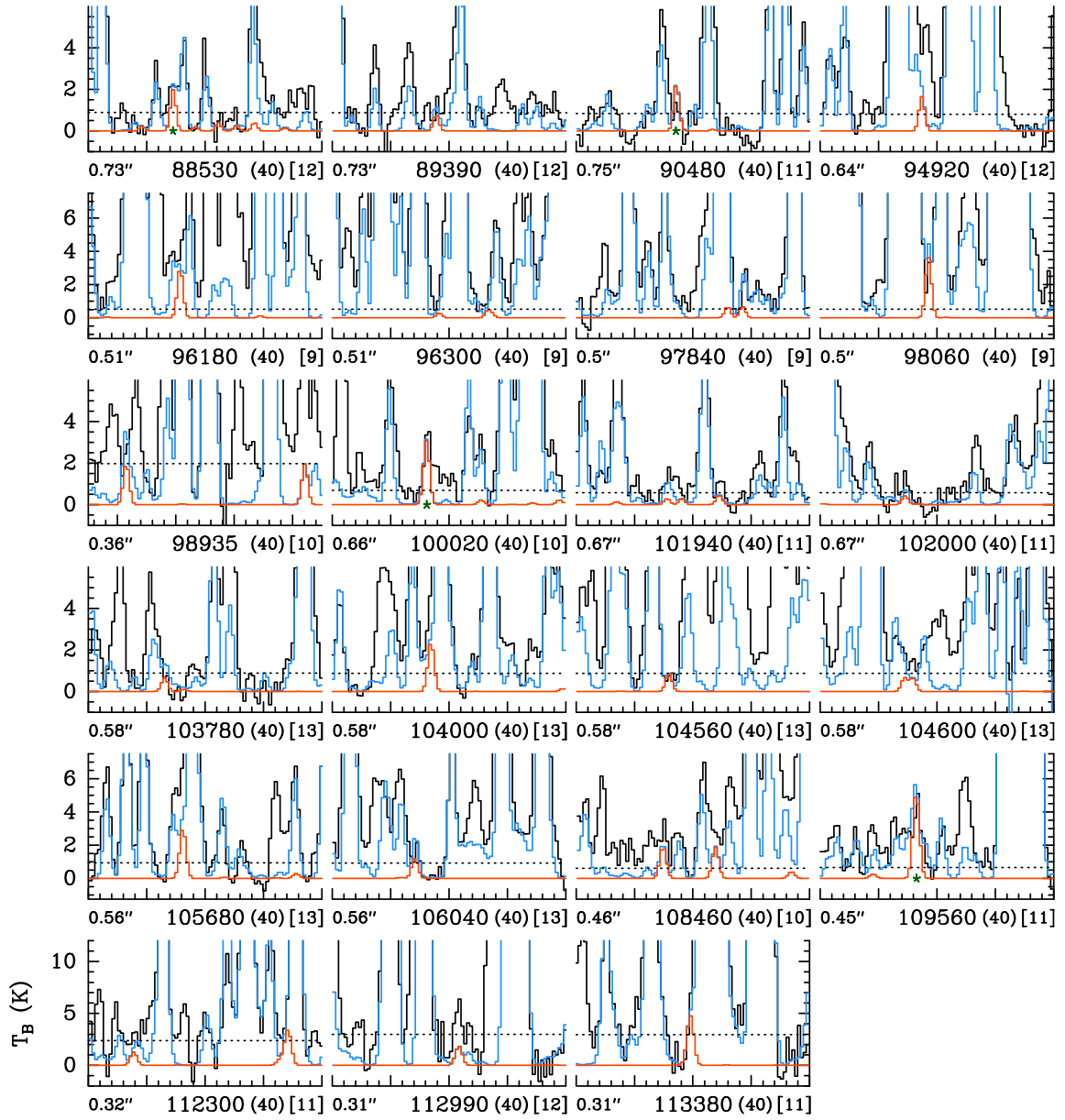
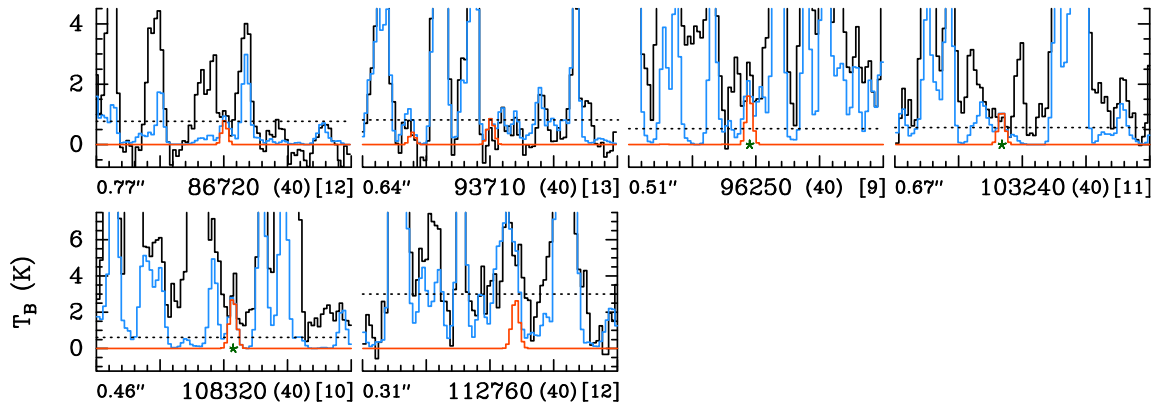


Fig. A.5. continued.



**Fig. A.6.** Same as Fig. A.1 but for *g-i*-C<sub>3</sub>H<sub>7</sub>OH,  $v=0$ . The green stars mark the transitions that we consider as detected.



**Fig. A.7.** Same as Fig. A.1 but for *a-i*-C<sub>3</sub>H<sub>7</sub>OH,  $v=0$ . The green stars mark the transitions that we consider as detected.

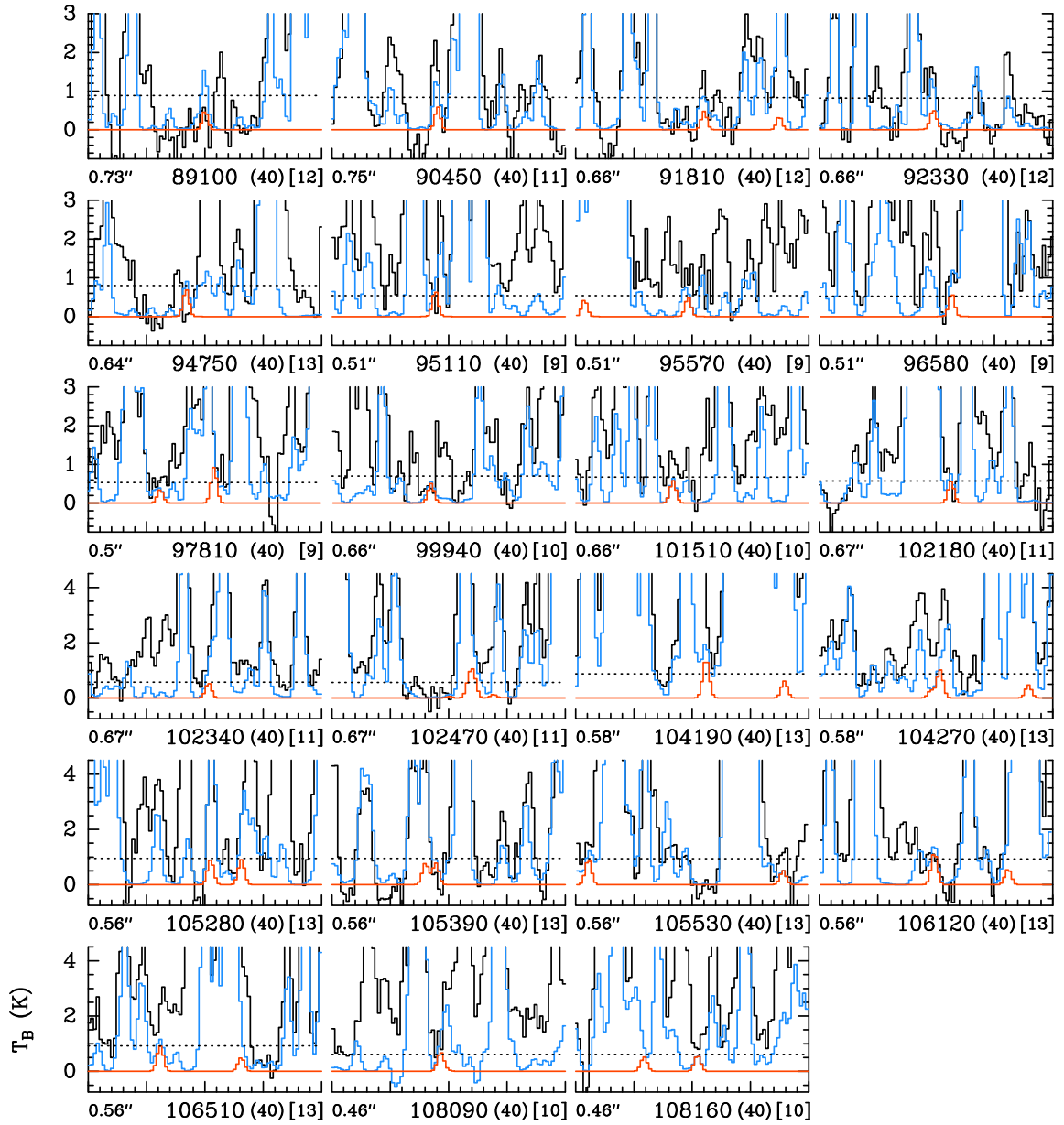


**Fig. A.8.** Same as Fig. A.1 but for *Ga-n*-C<sub>3</sub>H<sub>7</sub>OH,  $v=0$ .

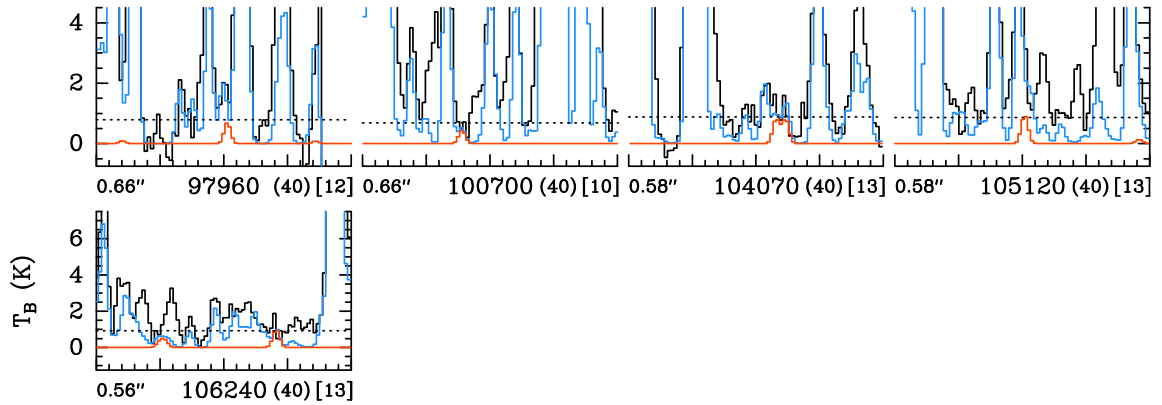


**Fig. A.9.** Same as Fig. A.1 but for *Gg-n*-C<sub>3</sub>H<sub>7</sub>OH,  $v=0$ .



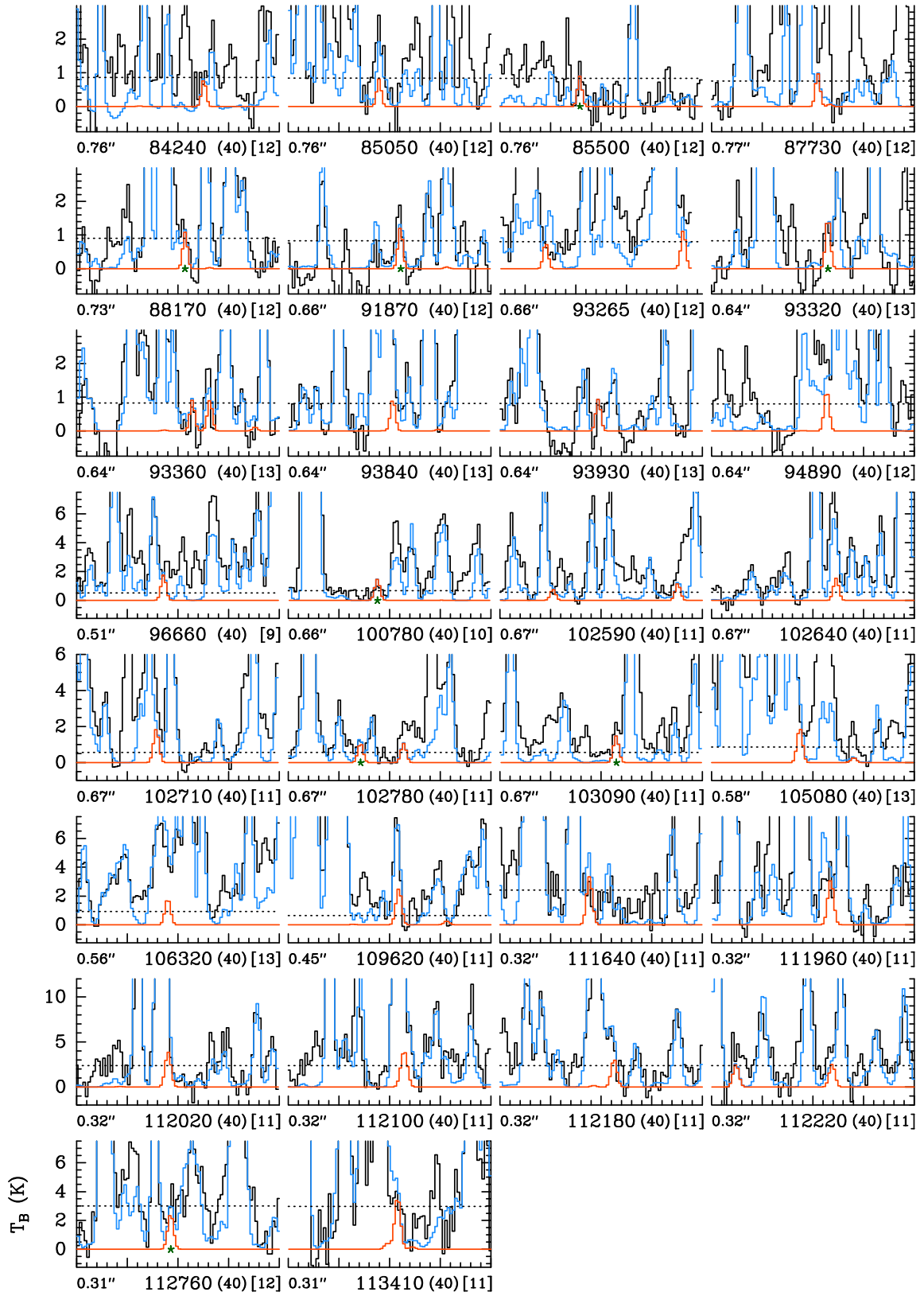


**Fig. A.10.** Same as Fig. A.1 but for  $Gg'$ - $n$ - $C_3H_7OH$ ,  $v=0$ . The green stars mark the transitions that we consider as detected.

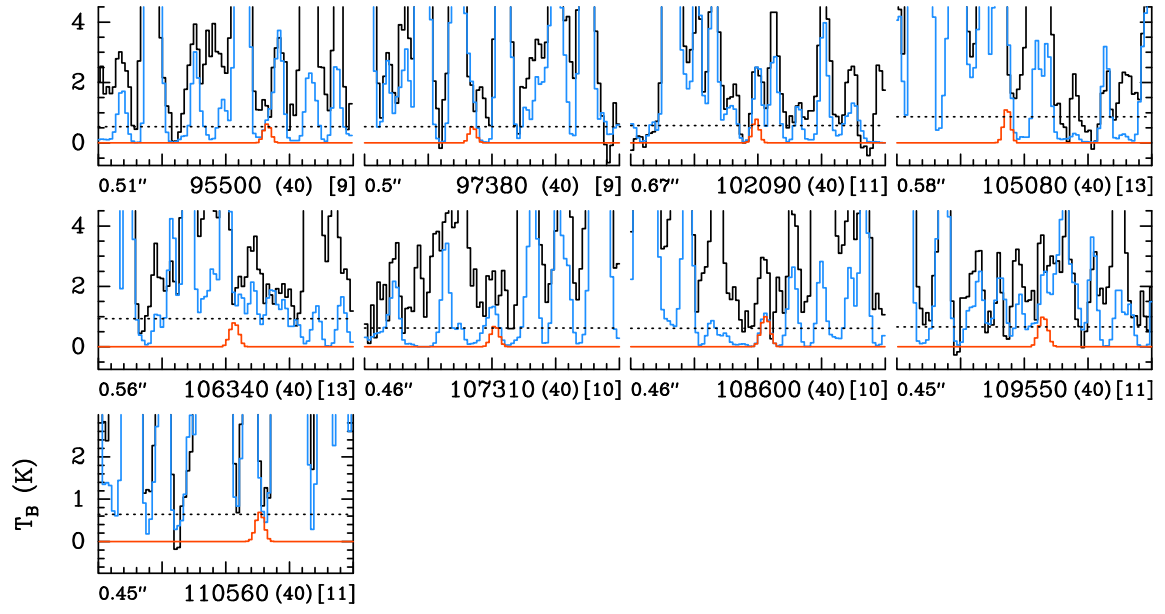


**Fig. A.11.** Same as Fig. A.1 but for  $Aa-n-C_3H_7OH$ ,  $v=0$ .

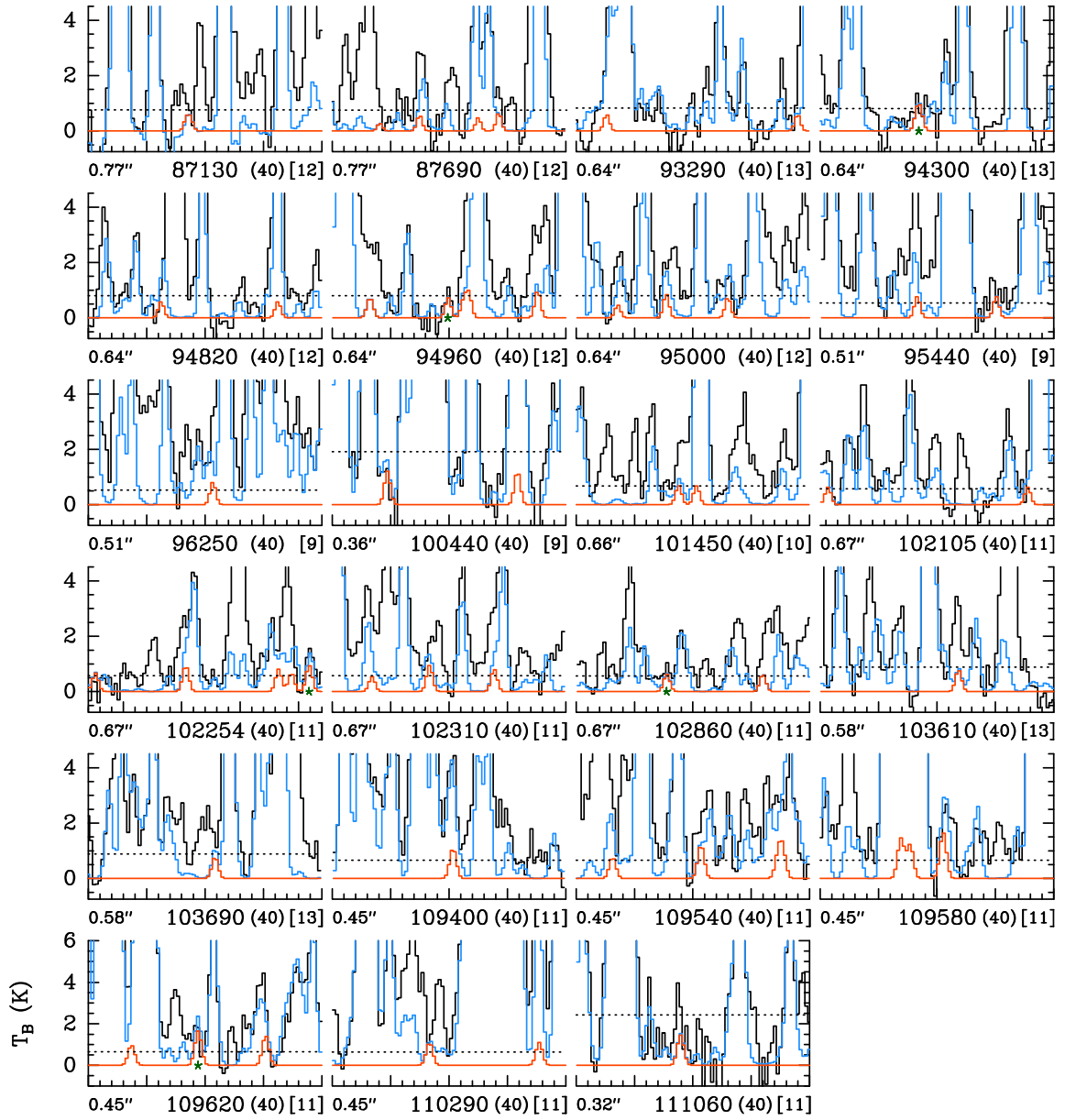


**Fig. A.12.** Same as Fig. A.1 but for  $Ag-n-C_3H_7OH$ ,  $v=0$ . The green stars mark the transitions that we consider as detected.

## Appendix B: Complementary figures: Population diagrams

Figures B.1–B.6 show the population diagrams of  $\text{CH}_3\text{OH}$ ,  $\text{C}_2\text{H}_5\text{OH}$ ,  $g$ - $i$ - $\text{C}_3\text{H}_7\text{OH}$ ,  $a$ - $i$ - $\text{C}_3\text{H}_7\text{OH}$ ,  $Gg'$ - $n$ - $\text{C}_3\text{H}_7\text{OH}$ , and  $Ag$ - $n$ - $\text{C}_3\text{H}_7\text{OH}$ , respectively, toward Sgr B2(N2b).

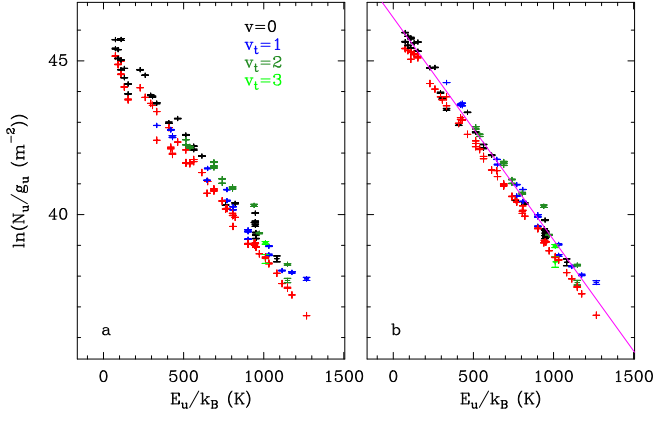


**Fig. B.1.** Population diagram of  $\text{CH}_3\text{OH}$  toward Sgr B2(N2b). The observed data points are shown in various colors (but not red) as indicated in the upper right corner of panel **a** while the synthetic populations are shown in red. No correction is applied in panel **a**. In panel **b**, the optical depth correction has been applied to both the observed and synthetic populations and the contamination by all other species included in the full model has been removed from the observed data points. The purple line is a linear fit to the observed populations (in linear-logarithmic space).

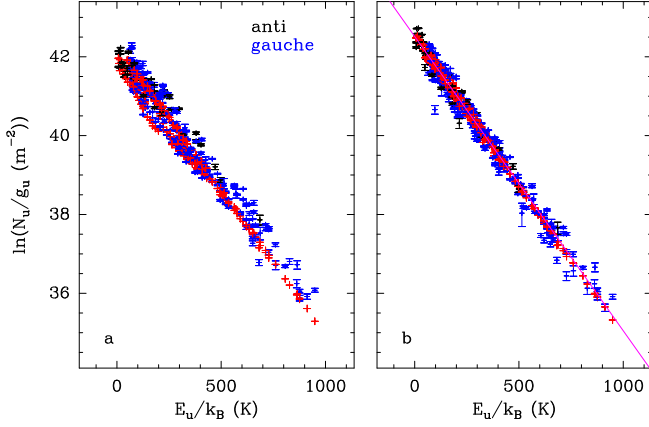


**Fig. B.2.** Same as Fig. B.1 for  $\text{C}_2\text{H}_5\text{OH}$ . The observed data points of the *anti* and *gauche* conformers of  $\text{C}_2\text{H}_5\text{OH}$  are shown in black and blue, respectively.

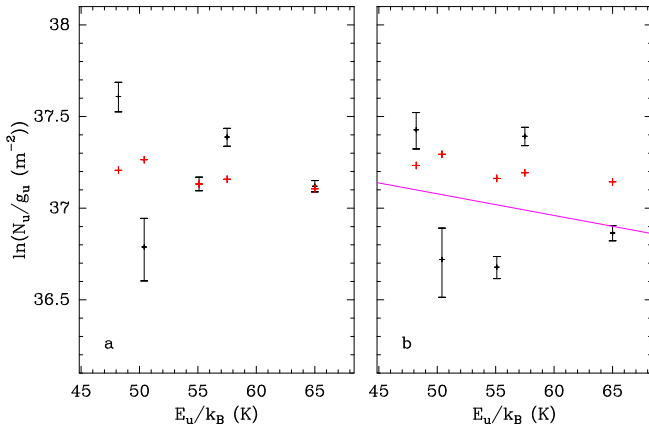


**Fig. B.3.** Same as Fig. B.1 for *g-i*- $\text{C}_3\text{H}_7\text{OH}$ .

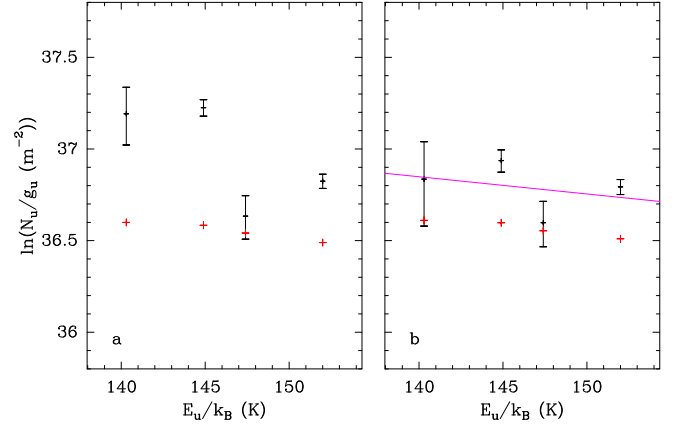


**Fig. B.4.** Same as Fig. B.1 for *a-i*- $\text{C}_3\text{H}_7\text{OH}$ .

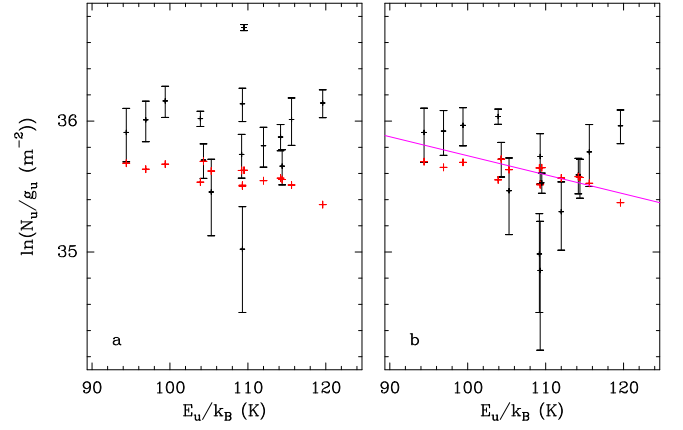


**Fig. B.5.** Same as Fig. B.1 for *Gg'-n*- $\text{C}_3\text{H}_7\text{OH}$ .

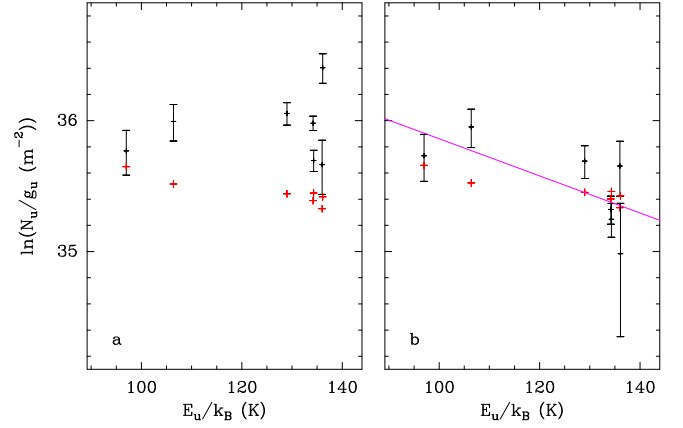


**Fig. B.6.** Same as Fig. B.1 for *Ag-n*- $\text{C}_3\text{H}_7\text{OH}$ .

## **Appendix C: Tables of chemical model input data**

**Table C.1.** Grain-surface/ice-mantle reactions involved in the formation of vinyl, ethyl, propyl alcohols, as well as updated reactions related to propyl cyanide production. Garrod et al. (2017) provide a more complete list of cyanide-related reactions.

#	Reaction					BR	$F_{\text{dir}}$	$F_{\text{comp}}$	$E_A$ (K)	Ref.
1	H	+	C <sub>2</sub> H <sub>3</sub> OH	→	CH <sub>3</sub> CHOH	—	0.375	0.25	604	a
2	H	+	C <sub>2</sub> H <sub>3</sub> OH	→	CH <sub>2</sub> CH <sub>2</sub> OH	—	0.25	1.00	1850	a
3	CH <sub>2</sub>	+	CH <sub>2</sub> OH	→	CH <sub>2</sub> CH <sub>2</sub> OH	—	—	—	—	
4	CH <sub>3</sub>	+	CH <sub>2</sub> OH	→	C <sub>2</sub> H <sub>3</sub> OH	—	—	—	—	
5	CH <sub>2</sub> CH <sub>3</sub>	+	OH	→	C <sub>2</sub> H <sub>3</sub> OH	0.5	—	—	—	
6	CH <sub>2</sub> CH <sub>3</sub>	+	OH	→	C <sub>2</sub> H <sub>4</sub>	0.5	—	—	—	
7	OH	+	C <sub>2</sub> H <sub>4</sub>	→	CH <sub>2</sub> CH <sub>2</sub> OH	—	—	—	0	b
8	OH	+	C <sub>2</sub> H <sub>4</sub>	→	CHCH <sub>2</sub>	0.5	—	—	2990	c
9	O	+	CH <sub>2</sub> CH <sub>3</sub>	→	C <sub>2</sub> H <sub>3</sub> O	—	—	—	—	
10	H	+	CH <sub>3</sub> CHOH	→	C <sub>2</sub> H <sub>3</sub> OH	0.5	—	—	—	
11	H	+	CH <sub>3</sub> CHOH	→	C <sub>2</sub> H <sub>3</sub> OH	0.5	—	—	—	
12	H	+	CH <sub>2</sub> CH <sub>2</sub> OH	→	C <sub>2</sub> H <sub>3</sub> OH	0.5	—	—	—	
13	H	+	CH <sub>2</sub> CH <sub>2</sub> OH	→	C <sub>2</sub> H <sub>3</sub> OH	0.5	—	—	—	
14	H	+	C <sub>2</sub> H <sub>3</sub> O	→	C <sub>2</sub> H <sub>3</sub> OH	—	—	—	—	
15	CH <sub>2</sub>	+	CH <sub>2</sub> CH <sub>2</sub> OH	→	CH <sub>2</sub> CH <sub>2</sub> CH <sub>2</sub> OH	—	—	—	—	
16	CH <sub>3</sub>	+	CH <sub>2</sub> CH <sub>2</sub> OH	→	<i>n</i> -C <sub>3</sub> H <sub>7</sub> OH	—	—	—	—	
17	CH <sub>2</sub> CH <sub>3</sub>	+	CH <sub>2</sub> OH	→	<i>n</i> -C <sub>3</sub> H <sub>7</sub> OH	0.333	—	—	—	
18	CH <sub>2</sub> CH <sub>3</sub>	+	CH <sub>2</sub> OH	→	CH <sub>3</sub> OH	0.333	—	—	—	
19	CH <sub>2</sub> CH <sub>3</sub>	+	CH <sub>2</sub> OH	→	H <sub>2</sub> CO	0.333	—	—	—	
20	CH <sub>2</sub> CH <sub>2</sub> CH <sub>3</sub>	+	OH	→	<i>n</i> -C <sub>3</sub> H <sub>7</sub> OH	0.5	—	—	—	
21	CH <sub>2</sub> CH <sub>2</sub> CH <sub>3</sub>	+	OH	→	C <sub>3</sub> H <sub>6</sub>	0.5	—	—	—	
22	O	+	CH <sub>2</sub> CH <sub>2</sub> CH <sub>3</sub>	→	CH <sub>3</sub> CH <sub>2</sub> CH <sub>2</sub> O	—	—	—	—	
23	H	+	CH <sub>2</sub> CH <sub>2</sub> CH <sub>2</sub> OH	→	<i>n</i> -C <sub>3</sub> H <sub>7</sub> OH	—	—	—	—	
24	H	+	CH <sub>3</sub> CHCH <sub>2</sub> OH	→	<i>n</i> -C <sub>3</sub> H <sub>7</sub> OH	—	—	—	—	
25	H	+	CH <sub>3</sub> CH <sub>2</sub> CHOH	→	<i>n</i> -C <sub>3</sub> H <sub>7</sub> OH	—	—	—	—	
26	H	+	CH <sub>3</sub> CH <sub>2</sub> CH <sub>2</sub> O	→	<i>n</i> -C <sub>3</sub> H <sub>7</sub> OH	—	—	—	—	
27	CH <sub>2</sub>	+	CH <sub>3</sub> CHOH	→	CH <sub>2</sub> CH(OH)CH <sub>3</sub>	—	—	—	—	
28	CH <sub>3</sub>	+	CH <sub>3</sub> CHOH	→	<i>i</i> -C <sub>3</sub> H <sub>7</sub> OH	—	—	—	—	
29	CH <sub>3</sub> CHCH <sub>3</sub>	+	OH	→	<i>i</i> -C <sub>3</sub> H <sub>7</sub> OH	0.5	—	—	—	
30	CH <sub>3</sub> CHCH <sub>3</sub>	+	OH	→	C <sub>3</sub> H <sub>6</sub>	0.5	—	—	—	
31	O	+	CH <sub>3</sub> CHCH <sub>3</sub>	→	CH <sub>3</sub> CH(O)CH <sub>3</sub>	—	—	—	—	
32	H	+	CH <sub>2</sub> CH(OH)CH <sub>3</sub>	→	<i>i</i> -C <sub>3</sub> H <sub>7</sub> OH	—	—	—	—	
33	H	+	CH <sub>3</sub> CH(OH)CH <sub>3</sub>	→	<i>i</i> -C <sub>3</sub> H <sub>7</sub> OH	—	—	—	—	
34	H	+	CH <sub>3</sub> CH(O)CH <sub>3</sub>	→	<i>i</i> -C <sub>3</sub> H <sub>7</sub> OH	—	—	—	—	
35	CN	+	C <sub>3</sub> H <sub>6</sub>	→	CH <sub>3</sub> CHCH <sub>2</sub> CN	—	0.375	—	0	d
36	CN	+	C <sub>3</sub> H <sub>6</sub>	→	CH <sub>2</sub> CH(CN)CH <sub>3</sub>	—	0.25	—	0	d
37	CN	+	C <sub>3</sub> H <sub>6</sub>	→	C <sub>3</sub> H <sub>5</sub>	0.375	—	—	0	d
38	CH <sub>2</sub>	+	C <sub>2</sub> H <sub>3</sub> OH	→	CH <sub>2</sub> CH <sub>2</sub> OH	0.1875	0.25	3600	Est.	
39	CH <sub>2</sub>	+	C <sub>2</sub> H <sub>3</sub> OH	→	<i>n</i> -C <sub>3</sub> H <sub>7</sub> OH	0.1875	0.25	3600	Est.	
40	CH <sub>2</sub>	+	C <sub>2</sub> H <sub>3</sub> OH	→	CH <sub>3</sub> CHOH	0.125	1.00	3760	Est.	
41	CH <sub>2</sub>	+	C <sub>2</sub> H <sub>3</sub> OH	→	<i>i</i> -C <sub>3</sub> H <sub>7</sub> OH	0.125	1.00	3760	Est.	
42	CH <sub>2</sub>	+	C <sub>2</sub> H <sub>3</sub> CN	→	CH <sub>2</sub> CH <sub>2</sub> CN	0.1875	0.25	3600	Est.	
43	CH <sub>2</sub>	+	C <sub>2</sub> H <sub>3</sub> CN	→	<i>n</i> -C <sub>3</sub> H <sub>7</sub> CN	0.1875	0.25	3600	Est.	
44	CH <sub>2</sub>	+	C <sub>2</sub> H <sub>3</sub> CN	→	CH <sub>3</sub> CHCN	0.125	1.00	3760	Est.	
45	CH <sub>2</sub>	+	C <sub>2</sub> H <sub>3</sub> CN	→	<i>i</i> -C <sub>3</sub> H <sub>7</sub> CN	0.125	1.00	3760	Est.	

**Notes.** Dots indicate which atom in a molecule hosts the radical site (i.e. an unpaired electron), where appropriate. Literature references refer to  $E_A$  values;  $F_{\text{dir}}$  and  $F_{\text{comp}}$  values are our own estimates. Branching ratios (BR) are used in case of multiple branches for barrierless, radical-radical reactions. For barrier-mediated reactions, the activation energies and related quantities determine the branching. “Est.” indicates a barrier estimate by the authors based on other reactions in the list. Dashes indicate an assumed activation energy barrier of zero, or the default values for  $F_{\text{dir}}$  and  $F_{\text{comp}}$  (i.e. unity). <sup>(a)</sup> Rao et al. (2011); <sup>(b)</sup> Atkinson et al. (1997); <sup>(c)</sup> Baulch et al. (1992); <sup>(d)</sup> Based on fit to Gannon et al. (2007) gas-phase data, as per Garrod et al. (2017).



**Table C.2.** Selected grain-surface/ice-mantle hydrogen-abstraction and barrier-mediated reactions involved in the formation of vinyl, ethyl, propyl alcohols, as well as updated reactions related to propyl cyanide production. Garrod et al. (2017) provide a more complete list of cyanide-related reactions.

#	Reaction					$F_{\text{dir}}$	$F_{\text{comp}}$	$E_A$ (K)	Ref.
46	H	+	C <sub>3</sub> H <sub>6</sub>	→	$\dot{\text{C}}\text{H}_2\text{CH}_2\text{CH}_3$	0.375	0.25	1320	a
47	H	+	C <sub>3</sub> H <sub>6</sub>	→	$\text{CH}_3\dot{\text{C}}\text{HCH}_3$	0.25	1	619	a
48	H	+	C <sub>3</sub> H <sub>6</sub>	→	C <sub>3</sub> H <sub>5</sub>	0.375	0.25	2930	b
49	$\dot{\text{O}}\text{H}$	+	C <sub>3</sub> H <sub>6</sub>	→	$\text{CH}_3\dot{\text{C}}\text{HCH}_2\text{OH}$	0.375	–	0	c
50	$\dot{\text{O}}\text{H}$	+	C <sub>3</sub> H <sub>6</sub>	→	$\dot{\text{C}}\text{H}_2\text{CH}(\text{OH})\text{CH}_3$	0.25	–	0	d
51	$\dot{\text{O}}\text{H}$	+	C <sub>3</sub> H <sub>6</sub>	→	C <sub>3</sub> H <sub>5</sub>	0.375	1	730	e
52	H	+	C <sub>3</sub> H <sub>8</sub>	→	$\dot{\text{C}}\text{H}_2\text{CH}_2\text{CH}_3$	0.75	0.25	4720	f
53	H	+	C <sub>3</sub> H <sub>8</sub>	→	$\text{CH}_3\dot{\text{C}}\text{HCH}_3$	0.25	1	4000	f
54	$\dot{\text{O}}\text{H}$	+	C <sub>3</sub> H <sub>8</sub>	→	$\dot{\text{C}}\text{H}_2\text{CH}_2\text{CH}_3$	0.75	0.25	1310	g
55	$\dot{\text{O}}\text{H}$	+	C <sub>3</sub> H <sub>8</sub>	→	$\text{CH}_3\dot{\text{C}}\text{HCH}_3$	0.25	1	1120	g
56	H	+	C <sub>2</sub> H <sub>5</sub> OH	→	$\dot{\text{C}}\text{H}_2\text{CH}_2\text{OH}$	0.375	0.25	3770	h
57	H	+	C <sub>2</sub> H <sub>5</sub> OH	→	$\text{CH}_3\dot{\text{C}}\text{HOH}$	0.25	1	2710	i
58	H	+	C <sub>2</sub> H <sub>5</sub> OH	→	C <sub>2</sub> H <sub>5</sub> $\dot{\text{O}}$	0.375	0.25	4380	h
59	$\dot{\text{O}}\text{H}$	+	C <sub>2</sub> H <sub>5</sub> OH	→	$\dot{\text{C}}\text{H}_2\text{CH}_2\text{OH}$	0.375	0.25	889	E-P
60	$\dot{\text{O}}\text{H}$	+	C <sub>2</sub> H <sub>5</sub> OH	→	$\text{CH}_3\dot{\text{C}}\text{HOH}$	0.25	1	70	j
61	$\dot{\text{O}}\text{H}$	+	C <sub>2</sub> H <sub>5</sub> OH	→	C <sub>2</sub> H <sub>5</sub> $\dot{\text{O}}$	0.375	0.25	1510	E-P
62	H	+	C <sub>2</sub> H <sub>5</sub> CN	→	$\dot{\text{C}}\text{H}_2\text{CH}_2\text{CN}$	0.375	0.25	4720	Est.
63	H	+	C <sub>2</sub> H <sub>5</sub> CN	→	$\text{CH}_3\dot{\text{C}}\text{HCN}$	0.25	1	4000	Est.
64	$\dot{\text{O}}\text{H}$	+	C <sub>2</sub> H <sub>5</sub> CN	→	$\dot{\text{C}}\text{H}_2\text{CH}_2\text{CN}$	0.375	0.25	1790	k
65	$\dot{\text{O}}\text{H}$	+	C <sub>2</sub> H <sub>5</sub> CN	→	$\text{CH}_3\dot{\text{C}}\text{HCN}$	0.25	1	1060	k
66	H	+	C <sub>3</sub> H <sub>7</sub> OH	→	$\dot{\text{C}}\text{H}_2\text{CH}_2\text{CH}_2\text{OH}$	0.3	0.25	3710	E-P
67	H	+	C <sub>3</sub> H <sub>7</sub> OH	→	$\text{CH}_3\dot{\text{C}}\text{HCH}_2\text{OH}$	0.2	1	3080	E-P
68	H	+	C <sub>3</sub> H <sub>7</sub> OH	→	$\text{CH}_3\text{CH}_2\dot{\text{C}}\text{HOH}$	0.2	1	3080	E-P
69	H	+	C <sub>3</sub> H <sub>7</sub> OH	→	C <sub>3</sub> H <sub>7</sub> $\dot{\text{O}}$	0.3	0.25	4780	E-P
70	$\dot{\text{O}}\text{H}$	+	C <sub>3</sub> H <sub>7</sub> OH	→	$\dot{\text{C}}\text{H}_2\text{CH}_2\text{CH}_2\text{OH}$	0.3	0.25	522	E-P
71	$\dot{\text{O}}\text{H}$	+	C <sub>3</sub> H <sub>7</sub> OH	→	$\text{CH}_3\dot{\text{C}}\text{HCH}_2\text{OH}$	0.2	1	125	E-P
72	$\dot{\text{O}}\text{H}$	+	C <sub>3</sub> H <sub>7</sub> OH	→	$\text{CH}_3\text{CH}_2\dot{\text{C}}\text{HOH}$	0.2	1	125	E-P
73	$\dot{\text{O}}\text{H}$	+	C <sub>3</sub> H <sub>7</sub> OH	→	C <sub>3</sub> H <sub>7</sub> $\dot{\text{O}}$	0.3	0.25	1210	E-P
74	H	+	<i>i</i> -C <sub>3</sub> H <sub>7</sub> OH	→	$\dot{\text{C}}\text{H}_2\text{CH}(\text{OH})\text{CH}_3$	0.6	0.25	3710	E-P
75	H	+	<i>i</i> -C <sub>3</sub> H <sub>7</sub> OH	→	$\text{CH}_3\dot{\text{C}}(\text{OH})\text{CH}_3$	0.1	1	3080	E-P
76	H	+	<i>i</i> -C <sub>3</sub> H <sub>7</sub> OH	→	$\text{CH}_3\text{CH}(\dot{\text{O}})\text{CH}_3$	0.3	0.25	6080	E-P
77	$\dot{\text{O}}\text{H}$	+	<i>i</i> -C <sub>3</sub> H <sub>7</sub> OH	→	$\dot{\text{C}}\text{H}_2\text{CH}(\text{OH})\text{CH}_3$	0.6	0.25	522	E-P
78	$\dot{\text{O}}\text{H}$	+	<i>i</i> -C <sub>3</sub> H <sub>7</sub> OH	→	$\text{CH}_3\dot{\text{C}}(\text{OH})\text{CH}_3$	0.1	1	125	E-P
79	$\dot{\text{O}}\text{H}$	+	<i>i</i> -C <sub>3</sub> H <sub>7</sub> OH	→	$\text{CH}_3\text{CH}(\dot{\text{O}})\text{CH}_3$	0.3	0.25	2040	E-P
80	H	+	C <sub>3</sub> H <sub>7</sub> CN	→	$\dot{\text{C}}\text{H}_2\text{CH}_2\text{CH}_2\text{CN}$	0.3	0.25	3710	E-P
81	H	+	C <sub>3</sub> H <sub>7</sub> CN	→	$\text{CH}_3\dot{\text{C}}\text{HCH}_2\text{CN}$	0.2	1	3080	E-P
82	H	+	C <sub>3</sub> H <sub>7</sub> CN	→	$\text{CH}_3\text{CH}_2\dot{\text{C}}\text{HCN}$	0.2	1	3080	E-P
83	$\dot{\text{O}}\text{H}$	+	C <sub>3</sub> H <sub>7</sub> CN	→	$\dot{\text{C}}\text{H}_2\text{CH}_2\text{CH}_2\text{CN}$	0.3	0.25	1000	Est.
84	$\dot{\text{O}}\text{H}$	+	C <sub>3</sub> H <sub>7</sub> CN	→	$\text{CH}_3\dot{\text{C}}\text{HCH}_2\text{CN}$	0.2	1	800	Est.
85	$\dot{\text{O}}\text{H}$	+	C <sub>3</sub> H <sub>7</sub> CN	→	$\text{CH}_3\text{CH}_2\dot{\text{C}}\text{HCN}$	0.2	1	800	Est.
86	H	+	<i>i</i> -C <sub>3</sub> H <sub>7</sub> CN	→	$\dot{\text{C}}\text{H}_2\text{CH}(\text{CN})\text{CH}_3$	0.6	0.25	3710	E-P
87	H	+	<i>i</i> -C <sub>3</sub> H <sub>7</sub> CN	→	$\text{CH}_3\dot{\text{C}}(\text{CN})\text{CH}_3$	0.1	1	3080	E-P
88	$\dot{\text{O}}\text{H}$	+	<i>i</i> -C <sub>3</sub> H <sub>7</sub> CN	→	$\dot{\text{C}}\text{H}_2\text{CH}(\text{CN})\text{CH}_3$	0.6	0.25	1000	Est.
89	$\dot{\text{O}}\text{H}$	+	<i>i</i> -C <sub>3</sub> H <sub>7</sub> CN	→	$\text{CH}_3\dot{\text{C}}(\text{CN})\text{CH}_3$	0.1	1	800	Est.

**Notes.** Dots indicate which atom in a molecule hosts the radical site (i.e. an unpaired electron), where appropriate. Literature references refer to  $E_A$  values;  $F_{\text{dir}}$  and  $F_{\text{comp}}$  values are our own estimates. “E-P” indicates an activation energy calculated using the Evans-Polanyi relation; see Garrod (2013). “Est.” indicates a barrier estimate by the authors based on other reactions in the list. <sup>(a)</sup> Curran (2006); <sup>(b)</sup> Tsang (1992); <sup>(c)</sup> Atkinson et al. (1997); <sup>(d)</sup> Thomsen & Jorgensen (2009); <sup>(e)</sup> Tsang (1991); <sup>(f)</sup> Baldwin & Walker (1979); <sup>(g)</sup> Hu et al. (1997); <sup>(h)</sup> Sivaramakrishnan et al. (2010); <sup>(i)</sup> Olm et al. (2016); <sup>(j)</sup> Atkinson et al. (2001); <sup>(k)</sup> based on fitting to data from Sun et al. (2008).

**Table C.3.** Physical quantities of new or related chemical species.

Species	$E_{\text{des}}$ (K)	$\Delta H_f(298\text{ K})$ (kcal mol <sup>-1</sup> )	Notes
H <sub>2</sub> O	4815	-57.80	$E_{\text{des}}$ : Jin et al. (in prep.)
CH <sub>3</sub> OH	5534	-48.00	$E_{\text{des}}$ : Garrod et al. (2008), Garrod (2013)
$\dot{\text{C}}\text{H}_2\text{CH}_2\text{OH}$	4950	-5.70	
CH <sub>3</sub> $\dot{\text{C}}\text{HOH}$	4950	-12.91	
C <sub>2</sub> H <sub>5</sub> OH	5400	-56.23	$E_{\text{des}}$ : Jin et al. (in prep.)
$\dot{\text{C}}\text{H}_2\text{CH}_2\text{CH}_2\text{OH}$	5675	-12.28	$\Delta H_f$ based on C <sub>3</sub> H <sub>8</sub> – $\dot{\text{C}}\text{H}_2\text{CH}_2\text{CH}_3$
CH <sub>3</sub> $\dot{\text{C}}\text{HCH}_2\text{OH}$	5675	-14.18	$\Delta H_f$ based on C <sub>3</sub> H <sub>8</sub> – CH <sub>3</sub> $\dot{\text{C}}\text{HCH}_3$
CH <sub>3</sub> CH <sub>2</sub> $\dot{\text{C}}\text{HOH}$	5675	-14.18	$\Delta H_f$ based on C <sub>3</sub> H <sub>8</sub> – CH <sub>3</sub> $\dot{\text{C}}\text{HCH}_3$
CH <sub>3</sub> CH <sub>2</sub> CH <sub>2</sub> $\dot{\text{O}}$	5462	-9.00	
<i>n</i> -C <sub>3</sub> H <sub>7</sub> OH	6125	-61.20	
$\dot{\text{C}}\text{H}_2\text{CH}(\text{OH})\text{CH}_3$	5675	-16.27	$\Delta H_f$ based on C <sub>3</sub> H <sub>8</sub> – $\dot{\text{C}}\text{H}_2\text{CH}_2\text{CH}_3$
CH <sub>3</sub> $\dot{\text{C}}(\text{OH})\text{CH}_3$	5675	-18.17	$\Delta H_f$ based on C <sub>3</sub> H <sub>8</sub> – CH <sub>3</sub> $\dot{\text{C}}\text{HCH}_3$
CH <sub>3</sub> CH( $\dot{\text{O}}$ )CH <sub>3</sub>	5462	-9.00	$\Delta H_f$ based on <i>n</i> -C <sub>3</sub> H <sub>7</sub> $\dot{\text{O}}$
<i>i</i> -C <sub>3</sub> H <sub>7</sub> OH	6125	-65.19	
$\dot{\text{C}}\text{H}_2\text{CH}_2\text{CH}_3$	5637	+23.90	$E_{\text{des}}$ : Garrod et al. (2017)
CH <sub>3</sub> $\dot{\text{C}}\text{HCH}_3$	5637	+22.00	$E_{\text{des}}$ : Garrod et al. (2017)
C <sub>3</sub> H <sub>8</sub>	6087	-25.02	$E_{\text{des}}$ : Garrod et al. (2017)
CH <sub>3</sub> CN	6150	+17.70	$E_{\text{des}}$ : Bertin et al. (2017); used by Garrod et al. (2022)
C <sub>2</sub> H <sub>5</sub> CN	6875	+12.71	$E_{\text{des}}$ : Garrod et al. (2022)
<i>n</i> -C <sub>3</sub> H <sub>7</sub> CN	7600	+7.46	$E_{\text{des}}$ : Garrod et al. (2022)
<i>i</i> -C <sub>3</sub> H <sub>7</sub> CN	7600	+5.44	$E_{\text{des}}$ : Garrod et al. (2022)

**Notes.**  $E_{\text{des}}$  is the desorption energy and  $\Delta H_f$  the enthalpy of formation. Dots indicate which atom in a molecule hosts the radical site (i.e. an unpaired electron), where appropriate. As in previous models, binding energies are representative of physisorption on an amorphous water ice surface. Enthalpies of formation are obtained from the NIST WebBook database; where not available, estimates were adopted as described in the Notes column.